MICRO-MECHANICAL ANALYSIS OF QUASI-STATIC PARTICULATE FRAGMENTATION APPLIED TO GEOMATERIALS

A Dissertation
Presented to
The Academic Faculty

By

Pei Wang

In Partial Fulfillment
of the Requirements for the Degree
Doctor of Philosophy in the
School of School of Civil and Environmental Engineering

Georgia Institute of Technology

May 2019

MICRO-MECHANICAL ANALYSIS OF QUASI-STATIC PARTICULATE FRAGMENTATION APPLIED TO GEOMATERIALS

Approved by:

Dr. Chloé Arson, Advisor
School of Civil and Environmental
Georgia Institute of Technology

Dr. David Frost
School of Civil and Environmental
Georgia Institute of Technology

Dr. Sheng Dai
School of Civil and Environmental
Georgia Institute of Technology

Dr. Richard W. Neu
School of Mechanical Engineering
Georgia Institute of Technology

Dr. Cino Viggiani
Laboratoire 3SR
Université Joseph Fourier

Date Approved: December 1, 2018

ACKNOWLEDGEMENTS

First and foremost, I would like to thank my advisor, Dr. Chloé Arson, for her guidance, support, and inspiration throughout my research and study at Georgia Tech. She has been creating an exceptionally innovative research environment which inspires me to explore novel theories and ideas. Her rigorous attitude and continuous energy towards scientific research greatly impress me and have set up a good example for me in my future reserach.

I would also like to sincerely thank my committee members: Dr. Sheng Dai, Dr. David Frost, Dr. Richard W. Neu and Dr. Cino Viggiani. Their generous support and guidance have shaped this thesis in many ways.

The work presented in this thesis would not have been possible without my collaborators, Dr. Stewart and her group, Dr. Zeynep Karatza, Dr. Edward Andò and Olumide Okubadejo.

I also want to thank all the DeeP MeLT group members, both past and current. It has been an absolute pleasure knowing every one of you. Special thanks to Cheng Zhu, Wencheng Jin, Xianda Shen, Koochul Ji, and Fernando Patino Ramirez for their valuable discussions.

Lastly, I want to thank my family for all the support and companion. Special thanks to my wife, Jingjie Wu, whose unwavering support has propelled me through many challenges in the past few years.

TABLE OF CONTENTS

LIST OF TABLES

LIST OF FIGURES

SUMMARY

Particulate fragmentation, the process by which large particles break into fragments, results in important changes Particle Size Distribution (PSD), particle shape, void ratio, permeability, compressibility, shear strength and stress-strain behavior. Particulate breakage can occur in different geomaterials from crushable granular materials to rock-fills and concrete aggregates. Various constitutive laws were proposed to relate the mechanical behavior of granular materials to breakage indexes. Despite the progress made on modeling granular mechanics at the macro-scale, discriminating the mechanisms that control particle breakage within a particulate assembly is still an open issue. For example, particle strength is known to decrease with particle size (so called size effect). But statistically, larger particles are more likely to have a larger coordination number, thus to be subjected to a more uniform contact stress (so called shielding effect) and to have a lower probability of breakage. As a result, the conditions in which a large particle size prevents breakage are not well understood. In this thesis, we analyze particle fragmentation and the associated energy distribution from a micro-mechanical standpoint.

We first explain the state of the art in terms of micro-macro modeling of breakage in granular assemblies, and we present in detail the pros and cons of the techniques employed in the Discrete Element Method (DEM) to simulate particle crushing.

Second, we conduct a numerical study at the particle scale to understand in which conditions shielding effects overcome size effects. We also investigate the influence of microscopic flaws on particle crushing. Our simulations highlight the predominant influence of porosity over flaw size and show that particle strength depends linearly on the particle coordination number and quadratically on particle porosity.

Third, we analyze micro-CT scans obtained sequentially during an oedometer test of zeolite to model crushing at the scale of a granular assembly. We implement a new breakage model in DEM, which combines particle replacement, for primary splitting breakage, and cluster bond breakage, for modeling for fragment breakage. An important improvement upon previously published models is that during the tensile splitting, the breakage plane is defined by the contact carrying the maximum normal force and direction of minimum principal stress, instead of assuming that the breakage plane contains the two maximum contact force vectors. The PSD obtained with the new DEM model exhibited an impressive matching with experimental results. The new breakage model could also capture the experimental stress-strain relationship at the macroscopic scale.

Fourth, we analyze the evolution of the energy of a granular assembly subject to particulate breakage during quasi-static confined comminution. Energy potentials are related to internal variables that have a clear relationship to microstructure evolution, e.g. deviation to initial and ultimate PSDs, particle specific surface, porosity. DEM simulations show that: At least 60% of the work input is dissipated by particle redistribution; The fraction of elastic deformation energy increases and the fraction of redistribution energy decreases as the compression stress increases; The breakage energy accounts for less than 5% of the total input energy, and this value is independent of the compressive stress; The energy dissipated by redistribution is between 14 to 30 times larger than the breakage energy.

Lastly, we propose a DEM displacement-softening contact model to simulate fracture propagation in concrete. Aggregates are designed from point clouds obtained by scanning actual aggregates. The Interfacial Transition Zone (ITZ) is accounted for by deleting bonds at the interface between aggregates and mortar. We calibrate the model with results of uniaxial compression tests and Brazilian tests of both mortar and concrete. DEM simulations confirm that concrete does not fail in pure tensile mode during Brazilian tests. Sensitivity

analyses also show that concrete strength depends linearly on both the adhesive area fraction of the ITZ and the aggregate tensile strength. The ITZ has a greater effect on concrete strength than aggregate strength.

Future studies will focus on the modeling of various simultaneous breakage mechanisms (e.g. splitting, multi-fragmentation, chipping, erosion) and on their relation to the macroscopic response of the granular assembly, as well as the modeling of cyclic effects, the prediction of bond corrosion in the presence of water, and the design of bond reparation.

CHAPTER 1
INTRODUCTION AND BACKGROUND

1.1 Motivations and Objectives

Particulate fragmentation is involved in many disciplines, such as powder engineering, the mining industry, food processing and civil engineering. Particle breakage (or particle crushing) refers to the process by which grains break into fragments or fines. For example, the production of fault gouge is the result of continuous particle crushing of particles between fault surfaces. In the mining industry, ore crushing is usually the first step of mineral processing [1]. In civil engineering, the cost of mitigating ballast particle crushing is estimated to be more than half of the total construction cost of railways [2]. Even heterogenous solids like concrete are subject to particle crushing, because weak aggregates break during Brazilian tests and uniaxial compression tests [3]. In the pharmaceutical industry, a common approach to increase drug solubility, which controls the rate and extent of drug absorption, is to reduce the size of tablets or powder grains by crushing [4, 5]. In order to understand and simulate the mechanical behavior of granular and aggregate-bearing materials at the macroscopic scale (laboratory scale to engineering structure scale), a fundamental understanding of the driving micro-mechanisms of particle breakage is required.

Particulate fragmentation results in important changes in granular material properties, e.g., particle size distribution, void ratio, particle shape and strength. Some studies claim that the normal compression line in the plot of void ratio vs. the logarithm of effective stress is characteristic of particle crushing, and that the sudden decrease in the rate of hardening (yielding region) indicates the onset of particle crushing which is shown as region 2 in Figure 1.1 [6, 7]. In other studies, it is found that the size of the yield surface is related to a crushing index [8]. Permeability of granular materials is closely related to the Particle

Size Distribution (PSD): fine particles generated during crushing tend to clog pores, which reduces permeability [9, 10].

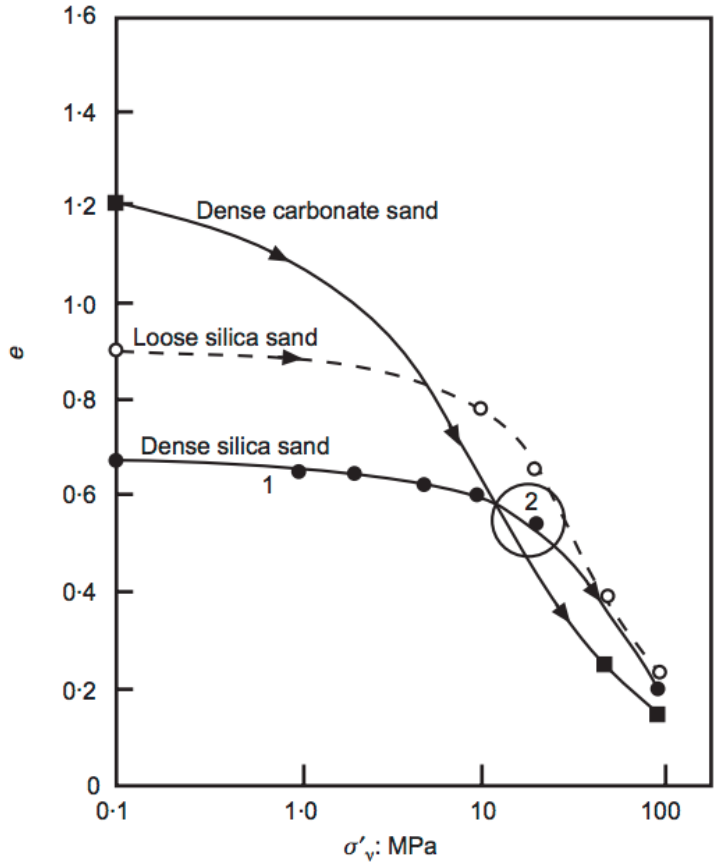

Figure 1.1: One-dimensional compression plots showning the yielding region 2 [6]

Extensive experimental studies were done at the particle scale. Diametric compression tests were conducted on single particles, to measure tensile strength, assess particle size and shape effects and analyze breakage modes. The stress distribution in an elastic sphere subjected to diametrical compression was obtained analytically by Hiramatsu in 1966 [11]; the model also provides a definition of particle tensile strength. Robertson conducted single particle crushing tests with three different materials, and the results show that failure of grain asperities occurs before major failure, and that tensile strength depends on particle size [12]. Salamia et al created a device to study the effect of coordination number on grain crushing in 2D, and concluded that existing models are incapable to reproducing the

fragmentation process [13].

Numerically, the Discrete Element Method (DEM), also called Distinct Element Method, is one of the most common tools to simulate particulate fragmentation. The DEM allows calculating the displacements of particles within a granular assemblies, as well as the induced contact forces. Averaging methods can be employed to characterize the macroscopic mechanical behavior of the granular assembly. Any PSD can be assigned to the DEM particulate elements. Particle contacts are governed by contact laws, such as the linear or the Hertz contact law. In addition, in order to model non-spherical particles or solid materials, particles can be bonded together at contacts. The DEM can thus be used to simulate fracture propagation as a sequence of bond breakages. The properties of contact bonds play an important role in controlling the behavior of materials. In our analysis of particle fragmentation, crushable grains are modeled as clusters of bonded particles, in which successive bond breakages lead to fragmentation, attrition or abrasion. The DEM solution depends on the number, size and packing of the elementary particles used in the model, and on the bond parameters [14, 15, 16]. Another method to model particle fragmentation is to replace a broken particle with smaller particles representing fragments. This replacement method requires postulating a breakage criterion, a breakage plane orientation, as well as the resulting sizes and shapes of the fragments. To this date, no quantitative model exists for some micro-mechanisms that occur at single particle scale, such as size effects and shielding effects. At the scale of the granular assembly, current numerical models do not allow simulating sequential breakage with non-spherical fragments, which is however a common situation encountered in confined comminution tests [17, 18, 19].

Thermodynamic and phenomenological models were proposed to predict the behavior of granular materials that undergo particulate fragmentation. The total input energy of the sample is transformed into elastic energy, breakage energy, friction dissipation and redistribution energy [20]. The energy distribution equation is the foundation of the constitutive relationship between stress and strain. A good understanding of how the energy dissipates

during the fragmentation process is necessary to formulate sound constitutive models for granular materials. How to calculate the relative fraction of the energy components dissipated during comminution has been studied for decades both at the grain and at the sample scales, with analytical, numerical and experimental methods [21, 22, 23]. Previous results show that energy is mostly dissipated by particle redistribution and inter-granular friction. However, there is still no consensus on the relative fraction of the different components of energy dissipated, which raises challenges in deriving thermodynamic based constitutive equations.

Coarse aggregate fragmentation is common in concrete. Properties of coarse aggregates have a strong influence on the mechanical behavior of concrete. In particular, weak coarse aggregates greatly decrease both the tensile strength and the uniaxial compressive strength of concrete [24]. In addition, the existence of coarse aggregates increase concrete porosity, and thus decreases concrete strength. The interfacial transition zone (ITZ) between coarse aggregates and mortar also affects strengths of concrete [25]. It is believed that the ITZ has weaker bonding strength due to higher water content near the coarse aggregates. However, no quantitative analysis was conducted so far to understand the effects of coarse aggregate strength and of the ITZ on concrete strength.

1.2 Plan of the Thesis

In this thesis, we analyze particulate fragmentation of geomaterials and the associated energy distribution from a micro-mechanical standpoint. We start with a literature review on particle crushing in granular materials across scales in Chapter 2. In Chapter 3, we focus on the micro-parameters that affect the most elementary crushing event: single particle crushing. Then in Chapter 4, we upscale our analysis to an assembly of grains subjected to confined comminution. We propose a new model to provide a more accurate representation of fracture planes, and to account for sequential breakage events based on XCT images of an oedometer test. Chapter 5 deals with the evolution of energy redistribution during the

compression of granular materials. Several modeling strategies are discussed. In Chapter 6, we focus on the fragmentation of coarse aggregates in concrete. A displacement-softening contact model is proposed to simulate the behavior of mortar and coarse aggregates. The effects of the aggregate tensile strength and of the adhesive area of the interfacial transition zone are analyzed. Chapter 7 presents the conclusions of this doctoral work.

CHAPTER 2

CHARACTERIZATION AND MODELING OF PARTICLE CRUSHING: STATE-OF-THE-ART

Particle crushing, which is also called particle breakage, refers to the process by which grains break into smaller fragments due to high contact forces. The first mechanical analyses of particle crushing date back from the 1960s and focus on single particle strength [26, 27]. Later, the mechanical response of granular assemblies subject to crushing gaines a lot of attention [28]. Particle breakage results in a change of the Particle Size Distribution and in the reduction on average particle size – a phenomenon called grain comminution. For instance, grain comminution occurs in zeolite during oedometer tests [29]. Figure 2.1 illustrates different modes of particle breakage, including fracture, attrition and abrasion [30]. In this chapter, we review the state-of-the-art of characterization and modeling of particle crushing.

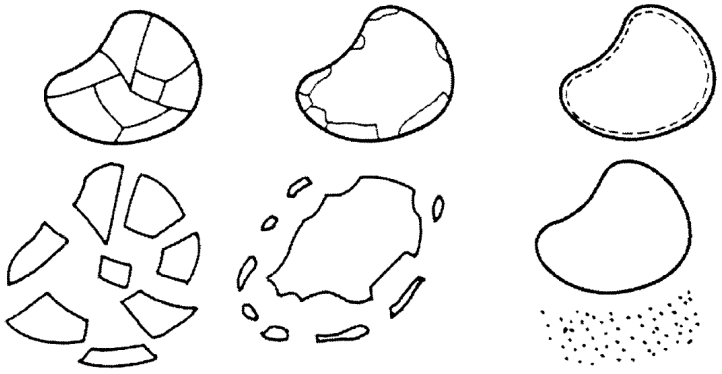

Figure 2.1: Three modes of particle crushing: fracture, attrition and abrasion [30]

2.1 Phenomenological Description of Particle Crushing

Particle crushing can be characterized by the evolution of Particle Size Distribution (PSD). Several breakage indexes were defined in order to measure the influence of crushing on

the engineering properties of granular materials [31]. For instance, Marsal calculated the percentage differences in particles passing each sieve size, before and after a crushing test, and defined the breakage index B as the sum of these differences [32]. Except for the largest grain size initially present in the sample, the percentage difference can be positive or negative. B varies between 0% and 100%. In another study that considers fine particles, the particle breakage index is defined as the ratio of $D_{15(before)}/D_{15(after)}$, in which D_{15} is defined such that 15% of the mass of the sample is made of grains that have a diameter lower than D_{15} [33]. 'After' and 'before' subscripts refer to measures done before and after the crushing test, respectively. Hardin [34] defined the breakage potential B_p as the area between the initial PSD curve and the line defining a particle size of 0.074mm, as shown in Figure 2.2. Similarly, the total breakage parameter, B_t, is defined as the area comprised between the PSD curves before and after the crushing test. The relative breakage B_r is expressed as the ratio between the total breakage and the breakage potential. The value of 0.074 mm corresponds to the upper limit size of silt particles. Because extremely high stress is required to crush silt particles, a soil sample was considered completely crushed when no particle larger than 0.074 mm subsisted after curshing. Recent studies confirm that silt particles have very high strength and store less elastic energy than larger particles [35], and also indicate that the final PSD follows a Weibull distribution with the same largest particle size as in the initial PSD [36].

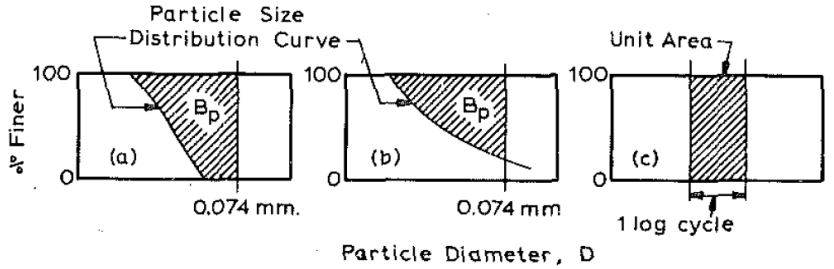

Figure 2.2: Definition of Hardin's breakage potential [34]

In order to correlate the particle breakage with standard soil parameters, Lade *et al* [31]

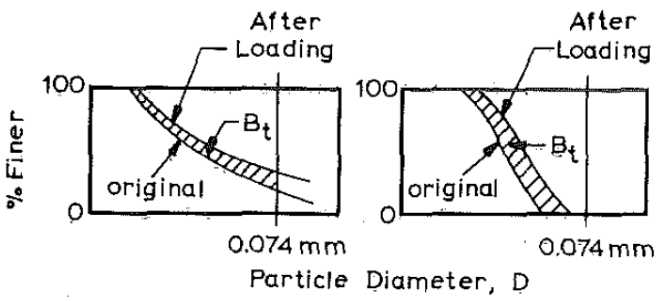

Figure 2.3: Definition of Hardin's total breakage parameter [34]

proposed the following breakage factor B_{10}:

$$B_{10} = 1 - \frac{D_{10f}}{D_{10i}} \tag{2.1}$$

in which D_{10i} and D_{10t} are the grain diameters that are such that 10% of the mass of the sample is made of grains that have a diameter lower than D_{10i} (before the crushing test) and D_{10t} (after the crushing test), respectively. The authors studied the relationship between soil parameters and the particle breakage factors proposed by Marsal [32], Lee and Farhoomand [33] and Hardin [34]. Lade's breakage parameter can be used to calculate the total energy input to a granular assembly, as well as the intrinsic permeability of a sand. However, it was found that no unifying breakage factor could capture all the soil behavior features. For example breakage factor proposed by Marsal remains less than 0.4 under an axial stress of up to 40 MPa in triaxial extension tests, but takes reasonable values in triaxial compression tests [31].

The main inconvenient of Hardin's breakage index is that it cannot account for the production of fines under compressive stresses higher than 100 MPa or under shear strains exceeding 0.5. That is why other models were put forward, in which the fragmentation is a scale invariant process, through which any initial PSD is transformed into a self-similar distribution. In a study of fault gouge samples [37], a self-similar grain size distribution was evidenced by comparing the relative fractions of particle classes at different scales.

The ultimate PSD was modeled as a fractal relationship between the number and the sizes of grains. The number of grains N with a diameter larger than d is expressed as [38]:

$$N = Cd^{-\alpha} \tag{2.2}$$

where C is a constant and α is the fractal dimension. Eq.2.2 is expressed in terms of particle size (d), while the PSD determined in the laboratory is expressed in terms of the mass of particles finer than a certain size d (noted M_d). Assuming that all particles have the same shape, M_d is calculated as follows:

$$M_d = \int_{d_m}^{d} s\rho d^3 \mathrm{d}N = \frac{C\alpha s\rho}{3-\alpha}(d^{3-\alpha} - d_m^{3-\alpha}) \tag{2.3}$$

where s is the shape factor, which relates the particle volume to the cube of its diameter, d^3 ($s = \pi/6$ for spheres), ρ is the mass density and d_m is the minimum particle size [39, 36]. If d_m is equal to zero, the ultimate PSD is expressed as:

$$F_u(d) = \frac{M_d}{M_T} = \Big(\frac{d}{d_M}\Big)^{(3-\alpha)} \tag{2.4}$$

Based on the expression of the ultimate PSD stated in Eq.2.4, Einav [36] redefined the relative and potential breakage parameters (B_r and B_p) as follows:

$$B_t = \int_{d_m}^{d_M} (F(d) - F_0(d))\mathrm{d}(\log d) = ln^{-1}10 \int_{d_m}^{d_M} (F(d) - F_0(d))d^{-1}\mathrm{d}d \tag{2.5}$$

$$B_p = \int_{d_m}^{d_M} (F_u(d) - F_0(d))\mathrm{d}(\log d) = ln^{-1}10 \int_{d_m}^{d_M} (F_u(d) - F_0(d))d^{-1}\mathrm{d}d \tag{2.6}$$

The physical meaning of these two parameters remains the same, B_t is the area of the domain that is between the current and initial PSD curves; B_p is the area of the domain that is between the final and initial PSD curves. The prediction of the ultimate PSD with Einav's model matches experimental data better than with Hardin's model.

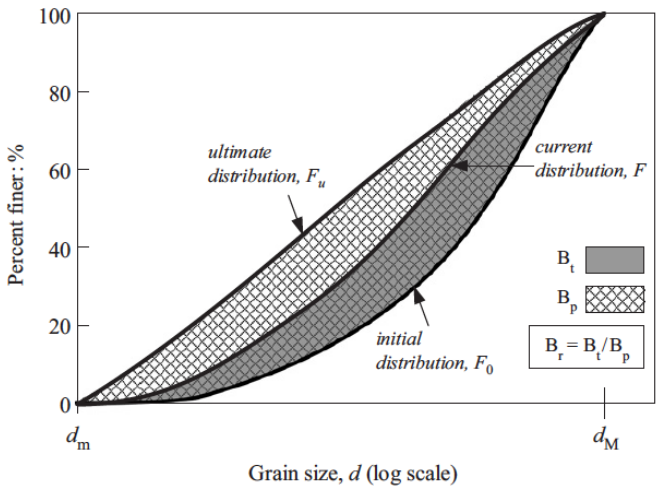

Figure 2.4: Modified definition of the breakage index B_r, proposed by Einav [36]

2.2 Micromechanical Description of Particle Crushing

In order to understand the micromechanical origin of grain breakage, single particle crushing tests were conducted, in which grains were placed between two loading platens or loading points. Particle crushing tests conducted on grains of different shapes indicated that grains break because of tensile failure [11]. As an example, two force-displacement curves obtained during single particle crushing tests of sand particles are shown in Figure 2.5. The particle usually breaks into two or three parts. Recent studies indicate that this type of failure is governed by tensile strength [40]. The tensile strength of a brittle grain subjected to diametrical loading can be obtained by:

$$\sigma_t = \frac{\alpha F_t}{d^2} \tag{2.7}$$

where σ_t is the tensile strength, F_t is the maximum compressive force, α is a parameter that usually lies in the range of 0.4 to 1.5 and d is the distance between loading points when breakage occurs. Note that d is not the distance that separates the loading points when the loading points are still in contact with the grain, before breakage.

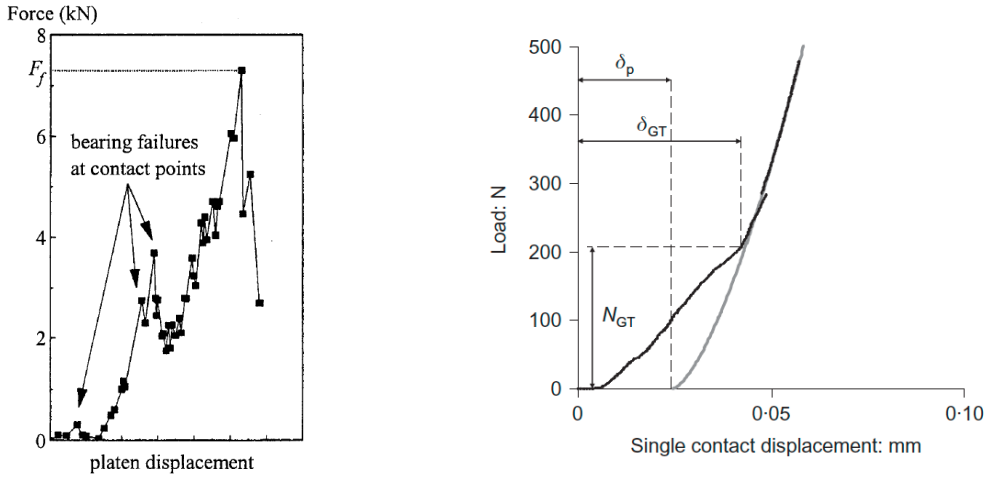

Figure 2.5: Typical load-displacement curves in sand single-particle crushing tests [6].

Photo-elasticity was used to visualize the stress distribution in a grain subjected to diametrically opposite concentrated loads. Stresses in the loading direction are very similar to those shown in Figure 2.6. Analytical models of stress distribution in elastic spherical grains indicate that σ_θ is tensile, and that its value is uniform over a segment of length equal to the particle radius, centered at the particle center. Numerical models were verified against this theoretical solution [15].

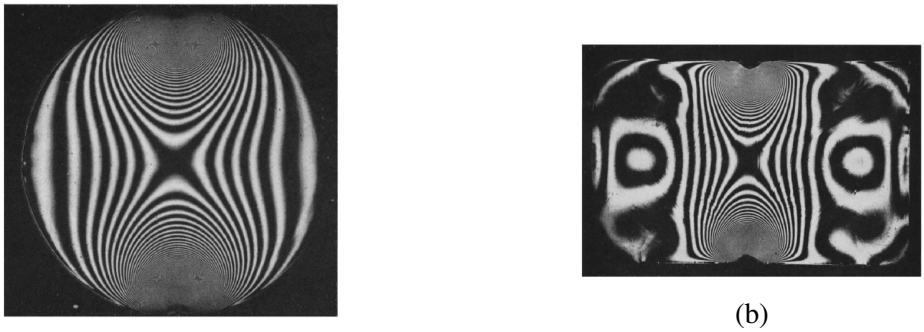

(a) (b)

Figure 2.6: Stress patterns observed in a photo-elastic (a) sphere and (b) rectangular prism [11]

It was noted experimentally that the compressive strength of a particle decreases with its size (so called size effect) [41, 42, 43, 44, 45, 46]. Lee conducted single particle crushing tests on three different materials, i.e. Leighton Buzzard sand, oolitic limestone and

carboniferous limestone, and found that the tensile strengths could be described by the relationship $\sigma_t \propto d^b \, (b < 0)$, as is shown in Figure 2.7. Size effects can be explained by the weakest link theory: the strength of a particle is dominated by large cracks/flaws, which are more likely to exist in large grains. Ma proposed that size effects are related to the size of a fracture processing zone (noted l) and to the sample size (noted D), and that size effects vanish when l/D becomes lower than a certain threshold [47]. Some researchers argue that crushing is driven by the propagation of surface flaws rather than by tensile failure. For instance, Brzesowsky *et al* successfully modeled crushing tests performed on sand grains of different sizes with a Hertzian fracture mechanics model applied to the propagation of surface flaws [48].

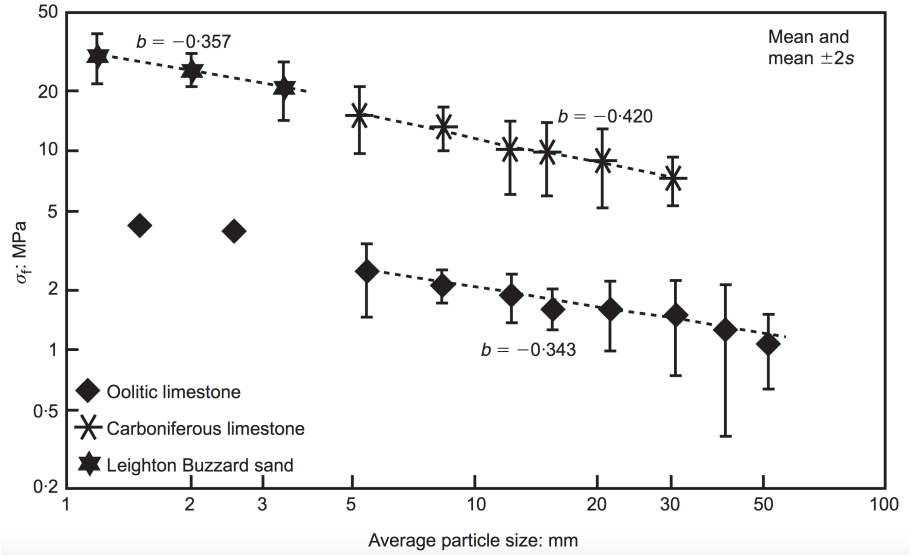

Figure 2.7: Tensile strength as a function of particle size [49]

A particle is in general not subjected to diametrical loading within a granular assembly. The coordination number of a particle is defined as the number of grains that are in contact with that particle (and potentially, applying a reaction force on that particle). Several studies were conducted to understand the influence of the coordination number on particle breakage [13, 50, 51, 52]. The analytical distribution of stress in a particle with a coordination number larger than 2 depends on the relative position of the contact forces, and is

therefore complex, especially in 3D. Solutions obtained for simplified loading conditions, such as four contact points positioned symmetrically, indicate a clear decrease of tensile stress at the center of the particle [27]. In addition, a recent study shows that the coordination number, the relative position of the contacts and type of contact forces (i.e., normal vs. tangential) all play an important role on grain fragmentation [13]. Each grain in contact with a particle potentialy applies a contact force on that particle; the combination of all contact forces redistributes tensile stress in the particle. As a result, a higher coordination number yields a higher crushing strength – a phenomenon known as shielding effect.

X-ray tomography was used to characterize the shape of broken grains and to evaluate of the effects of fragments on the macroscopic behavior of granular materials [53]. The evolution of the PSD was monitored during high-confinement triaxial compression tests [49] to relate breakage events to Loading Steps (LS), as shown in Figure 2.8. 3D+t image analysis was recently put forward to quantify grain breakage over time. The methods involves grain labelling and tracking in two different steps, which reduces errors.

2.3 Micro-macro Modeling of Particle Crushing

The effect of particle crushing on the macroscopic stress-strain relationship of a granular medium is still not fully understood. During the crushing process, the total work input energy turns into elastic potential energy, dissipated breakage energy and dissipated redistribution energy. The latter is the sum of the kinetic energy of moving fragments, plus friction energy dissipated at the contacts between fragments [20, 23, 35].

Particle breakage is usually modelled by relating energy dissipation to the increase of particules' surface and/or to the frictional displacement field [54, 30, 55]. Based on energy balance and critical soil mechanics, McDowell and collaborators [39] proposed the following constitutive relationship for uniaxial compression:

$$\bar{\sigma}\mathrm{d}\bar{\varepsilon}^p = \frac{2}{9}M(1+2K_0)\bar{\sigma}\mathrm{d}\bar{\varepsilon}^p + \frac{\Gamma \mathrm{d}S}{V_s(1+e)} \tag{2.8}$$

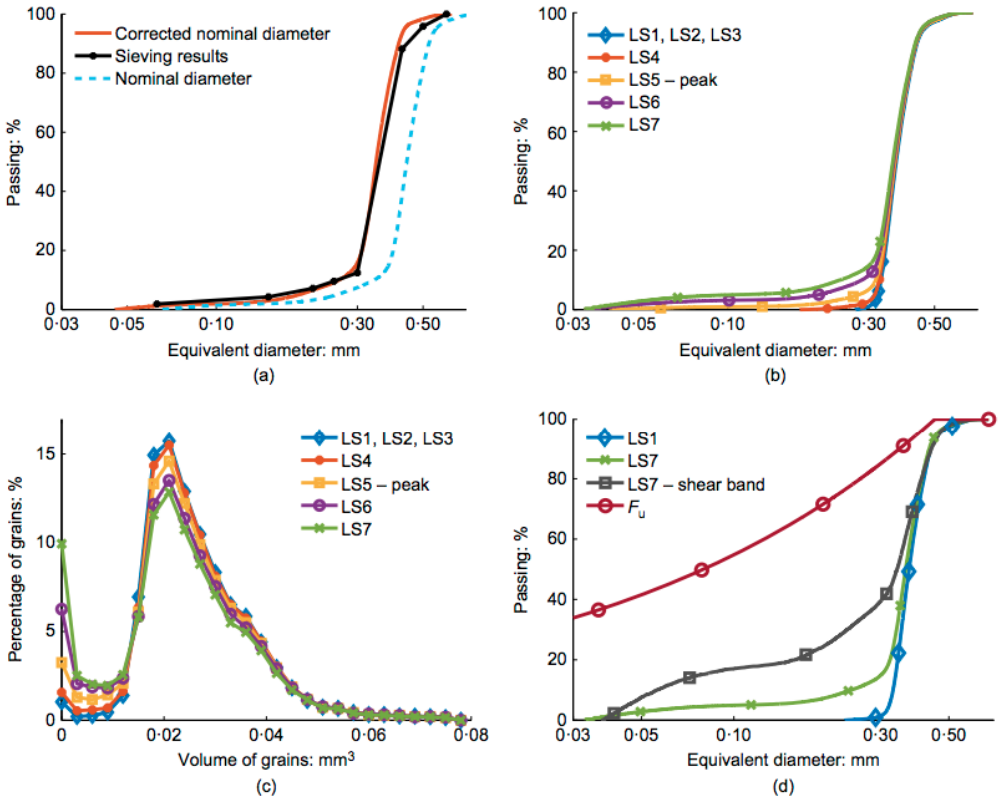

Figure 2.8: Breakage evolution obtained by image processing in high-confinement triaxial compression tests of sand [49]

where $\bar{\sigma}$ is the axial stress and $\bar{\varepsilon}$ is the corresponding axial strain. K_0 is the stress ratio, M is the slope of the critical state line in the $p-q$ space, Γ is the free surface energy, V_s is the volume of solid grains in the sample and e is the void ratio. This equation relates stress, strain and surface increase, and is consistent with previous experimental results, in which it was noted that the increase of surface area is proportional to the plastic work [56]. Eq. 2.8 was used in a crushing simulation with a fractal distribution of triangle particles. The model can capture the main characteristics of the mechanical response of a crushable granular assembly subjected to one-dimensional compression. Note however that the model was not calibrated. Alternatively, grain crushing can be described macroscopically as accumulated plastic strain, based on the assumption that grain crushing reduces frictional properties. This crushing-induced plasticity model could capture the stress-dilatancy relationship of Pozzolana Nera (a pyroclastic deposit from Central Italy) [55].

Different from plasticity, breakage mechanics is a continuum mechanics theory established for crushable granular materials, based on statistical and thermodynamic principles [36]. The free energy density function is split into a function of the particle size d and a function of the void ratio e, as follows:

$$\hat{\psi} = f_{\psi}(d)\psi_r(e), \tag{2.9}$$

Assuming that the internal energy and that the rate of dissipation are additive, the Helmholtz free energy Ψ of the granular assembly, is expressed as

$$\Psi = \Psi_0(1-B) + \Psi_u B \tag{2.10}$$

where Ψ_0 and Ψ_u are the Helmholtz free energy at the beginning and ultimate stages, respectively. The increment of Helmholtz free energy is given as:

$$\delta\Psi = \frac{\partial\psi_r(e)}{\partial e}[(1-B)m_0 + Bm_u]\delta e + \psi_r(e)(m_u - m_0)\delta B \tag{2.11}$$

where m_0 and m_u are parameters related to the initial and ultimate particle size distributions, respectively. Resorting to a special case of degenerate Legendre transformation, the breakage yield function and the consistency condition are given as:

$$y_B = E_B(1-B)^2 - G_b \tag{2.12}$$

$$\delta E_B(1-B)^2 - 2E_B(1-B)\delta B = 0 \tag{2.13}$$

where E_B is the breakage potential and G_B is a material parameter used to scale the strain energy. The breakage criterion is based on the idea that the energy dissipated by breakage is equal to the loss in residual breakage energy (see Figure 2.9). During the crushing process, energy is dissipated not only by breakage, but also by friction, and both phenomnea are coupled [57]. A detailed analysis about this coupling is presented in Section 5.2. Breakage mechanics was used to study creep, permeability, cementation and wetting in soils [58, 10, 59, 60, 61].

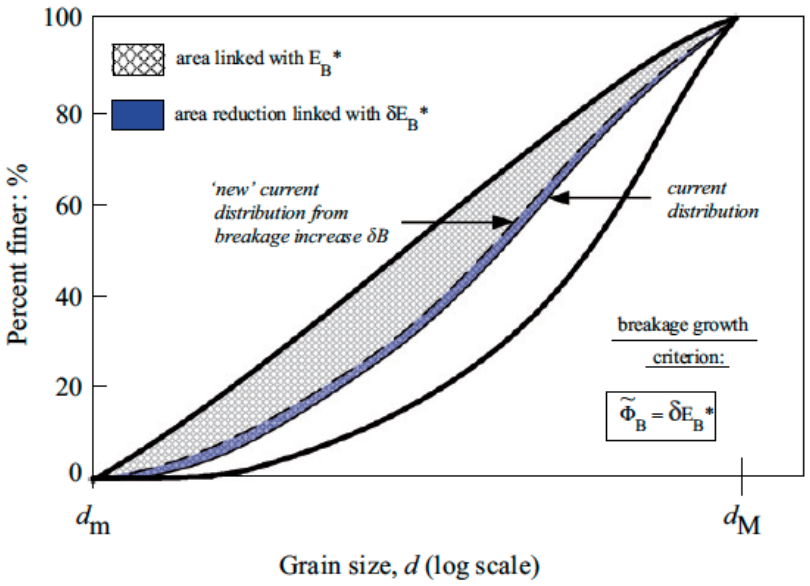

Figure 2.9: Physical meaning of the breakage criterion in breakage mechanics

Homogenization methods can also be used to predict the macroscopic behavior of com-

posite materials or aggregates [62]. Two steps are usually needed: the first is to calculate the stress and strain of an inclusion embedded into an infinite reference homogeneous medium; the second is to calculate the macoscopic stress and strain fields by means of a micro-macro relationship, which represents the interaction between the inclusion and the surrounding continuum medium. The dilute homogenization scheme is independent of the distribution of inclusions [63]. By contrast, the self-consistent method and Mori-Tanaka method allow accounting for interactions between inclusions. The self-consistent method is particularly suitable for disordered materials, in which no clear distinction can be made between the "inclusion" and the "matrix", because the material resembles a patchwork of different types of inclusions. For example, Hill's incremental inclusion-matrix relationship [64] is:

$$\delta\sigma - \delta\bar{\sigma} = -L^* : (\delta\epsilon - \delta\bar{\epsilon}) \tag{2.14}$$

where σ is the local stress, $\bar{\sigma}$ is the macroscopic stress, ϵ is the microscopic strain and $\bar{\epsilon}$ is the macroscopic strain. For spherical inclusions embedded in an isotropic linear elastic matrix, the Hill's tensor L^* is given by:

$$L^*_{ijkl} = \frac{\mu}{4-5\upsilon}[(3-5\upsilon)\delta_i j\delta_k l + \frac{7-5\upsilon}{2}(\delta_i k\delta_j l + \delta_i l\delta_j k)]. \tag{2.15}$$

Hill's theory was used to represent the breakage of crystals in polycrystalline structures [65]. Crystals of same orientation define a type of inclusion, which was assigned specific mechanical properties, such as strength. Broken grains were replaced by voids. Account for breakage in the calculation of local stress is explained in Table 2.1.

Table 2.1: Microscopic stress change due to grain breakage

	Microscopic stress	Microscopic deformation
Non-broken grains	$\delta\sigma = C_0 : \delta\epsilon$	$\delta\epsilon = [I + M^* : C_0]^{-1} : (\delta\bar{\epsilon} + M^* : \delta\bar{\sigma})$
Breaking grains	$\delta\sigma = -\sigma$	$\delta\epsilon = M^* : \sigma + \delta\bar{\epsilon} + M^* : \delta\bar{\sigma}$
Broken grains	$\delta\sigma = 0$	$\delta\epsilon = \delta\bar{\epsilon} + M^* : \delta\bar{\sigma}$

2.4 DEM models of particle breakage

The Discrete Element Method (DEM) allows simulating the mechanical response of granular assemblies and calculating quantities that cannot be observed by imaging, such as contact forces and grain stresses. Particle breakage can be simulated with the DEM by representing a crushable particle by a cluster of bonded elements (cluster method) or by replacing each broken particle with several fragments (replacement method). Upon proper calibration, DEM cluster models show good agreement with experimental results for single-particle crushing tests. The cluster method was also used to simulate oedometer tests with an assembly of crushable particles, but simulations required several tens of thousands of elements inside each cluster, and the computational cost was too high to ensure model practicality. Alternatively, in the replacement method, a stress criterion is employed to determine when a particle should break; the particle is then replaced by smaller elements representing fragments. The latter can be stand-alone particles, clusters or clumps. DEM breakage models were used to understand the influence of the loading speed, the packing of elementary particles, the number oand size of internal flaws and the number of elementary particles in a cluster [16, 6, 52, 14]. In the following, we discuss the pros and the cons of the cluster and substitution methods.

2.4.1 Cluster Method

In the cluster method, the crushable particle consists of smaller elementary particles that are bonded together. Elementary particles are usually (not always) uncrushable and equally sized. Different types of bonds can be used for different types of crushing mechanisms. As an example, the parallel bond model was used in Chapter 3. The cluster method is widely used in DEM.

Cheng and collaborators [14] simulated an isotropic compression test performed on sand, with 389 crushable sand particles represented by clusters, as shown in Figure 2.10a.

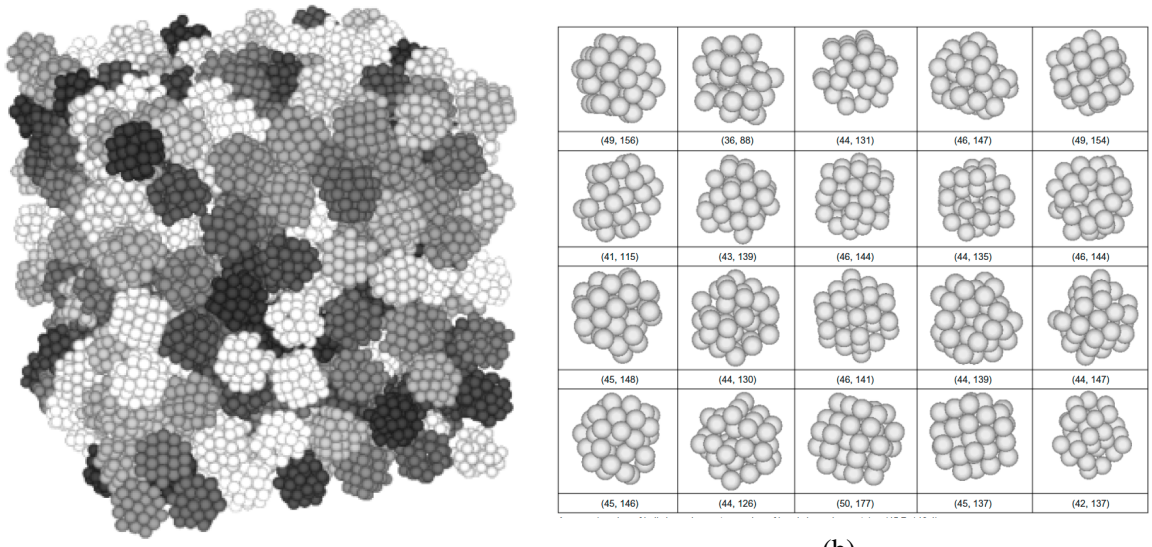

(a) (b)

Figure 2.10: Simulation of sand isotropic compression tests: (a) cubical arrangement of 389 agglomerates; (b) typical shape of a crushable 'grain'[14]

When generating the clusters, 20% of the elementary particles were randomly deleted to provide statistical variability. The shapes of the clusters and the corresponding arrangement of elementary particles are shown in Figure 2.10b.

Many subsequent studies [21, 66, 67] resorted to a similar cluster model. A bond model was introduced in the simulation of an isotropic compression test to represent the transmission of not only normal and shear stresses, but also bending moment. The elementary particle diameter was fixed to 0.2 mm and 1040 clusters with diameters ranging from 0.7 mm to 2 mm were generated [68]. Realizing that equally sized elementary particles may lead to unrealistic fractures that align with the lattice direction, Abe introduced clusters with a random size distribution and packing of elementary particles [69]. DEM simulations of shear tests resulted in microstructures comparable to those of natural gouges.

In all the techniques employed to account for the statistical variability of clusters, the accuracy of the cluster model largely depends on the number of elementary particles present in the clusters. In Cheng's work [14], each cluster had around 50 particles. Lim and McDowell [52] found that a minimum of around 500 particles is necessary to give accurate

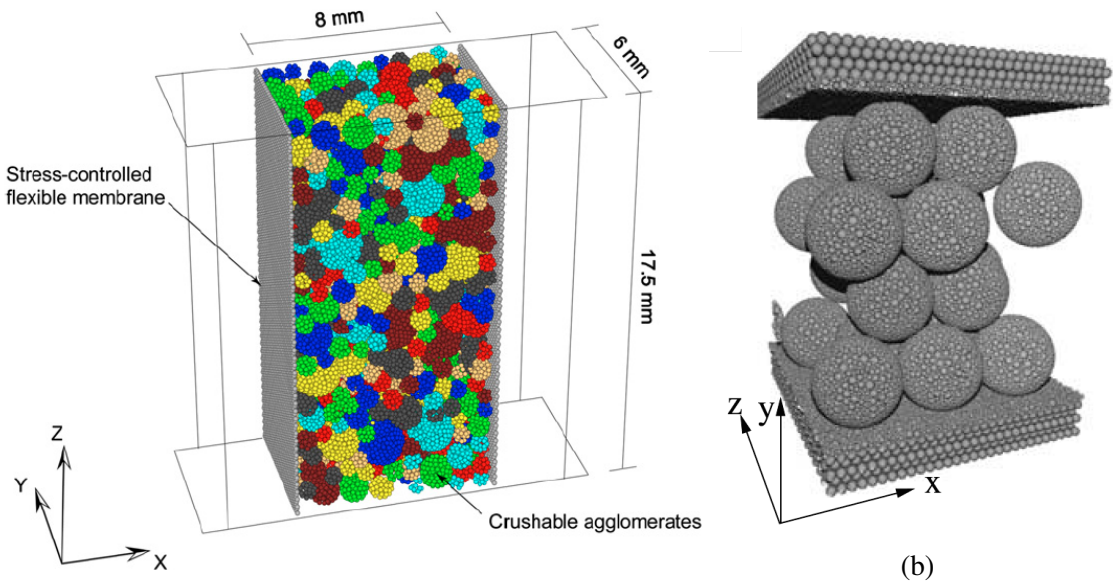

(a) (b)

Figure 2.11: Cluser method: (a) Equally sized elementary particles [68]; (b) Elementary particles with different sizes [69]

results. In Chapter 3, we found that the ratio of particle size/cluster size should be less than 0.014 – which implies that each cluster should have at least 37,000 elementary particles. With such a high number of particles in each cluster, it is highly computationally expensive to conduct simulations on complete grain assemblies. As an example, the DEM simulation of the single particle took 5 to 6 hours with a workstation (i7-3770 3.4GHz CPU and 64 GB RAM). To simulate mechanical tests on granular assemblies, at least few hundred of clusters have to be modeled.

2.4.2 Replacement Method

In the replacement method, the breakage criterion, *i.e.* the limit condition of the crushable particle, needs to be defined in terms of mean stress, tensile strength, shear strength, or maximum contact force, depending on the breakage mechanism. This limit condition can be defined by a single value or by a variable that follows a statistical distribution [70, 71]. Due to the difficulty in obtaining the stress distribution in a particle subjected to several

contact forces, the following simplified stress averaging method is often adopted [72]:

$$\sigma_{ij} = \frac{1}{V} \sum_{N_c} (x_i^{(c)} - x_i^{(p)}) F_j^{(c,p)} \tag{2.16}$$

where V is the volume of the particle, N_c is the total number of contacts, $x^{(c)}$ and $x^{(p)}$ are the locations of the contact point and particle centroid, respectively, and $F_j^{(c,p)}$ is the force acting on the particle at the jth contact. Åström and Herrmann compared two dfferent limit conditions for breakage, the mean stress and the largest compressive contact force. They found that using mean stress as a criterion led to unstable breakage. Contrarily, a criterion based on the largest compressive force predicts stable breakage mechanisms and more accurate PSDs [73]. However, the authors did not provide the expression of the average contact force that they used in the mean stress method, neither did they calibrate the numerical results against experiments. In another study, a grain was set to crush when the arithmetic mean of the normal contact force exceeds a critical value, F_{crit}^*, and a grain crushes when $\bar{F}_n > F_{crit}^*$ [74]. By investigating two breakage criteria and several configurations of post-crushing replacement, it was concluded that the expected ultimate fractal distribution of particle sizes could be approached irrespective of the breakage criterion used.

Ciantia and collaborators used the maximum normal contact force in the limiting criterion $F \leq \sigma_{lim} A_F = F_{lim}$, where F is the maximum normal contact force, σ_{lim} is the limit strength (which is a function of Poission's ratio, tensile and uniaxial compressive strengths), and A_F is the contact area [71]. 3D simulations of an oedometer test showed that this criterion was computationally efficient and accurate. A criterion expressed in maximum contact force was also used in [75], and later this criterion proved to better represent the PSD evolution and the average stress distribution [72].

In most single particle compression tests, breakage was found to be caused by tensile stress, splitting the grain axially, like in a Brazilian test [11]. According to Tsongui and collaborators [76], when a grain is in contact with several neighbours, the tensile stress

at the centre is close to $(\sigma_1 - 3\sigma_3)/2$. An oedometric compression test was simulated in 2D with a DEM model in which $(\sigma_1 - 3\sigma_3)/2$ was set as the failure criterion, and a good agreement was found with experimental results.

In another approach, McDowell and collaborators defined the breakage criterion in terms of octahedral shear stress, $q = 1/3[(\sigma_1 - \sigma_2)^2 + (\sigma_2 - \sigma_3)^2 + (\sigma_1 - \sigma_3)^2]^{1/2}$ [77]. They proposed that it would be unlikely for a particle to break when it is subjected to a high isotropic stress, and therefore that the deviatoric stress played a more important role in breakage. They used the model to simulate the isotropic compression of silica sand and achieved a normal compression line of the same slope as in experimental results from a 1D compression test.

Once the breakage threshold is reached, the crushable particle is replaced by smaller elements that represent the fragments. Different fragmentation methods were proposed, based on mass conservation, PSD evolution and various breakage mechanisms. McDowell and de Bono introduced two equally sized spheres to replace the broken particle, without mass loss, as shown in Figure 2.12(a) [17]. The axis joining the two centres is in the direction of the minor principal stress, which is similar to the breakage configuration in a single particle compression test. However, the main problem in this method is the development of a high elastic stress due to the overlap of the particles. Assuming that particle breakage is the result of tensile failure, Lobo-Guerrero and collaborators used a group of eight particles to replace the broken particle [18]. The axis joining the two largest fragments is perpendicular to the direction of maximum contact force, see Figure 2.12(b). Ben-Nun and Einav studied particle breakage in three configurations, one of which is shown in Figure 2.12(c). In the three configurations, they obtained a PSD that obeyed a power-law, scaling with three different fractal dimensions [78]. In terms of 3D simulations, Ciantia and collaborators conducted a parametric study on the effect of the splitting configuration and found that the mechanical response does not change significantly when there are more than 14 particles in the fragments. The geometric assumptions of the 14-particle replacement

method, shown in Figure 2.12(d), are also based on the observation of the breakage of a single particle subjected to diametric loads.

In summary, the maximum contact force method (or the induced stress) yields the best results and it has been recently accepted by researchers as the most appropriate breakage criterion. Although this method seems biased due to the absence of account for the coordination number or the spatial distribution of contact forces, it ensures that small particles are more likely to break while large particles are protected by smaller ones, which is usually true in experiments [72]. In terms of fragment geometric configuration, previous models share some interesting similarities: fragments are separate (no bond connection), have a disc shape (spherical shape in 3D) and there are fragments passing through the breakage plane. From previous studies [79, 76], fragments of broken particles remain close to their mother particles. While in the breakage models mentioned earlier, where there are no bonds among fragments, spherical particles have much less interlocking than real angular fragments observed in experiments [28]. Unbonded fragments thus undergo large displacements away from their mother particle's position. In addition, it is also clear that for both axial splitting and multi-fragmentation in our tests, none or very few fragments pass through the breakage plane, while contacts always do [80]. The last observations, which contradict previous fragment configurations, made us think of a more realistic arrangement of fragments to model particle breakage, which will be discussed in detail in Section 4.4.

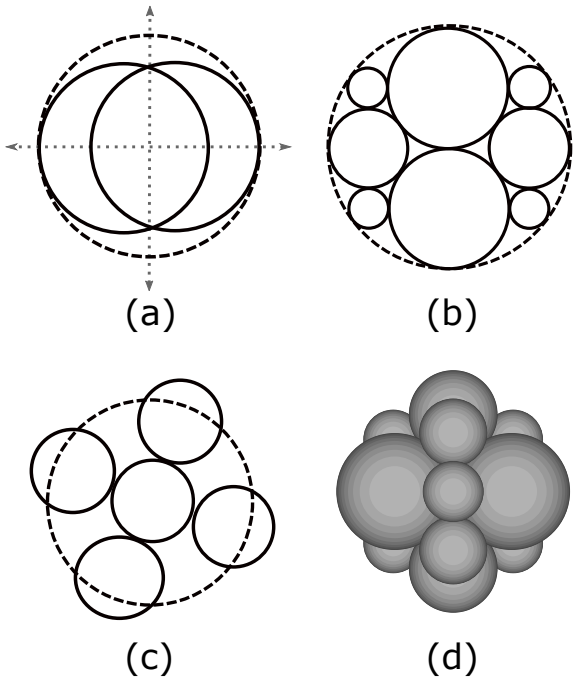

Figure 2.12: Examples of fragment arrangements [17, 18, 78, 19]

CHAPTER 3
DISCRETE ELEMENT MODELING OF SHIELDING AND SIZE EFFECTS DURING SINGLE PARTICLE CRUSHING

3.1 Introduction

It is well known that the probability of crushing decreases with the particle's coordination number. The mechanism can be explained by the redistribution of concentrated compression forces at particle contacts into a distributed pressure close to hydrostatic conditions, which reduces the tensile stress in the grains. A few analytical models were proposed to understand this phenomenon, known as "shielding effect". Jaeger [27] derived the expression of stress in the section of a cylinder subjected to four compressive line loads positioned 45^o apart from each other in the section. The analytical solution shows that the maximum tensile stress and the corresponding breakage force are less than in the case of a cylinder loaded with only two line loads positioned 90^o apart. Tsoungui modeled contact forces applied to a particle by calculating four equivalent contact forces in two principal directions, and expressed the principal stresses and maximum tensile stresses in the particle [76]. The tensile stress was compared to the particle strength to predict fracture propagation and crushing at the particle scale. Unfortunately the solution was only provided for 2D problems and the calculation method assumes that the particle cannot break if the two principal stresses are equal, which is not practical for sand or rock particles. Recently, Salami *et al* [13] constructed a new particle crushing device and analyzed the effect of the coordination number on grain strength. Grains had a cylindrical shape and were subjected to multi-axial compression tests. Results showed that grain crushing depends both on the number and position of contact forces. Both tensile and shear cracks were observed. However, it has to be noted that the tests were restricted to grains with a coordination number less than, or

equal to 6, which is not repreentative of particles that are part of a well graded granular assembly. In studies based on the Distinct Element Method (DEM), the influence of the number of contacts between crushable particles, modeled as clusters of bonded elementary particles ("balls"), was not examined. Instead, authors focused on the number of contacts (or bonds) of the elementary balls making the cluster [52][81]. Therefore, the influence of the coordination number on particle crushing is still not fully understood.

Statistically, the largest particles in a granular assembly have the highest coordination number. Therefore, due to the shielding effects, the probability of breakage of a particle should decrease as the relative size of that particle (i.e. the actual particle size divided by the average particle size in the assembly) increases. However the strength of a particle also depends on the size of that particle, regardless of the coordination number. This size effect was noted in strength test experiments performed in concrete structures, rock samples and granular materials [82][43][44]. If one accepts that larger particles tend to have larger internal flaws than smaller particles, then it is possible to explain, based on the Griffith's theory, why particle strength decreases as particle size increases [83][84]. Several empirical equations were obtained from single-particle uniaxial compression tests, in order to relate particle strength to particle size. For instance, Hiramatsu [11] studied the stress distribution in a single particle subjected to a concentrated load by means of photo-elastic experiments and mathematical analysis. In order to predict the strength of real rock particles, a fitting parameter (κ) was introduced in the analytical expression of stress in a spherical particle:

$$\sigma_f = \frac{\kappa F_f}{d^2}, \tag{3.1}$$

where σ_f is the tensile stress at failure, F_f is the corresponding compressive force applied and d is a characteristic particle dimension. The value of κ was fitted to experimental results obtained during compression tests. Several values were reported: $\kappa = 0.9$ in [11]; $\kappa = 0.58$ and $\kappa = 0.82$ in [85]. Based on single-particle compression tests, Lee [86] proposed the

following relationship between particle strength and particle size:

$$\sigma_f = Kd^b. \tag{3.2}$$

The size effect parameter b, which is the slope of the force-size curve in logarithmic co-ordinates, is typically a negative number, in the order of -1 to -0.1. Equations 3.1 and 3.2 suggest that the peak force F_f is proportional to an exponent of the particle size (d^α). This hypothesis was verified by another empirical study [82], which showed that for α smaller than 2.0, tensile strength decreases when particle size increases.

The Weibull theory can be used to predict the probability of failure of a particle that contains flaws of various sizes, or the probability of survival (i.e. the probability of non crushing) of a particle of a given size inside a granular assembly [87][6]. At the particle scale, the Weibull theory was used to predict the breakage force for clusters of various sizes, made of bonded particles and internal flaws [52]. However the porosity of the clusters was not provided, which made it impossible to explain size effects, because the influence of the flaw size cannot be distinguished from that of the number of flaws or that of the flaw volumetric fraction. Weibull models can be fitted to predict force-displacement curves and particle size distributions observed during compression tests performed in the laboratory or simulated with the DEM. However, there is still a lack of understanding of what originates size effects, and how size effects counter-act shielding effects in the process of crushing.

In this chapter, we analyze separately shielding and size effects with a DEM model of single-particle crushing designed with PFC3D 4.0. We calibrate our cluster model against published force-displacement curves obtained during sand particle crushing tests. The strength predicted by the model is verified by applying the Buckingham Π theorem (Section 3.2.3). We apply reaction forces to the cluster to replicate the confining effect of neighboring particles, and we simulate compression by increasing the value of the top and bottom reaction forces. We then express a relationship between the breakage force and

the coordination number (Section 3.3). Lastly, we simulate single particle crushing with various cluster sizes, cluster porosities, flaw sizes and number of flaws (Section 3.4).

3.2 DEM Model of Crushable Particle

3.2.1 Constitutive Model Used in the Particle Flow Code (PFC3D)

In the following, we represent a crushable particle as a spherical cluster of bonded, hexagonally packed, equally sized, non-breakable spheres ("balls"). Cluster crushing is modeled as bond breakage. The simulations are conducted with PFC3D, a DEM program introduced by Cundall and Strack [88] and then further developed by Itasca [89]. In PFC3D, rigid "balls" and rigid "walls" are allowed to overlap over a contact area of negligible size compared to that of the balls. Balls can be bonded together to form clusters of different sizes and shapes. The cluster designed in PFC3D is governed by three constitutive laws: a ball contact-stiffness model, a ball slip model and a bond model. Interactions between bonded balls are governed by these three laws simultaneously. Once the strength (tensile or shear) of a bond is reached during loading, the bond breaks and is deleted from the cluster model.

We use a linear contact-stiffness model, in which the relationship between the force and the relative displacement at the $i-th$ ball contact is expressed as:

$$F_i^n = k^n U^n n_i,\ \Delta F_i^s = -k^s \Delta U_i^s \tag{3.3}$$

where F_i^n and ΔF_i^s are respectively the normal contact force and shear force-increment; k^n and k^s are respectively the normal stiffness and the shear stiffness at the contact; U^n is the normal overlap between the two balls in contact; n_i is the unit vector along the line that links the two ball centers; and U_i^s is the shear component of the increment of contact displacement. Note that the linear contact-stiffness model assumes that the normal and shear stiffnesses of the contact do not depend on the displacement vector.

In the slip model used in the simulations, the maximum shear force at a contact is expressed as:

$$F^s_{max} = \mu |F^n_i| \tag{3.4}$$

If $|F^s_i| > F^s_{max}$, then slip occurs and the magnitude of F^s_i is set to F^s_{max}. We use the parallel bond model, in which bonds between balls are represented as short beams of circular cross-section ("disks"). Parallel bonds transmit both forces ($\bar{F}_i$) and moments ($\bar{M}_i$), which are split into a component normal to the contact plane ($\bar{F}^n_i$, $\bar{M}^n_i$) and a shear component contained in the contact plane ($\bar{F}^s_i$, $\bar{M}^s_i$), as follows:

$$\bar{F}_i = \bar{F}^n_i + \bar{F}^s_i, \quad \bar{M}_i = \bar{M}^n_i + \bar{M}^s_i \tag{3.5}$$

The bond model depends on five parameters: the normal and shear stiffnesses ($\bar{k}^n$ and $\bar{k}^s$); the normal and shear strengths ($\bar{\sigma}_c$ and $\bar{\tau}_c$); and the radius of the bond cross section ($\bar{R}$). The increments of elastic force and moment are calculated as follows:

$$\Delta \bar{F}^n_i = (-\bar{k}^n A \Delta U^n) n_i, \; \Delta \bar{F}^s_i = -\bar{k}^s A \Delta U^s_i \tag{3.6}$$

$$\Delta \bar{M}^n_i = (-\bar{k}^s \boldsymbol{J} \Delta \theta^n) n_i, \; \Delta \bar{M}^s_i = -\bar{k}^n \boldsymbol{I} \Delta \theta^s_i \tag{3.7}$$

In which θ^n and θ^s_i are the incremental angles and A is the area of the disk that forms the cross section area of the bond ($A = \pi \bar{R}^2$). $\boldsymbol{J}$ and $\boldsymbol{I}$ are the polar moments of inertia, calculated by $\boldsymbol{J} = \frac{1}{2}\pi \bar{R}^4$ and $I = \frac{1}{4}\pi \bar{R}^4$ respectively. Initially when a bond is created with PFC3D, internal bond forces and moments are set to zero. During a loading increment, the relative displacement and rotation between the two bonded balls generate an increment of force and moment. If the maximum tensile or shear stress exceeds the corresponding strength, then the parallel bond breaks and is deleted from the DEM model.

3.2.2 Model Calibration: Single Particle Crushing Simulation

In the following, we calibrate the five bond parameters of the DEM cluster model to match force-displacement curves obtained experimentally during single-particle crushing tests performed on sand [90]. In order to reproduce the conditions of the experiment, the diameter of the cluster was set to 0.729mm (which is the diameter of the sand grains). In order to minimize the rotation of the cluster and the yielding of asperities before the first fragmentation [91][14], we deleted a few layers of rigid balls at the top and bottom of the cluster. The diameter of the cluster was reduced by 5% in the axial direction, and maintained as such in the lateral direction. The model contained 11,000 rigid balls, which allowed considering the cluster as a Representative Elementary Volume (REV) of bonded particles [52]. We arranged the rigid balls into a Hexagonal Close Packing (HCP) in order to maximize the density of the cluster and the number of contacts of the balls in the cluster, and therefore get a representative model of crushable particle without flaws, as advocated in previous studies conducted with PFC3D [90][12][16]. The loading platens were modeled by disk-shaped rigid walls (e.g., [92]). The diameter of the disk walls was equal to that of the cluster. In order to model the platens as rigid bodies, the stiffness of the walls was set to 1×10^{30}N/m, i.e. several orders of magnitude higher than the stiffness of the balls and of the bonds.

The cluster was subjected to gravity forces before being compressed axially. During the loading phase, the top and bottom walls were subjected to a constant velocity, which was chosen small enough to simulate a quasi-static loading (note that the breakage force depends on the loading velocity otherwise). The DEM algorithm is stable only if the time step chosen for the loading increments is smaller than a critical value, which depends the mass and stiffness of each ball and is of the order of 10^{-7} to 10^{-9} s for soils and rocks [89]. Loading velocities ranging from 0.2 to 1.28m/s were used in [16][93][94]; these high loading increments were chosen to ensure algorithm stability while reducing the simulation time. By contrast, we used differential density scaling, which consists in calculating a fictitious

Table 3.1: Parameters used in DEM simulations

Diameter of sphere (R)	mm	1.4×10^{-2}
Density of sphere (ρ)	kg/m^3	3581
Normal and shear stiffness of each sphere (k^n and k^s)	N/m	1×10^5
Normal and shear bond strength (σ_c and τ_c)	MPa	130
Normal and shear stiffness of parallel bond ($\bar{k}^n$ and $\bar{k}^s$)	N/m^3	1.6×10^{13}
Frictional coefficient of sphere (μ)	-	0.5

inertial mass for each particle at the the beginning of each timestep, such that the model's stable timestep is unity. Differential density scaling allows applying a low wall velocity (to ensure quasi-static loading conditions) with a reduced number of load steps. The loading rate applied in the simulations presented in the following was 5×10^{-7}mm/s. During the entire simulation, we monitored the intensity of the contact forces at the walls, the displacements of the walls and the number of broken bonds. The five DEM bond parameters were fit to match the force intensity and wall displacement obtained experimentally at the first peak of the force-displacement curve (i.e., at the first fragmentation). The calibrated parameters are listed in Table 4.2.

The HCP of rigid balls has symmetries. In order to assess the potential anisotropy induced by the HCP orientation on cluster mechanical properties, we compared the results obtained with the set of DEM bond parameters reported in Table 4.2 for the following HCP orientations (in reference to the horizontal): $0°$(horizontal), $30°$, $45°$, $60°$ and $90°$(vertical). The test set upq for angles $0°$ and $45°$ are shown in Figure 3.1. Figure 3.2 shows the force-displacement curves obtained during the simulations. All HCP orientations exhibit similar trends. After the first fragmentation, internal forces in the cluster are relaxed, which explains the sudden drop of force after the peak. At larger orientation angles (i.e., when the HCP orientation deviates from the horizontal), the breakage plane is more likely to be parallel to the HCP layers. For an angle of $0°$ (i.e, horizontal HCP), the breakage plane is vertical (i.e. perpendicular to the lattice), which is similar to what is observed in Brazilian tests performed on rock samples. It is noteworthy that for the vertical HCP, a force drop

occurred before the first fragmentation (point A in Figure 3.2). According to the video generated during the simulation, this drop, although small, actually corresponded to a rotation of the cluster and the yielding of some asperities. The particle broke after rotation, when the axis of the loading was alined with a plane of weakness of the cluster. To avoid rotation, we present results obtained with the horizontal HCP model, which is used in all the following simulations for consistency.

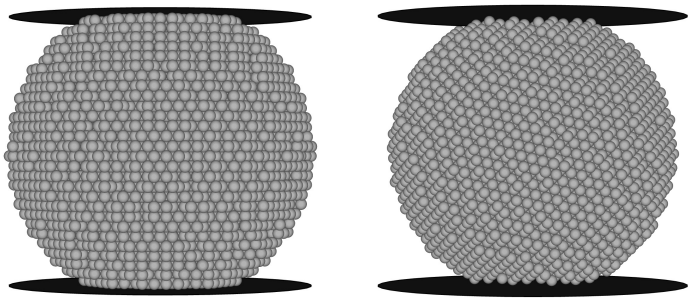

Figure 3.1: Cluster formed by bonded non-breakable spheres arranged into a Hexagonal Close Packing (HCP). a. HCP orientation of 0° to the horizontal plane ("Horizontal HCP"). b. HCP orientation of 45° to the horizontal plane.

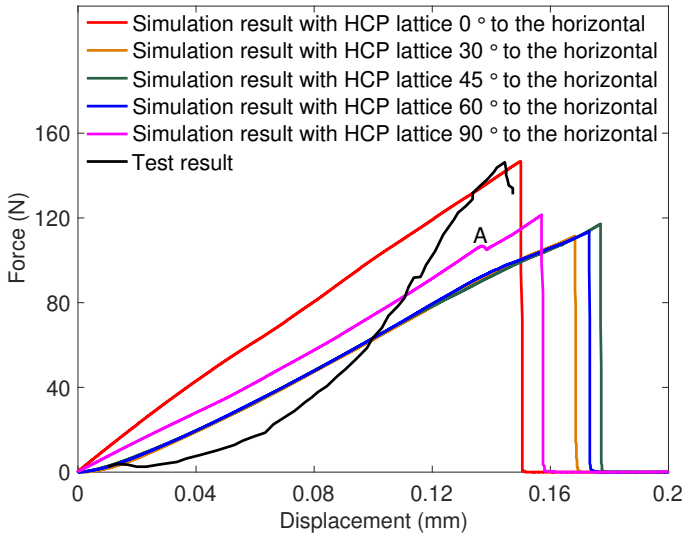

Figure 3.2: Force-displacement curves during a uniaxial compression test simulated up to the first fragmentation: calibration of the DEM cluster model against experimental test results, with various HCP orientations (in reference to the horizontal plane).

Note that since the balls and bonds obey a linear elastic behavior before breakage, the force-displacement curve is linear before the first peak. In the experiment, the curve is non-linear due to the presence of heterogeneities in the particle and due to the expansion of contact areas during compression, which increases particle stiffness. Typical simulation results are shown in Figure 3.3, in which we can see that due to the symmetry imposed to the model, the particle breaks along the loading axis. When the first peak force is reached, the cluster breaks into four main pieces and a number of smaller fragments, which is in agreement with experimental observations [90].

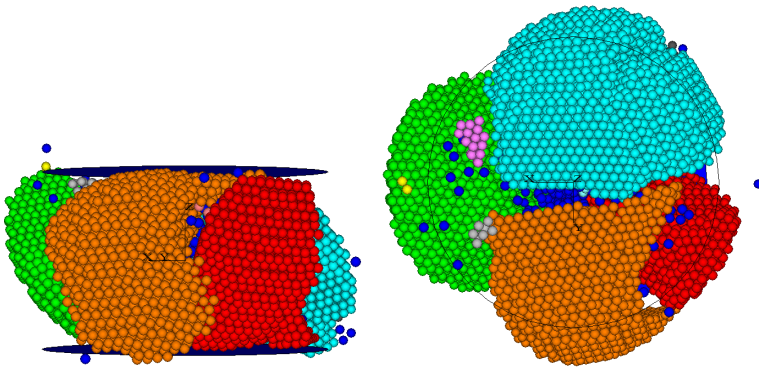

Figure 3.3: Lateral view (left) and top view (right) of the cluster after the first fragmentation.

3.2.3 Model Validation Using the Buckingham Π Theorem

According to the Buckingham Π theorem, physical laws should not depend on the units of measurement [95]. Huang [96] indicated that for a DEM model that contains bonded balls, the set of micro-parameters that control macro-properties should be $\{k_n, k_s, T_n, T_s, \mu, R, n, \rho, L, V\}$, where T_n and T_s are respectively the normal and shear strengths of the contact bonds, R is the average ball size, n is the porosity, ρ is the mass density of the elementary balls, L is the sample size and V is the loading speed. The failure of the specimen is governed by the following dimensionless parameters: $\{k_nR/T_n, T_n/T_s, \mu, k_s/k_n, n, R/L, V/\sqrt{k_n/\rho}\}$. In the present case, the ratio $V/\sqrt{k_n/\rho}$ can be ignored because the loading

is quasi-static. In order to simplify the analyses with the parallel bond model, we replace the contact bond strengths T_n and T_s (defined in force) by the strengths σ_c and τ_c (defined in stress). After introducing the normal and shear parallel bond stiffnesses $\bar{k}^n$ and $\bar{k}^s$, two dimensionless parameters are added to the list of controlling variables: the ratio of parallel bond normal stiffness and parallel bond shear stiffness $\bar{k}^n/\bar{k}^s$, and the ratio of parallel bond stiffness and ball stiffness $\bar{k}^n R^2/k_n$. Other studies indicate that the ball size also needs to be considered because it has effects on the behavior of particulate assemblies in PFC simulations [97][98][99]. Accordingly, we propose to express the relationship between micro-parameters and sample tensile strength (σ_t) as:

$$\sigma_t = \sigma_c \Phi(\frac{k_n}{\sigma_c R}, \frac{\sigma_c}{\tau_c}, \mu, \frac{k_n}{k_s}, \frac{L}{R}, \frac{\bar{k}^n R^2}{k_n}, \frac{\bar{k}^n}{\bar{k}^s}) \tag{3.8}$$

We simulated a uniaxial compression for several cluster sizes. The ball size R, the contact normal stiffness k_n and the parallel bond stiffnesses $\bar{k}^n$ and $\bar{k}^s$ were adjusted in order to maintain all the dimensionless DEM parameters constant. We observe that the breakage force increases according to a power law (Figure 3.4) but that the strength of the cluster remains fairly constant (Figure 3.5). The result are in agreement with the Buckingham Π theorem, which states that under constant DEM non-dimensional parameters, the cluster strength should be the same for all cluster sizes tested (Equation 3.8).

3.3 Modeling of the Shielding Effect

We now use the calibrated cluster model presented in Section 3.2 to simulate shielding effects at the particle scale. Particles neighboring the cluster are represented by walls that produce a reaction force at the boundaries of the cluster. This modeling strategy allows uncoupling the variation of the coordination number from the rearrangement of the fabric that is expected to occur during crushing. Statistically, the coordination number in a granular material increases when the contrast in size between particles is large. The surface area

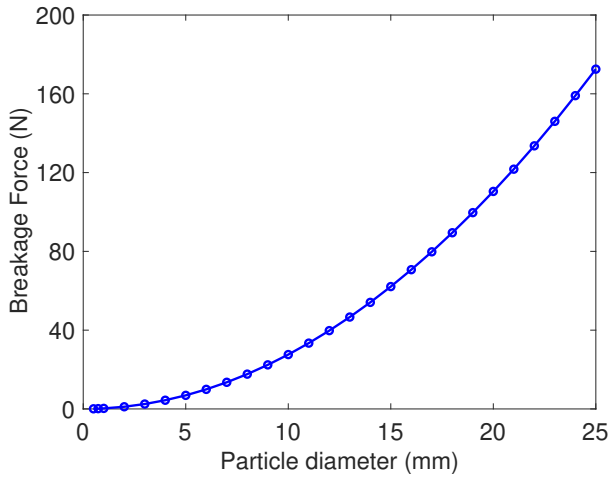

Figure 3.4: Validation of the cluster model with the Π theorem: variations of the breakage force with the cluster size.

(which determines the maximum coordination number) is proportional to d^2 (in which d is the diameter of the particle). In well-graded sands and rocks which contain both fine- and coarse-grained soils, the value of d_{max}/d_{min} often exceeds 10 [100], which implies a difference of surface are of two orders of magnitude and therefore, high coordination numbers. A broad range of coordination numbers (i.e., up to 120) is explored in order to check whether shielding effects can be explained by a redistribution of contact forces from a set of punctual loads (applied over a limited number of neighboring grains) to a quasi-hydrostatic stress (applied through a high number of contacts). The cluster is axially loaded by the top and bottom walls (called the loading walls in the following), and confined by passive walls (called shielding walls in the following). We vary the number of shielding walls in order to establish a relationship between the coordination number of a particle and the axial force needed to trigger the first fragmentation.

3.3.1 Construction of the DEM Shielding Model

The shielding model was obtained in four steps, as shown in Figure 3.6:

1. Generate the cluster and the loading walls. This step was similar to that used for the simulations presented in Section 3.2.2 for calibration.

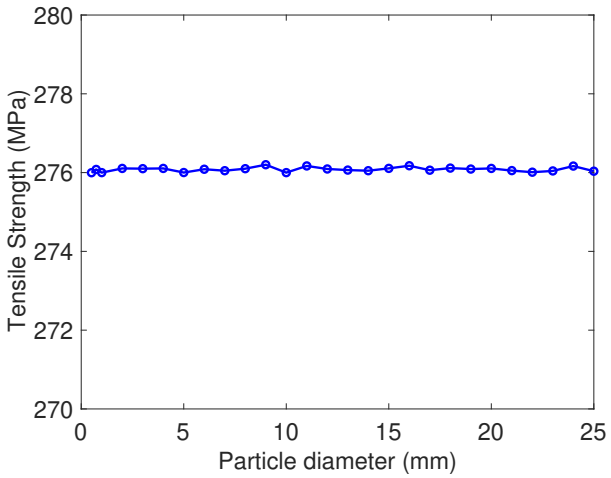

Figure 3.5: Validation of the cluster model with the Π theorem: variations of the cluster strength with the cluster size.

2. Generate the shielding walls. Shielding walls were modeled as small disk walls that are tangent to the cluster. The radius of the shielding walls was 0.05mm (about 3 times the radius of the non-breakable balls inside the cluster), which ensures that the shielding walls produce a confinement without punching the cluster. During the crushing process, shielding walls redistributed contact forces, which reduced concentrated compressive forces at the contacts and tensile stress in the cluster. For low coordination numbers (below 60), random wall distributions resulted in highly heterogeneous contact distributions on the cluster. Stress redistribution resulted in stress concentrations instead of the expected hydrostatic stress. Therefore, for a coordination number up to 60, shielding walls were positioned according to a symmetric distribution. Above 60, both symmetric and random wall distributions were investigated. The procedure adopted to generate symmetric wall distributions is explained in Figure 3.7 and Table 3.2. Random wall distributions were generated by random point picking, with normal vectors pointing towards the origin [101], as shown in Figure 3.8. An algorithm was written to delete overlapping shielding walls. Gravity forces were applied after all walls were created.

3. Generate reaction forces at the shielding walls. The shielding walls were displaced towards the center of the cluster under controlled velocity in order to ensure contact with the cluster. The velocity was set to 5×10^{-7}mm/s (same velocity as that used for calibration), until the first bond breakage occurred in the cluster. Since the total number of bonds exceeded 60,000, the effect of a single bond breakage on the fragmentation of the whole cluster was ignored. After the first bond breakage, the velocity of the shielding walls was set to zero.

4. Crush the cluster. The two loading walls were displaced at a velocity of 5×10^{-7}mm/s, while keeping the shielding walls at a fixed position. Reaction forces generated in the loading walls were monitored.

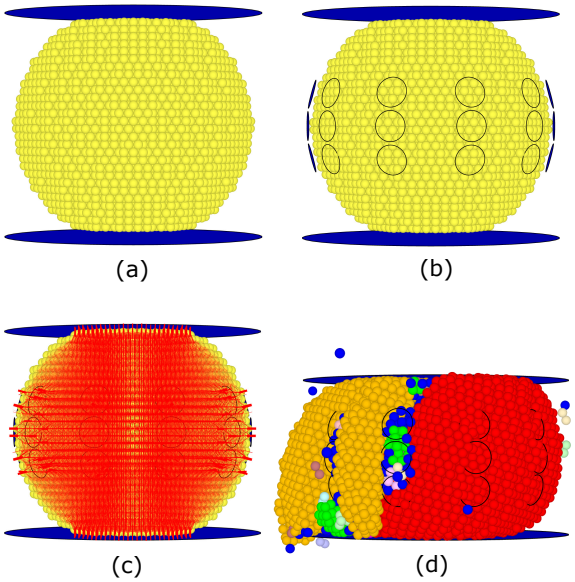

Figure 3.6: Steps to generate a shielding model in DEM. (a) Generate the cluster and loading walls. (b) Generate the shielding walls. (c) Generate the reaction forces at the shielding walls. (d) Crush the cluster.

3.3.2 Simulation Results

Figure 3.9 shows selected force-displacement curves obtained during the simulations. It is clear that the magnitudes of the peak force and of the wall displacements at the first

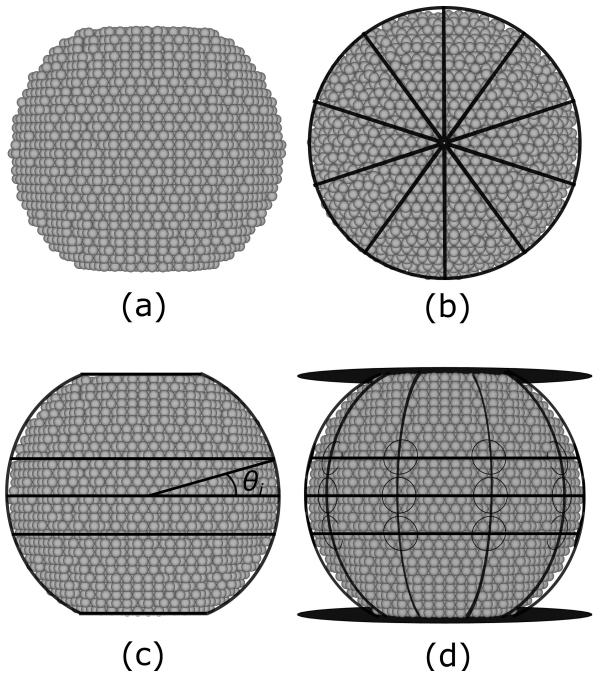

Figure 3.7: Procedure to generate a model with a symmetric distribution of 30 shielding walls (10×3): (a) generate the HCP cluster; (b) divide the cluster into ten longitudinal slices (top view); (c) find circles at a longitude θ_i (in reference to the horizontal) at the surface of the particle (side view); (d) generate walls at the intersection of the circles with the longitudinal lines (side view).

Table 3.2: Geometric parameters of the symmetric distribution of shielding walls. The number of walls $N = N_1 \times N_2$ is the product of the number of wall centroids in a plane (N_1) by the number of horizontal planes containing wall centroids (N_2). θ_i is the orientation of the wall centroids in reference to the horizontal.

Wall numbers	θ_i	Wall numbers	θ_i
$4 \times 1 = 4$	0	$8 \times 5 = 40$	$0, 15, 30$
$8 \times 1 = 8$	0	$15 \times 3 = 45$	$0, 15$
$10 \times 1 = 10$	0	$10 \times 5 = 50$	$0, 15, 30$
$12 \times 1 = 12$	0	$8 \times 7 = 56$	$0, 15, 30, 45$
$15 \times 1 = 15$	0	$12 \times 5 = 60$	$0, 15, 30$
$6 \times 3 = 18$	0,15	$10 \times 7 = 70$	$0, 15, 30, 45$
$8 \times 3 = 24$	0,15	$15 \times 5 = 75$	$0, 15, 30$
$10 \times 3 = 30$	0,15	$12 \times 7 = 84$	$0, 15, 30, 45$
$12 \times 3 = 36$	0,15	$15 \times 7 = 105$	$0, 15, 30, 45$

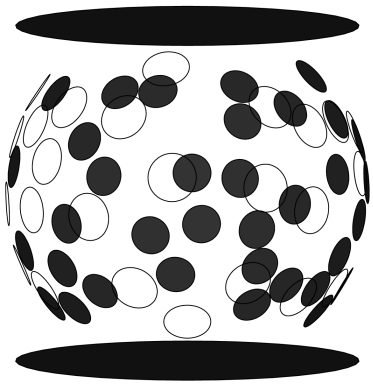

Figure 3.8: Random distribution of 60 shielding walls, generated by random point picking. An algorithm was written to avoid overlap between the shielding walls.

fragmentation both increase with the number of shielding walls. For samples with high coordination numbers, we observed that particle fragments were all confined within the volume delimited by the shielding walls during the crushing. Therefore contact was maintained between the cluster and the loading walls, which explains why the magnitude of the force drop was smaller for a higher number of contact walls. Figure 3.10 shows the evolution of the number of broken bonds with the loading displacement. The sudden force drop observed for low coordination numbers in Figure 3.9 translates into a very sharp increase of the number of broken bonds - as opposed to the more gradual bond breakage evolution noted for higher coordination numbers. Overall, the steady increase of peak force with the coordination number illustrates the occurrence of shielding effects for both symmetric and random distributions of walls. Figure 3.11 shows that the peak force reached at the first cluster fragmentation is approximately proportional to the number of shielding walls. A linear regression provided a slope of 1.31 for both symmetric and random wall distributions. This linear relationship can be used to optimize the size distribution and packing (thus coordination number) of crushable particles inside a granular assembly to avoid crushing under quasi-static axial loading.

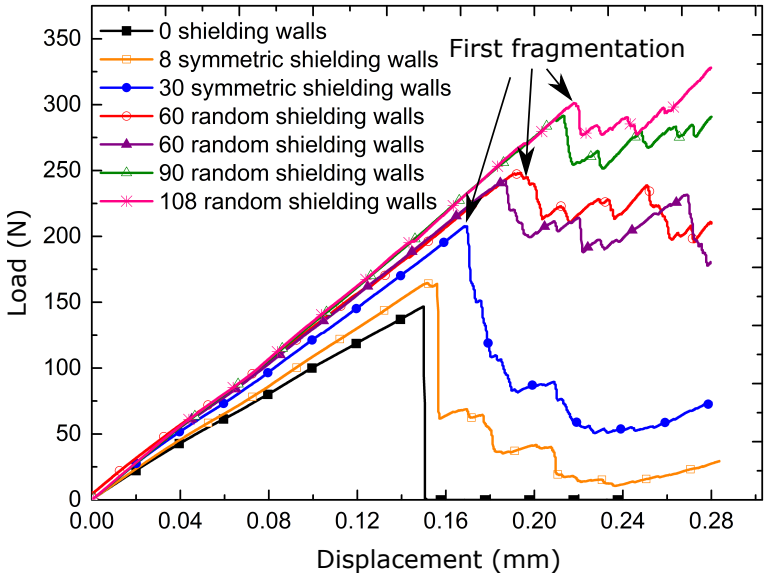

Figure 3.9: Force-displacement curve obtained with the shielding models.

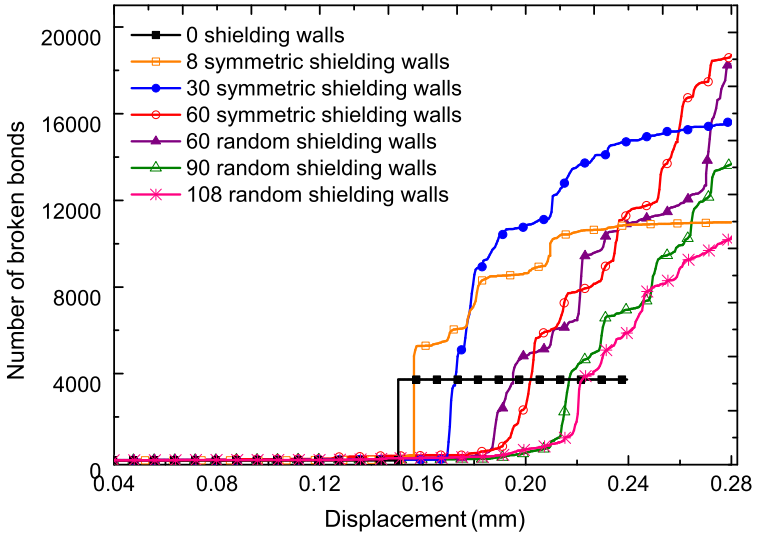

Figure 3.10: Evolution of the number of broken bonds with the cumulated displacement of the loading walls in the shielding models.

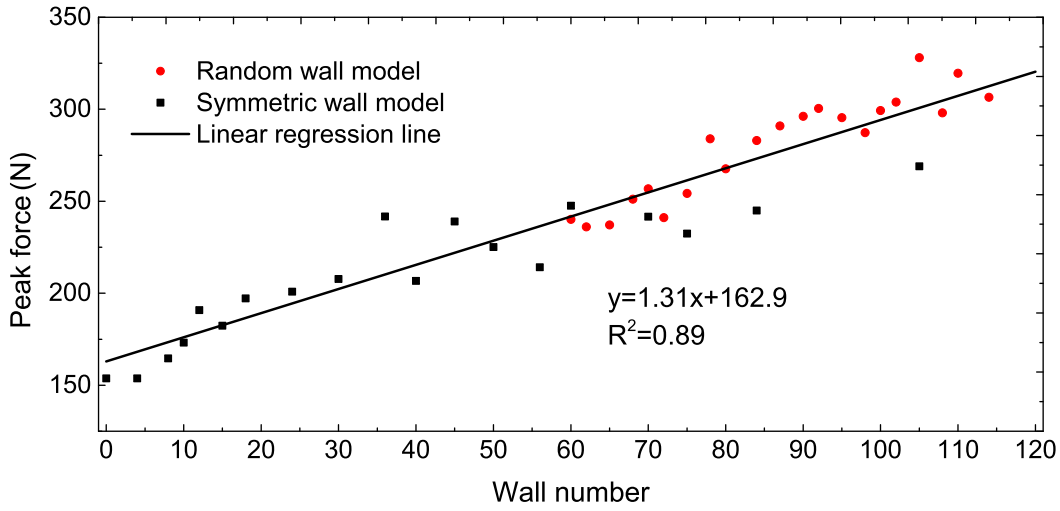

Figure 3.11: Relationship between the peak force reached at the first fragmentation and the number of shielding walls used in the simulations (coordination number of the cluster).

3.4 Modeling of the Size Effect

Numerous single-particle crushing experiments show that tensile strength increases when particle size decreases, which, according to previous studies, can be explained by the fact that smaller particles have less and smaller defects than larger particles [6]. The particle size exponent b in Equation 3.2 was found to be equal to -0.375, -0.343 and -0.420 for Leighton Buzzard sand, oolitic limestone and carboniferous limestone respectively [86]. In other materials, b was found to range between -0.7 and -0.3 [102, 103]. The micro-mechanical origin of size effects is still not fully understood. In the following, we explore several possible causes of size effects, including the particle size (with and without internal flaws), the flaw size, the number of flaws and the overall porosity of the crushable particle.

3.4.1 Effect of the Cluster Size, with and without Internal Flaws

We construct cluster models of various sizes, with the same elementary ball size and DEM parameters as those presented in Section 3.2.2. For each cluster size, we compare the results of uniaxial compression tests obtained with clusters that have 0% porosity (no internal

flaw; solid volume fraction of about 74%, i.e. maximum packing density) with those obtained with clusters that have 10% porosity (i.e. with internal flaws). Porosity was created by removing randomly 10% of the elementary balls forming the cluster. Clusters had a diameter ranging from 0.1mm (34 elementary balls) to 1.9mm (230,000 balls).

Figure 3.12 shows that the peak force at first fragmentation varies with the diameter of the cluster (representing the crushable particle) according to a power law. The exponent is 1.96 for 0% porosity and 1.86 for 10% porosity. According to Equation 3.2, this implies that the tensile strength is proportional to $d^{-0.04}$ (respectively $d^{-0.14}$) for 0% porosity (respectively 10% porosity), i.e. that the tensile strength is almost constant (respectively slightly decreases as the size of the particle increases) for 0% porosity (respectively for 10% porosity). This statement is confirmed by the results presented in Figure 3.13. For instance, for 0% porosity, the tensile strength varies between 250MPa and 290MPa for cluster sizes varying from 0.2 to 1.9mm respectively (i.e. the slope of strength/size curve amounts to less than 15% of the magnitude of the the tensile strength). Strength decreases with particle size for 10% porosity, which may be due to the higher number of voids at the contact between the particle and the platen, which increases the probability to initiate cracks in the contact zone. Since flaws were randomly distributed to create a 10% porosity, the average number of contacts between balls was uniformly decreased, which generated higher stress concentrations, and therefore, reduced the strength of the cluster. We note that in relation 3.2, the absolute value of the exponent b that we obtain in our simulations is much smaller than that measured in the laboratory, which confirms that particle size does not control particle strength.

We also note that the tensile strength converges to a constant value for clusters 1mm in size and above, i.e. for clusters that contain at least 37,000 elementary balls (which corresponds to a ratio ball size/cluster size smaller than 0.014). We claim that below a ratio

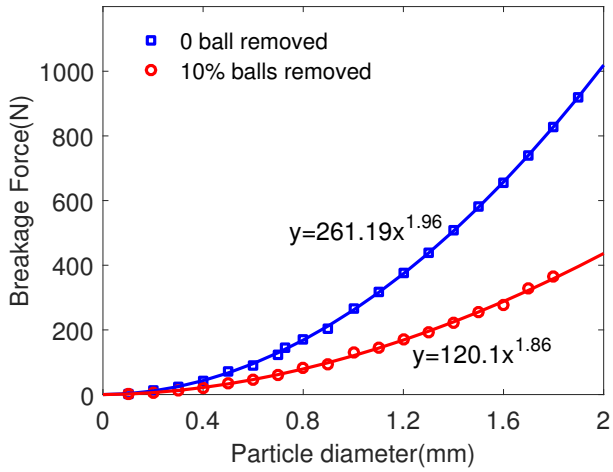

Figure 3.12: Relationship between the breakage force and the crushable particle size (fixed flaw size).

ball size/cluster size of 0.014, the cluster has an insufficient number of elementary balls to be considered as a REV. The results presented in Figure 3.13 indicate that for a fixed number of flaws (either zero flaw or a number of flaws equal to 10% of the elementary balls forming the cluster) and for a fixed flaw size (either null size or a size equal to the elementary ball size), size effects cannot be attributed to the size of the crushable particle.

3.4.2 Effect of the Flaw Size

According to Griffith theory, the strength of the crushable particle depends on the size of the largest flaw in that particle. In order to verify this statement, we simulated uniaxial compression tests with clusters that contained flaws. The simulations were performed with the cluster model calibrated in Section 3.2.2 with $N_1 = 653$, $N_2 = 1306$ and $N_3 = 1960$ flaws. In each simulation, flaws were equally sized. In each of the three cases under study (N_1, N_2 and N_3), we tested three uniform flaw size distributions, by deleting one, two or three elementary balls per flaw. We repeated the nine simulations several times and checked that similar results were obtained. We compared the results obtained with the same number of flaws but different flaw sizes, and we compared the results obtained with the same flaw size but different numbers of flaws. Results are shown in Figure 3.14. We

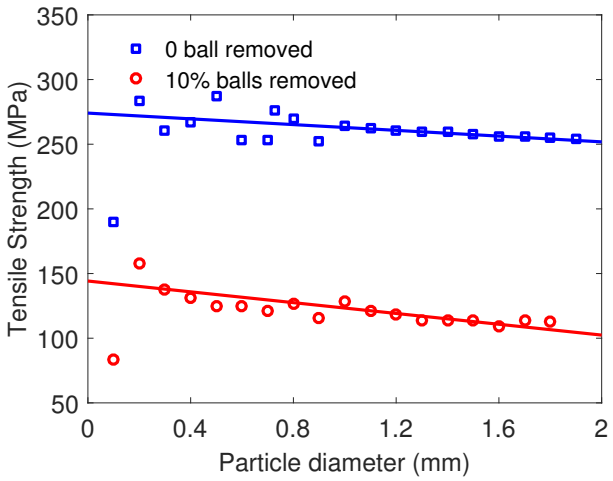

Figure 3.13: Relationship between the strength and the crushable particle size (fixed flaw size).

verify that strength decreases when porosity increases, and we note that particle tensile strength decreases linearly with the flaw size. For the range of porosities and numbers of flaws investigated in this parametric study, it was not possible to simulate crushing for a large range of flaw sizes. We present results obtained for a larger span of flaw sizes in the next subsection.

3.4.3 Effect of the Number of Flaws

In the following, we investigate the strength of particles that contain a variable number of equally sized flaws. The size and DEM parameters of the cluster are those presented in Section 3.2.2. Flaw sizes ranged between $n = 1$ to $n = 100$ times the elementary ball size. We started by generating a random distribution of flaw centroids. Then we deleted elementary balls containing the centroids ("centroid balls"). For $n \leq 10$, we created flaws by deleting $(n - 1)$ balls in contact with each centroid ball. For $n > 10$, we deleted all the elementary balls contained in a spherical control volume around the centroid balls. The size of the control volume was increased until it contained the desired number of elementary balls to be deleted. For the same level of porosity, the distribution of flaws was more uniform for smaller (and more numerous) flaws than for larger flaws. This explains why

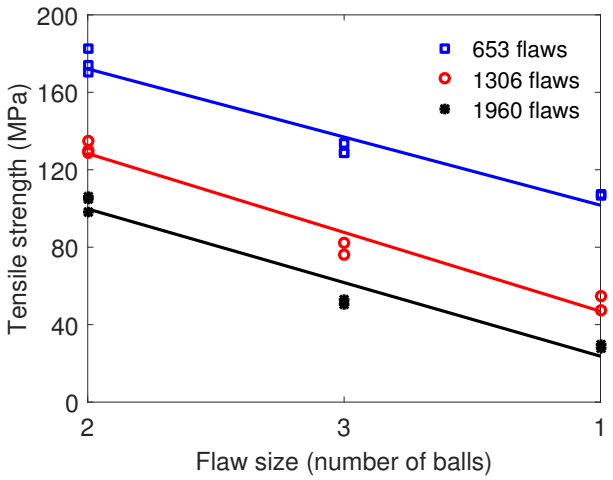

Figure 3.14: Effect of flaw size on particle tensile strength. Flaws were created by deleting elementary balls that formed the cluster. Three flaw sizes were studied, by deleting sets of three balls in contact, two balls in contact, or balls initially not in contact.

simulations were more difficult to reproduce when $n > 10$ than when $n \leq 10$. The results are presented in Figure 3.15. For each flaw size investigated, a linear relationship was found between the particle tensile strength and the logarithm of the number of flaws. We note that the slope is similar in all the simulations performed with $n \leq 10$. For larger flaws, the strength decreases at a faster rate with the number of flaws present in the cluster.

3.4.4 Effect of Porosity

The previous parametric studies indicate that the size effects noted in particle strength are more likely attributed to the size and number of flaws, rather than to the size of the particle itself. In a crushable particle that contains equally sized flaws, are size effects due to the average flaw size or to the number of flaws? In order to answer this question, we compared the results obtained for clusters of same porosity but different flaw size. Figure 3.16 shows the variations of particle strength with porosity (which was calculated as the percentage of elementary balls deleted to create particle flaws). We note that for a given particle porosity, particle strength decreases when porosity increases and does not vary with the flaw size. Laboratory tests reported in the literature indicate that the strength of a material (of given

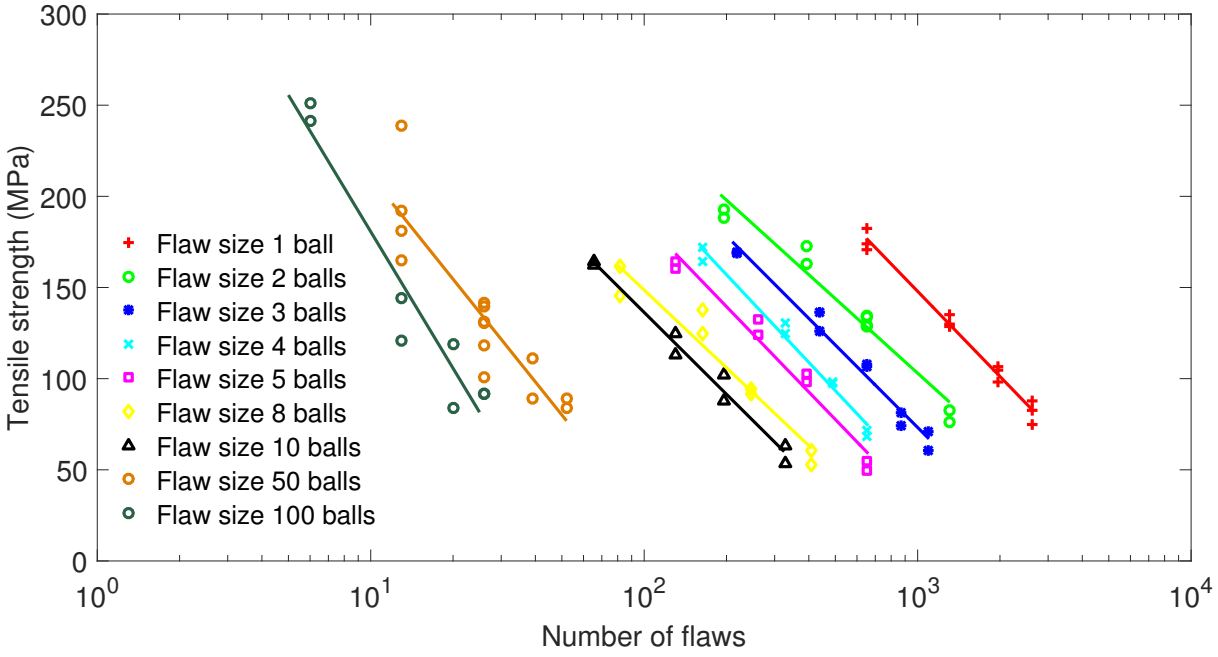

Figure 3.15: Effect of the number of flaws on particle tensile strength. Flaws were created by deleting elementary balls that formed the cluster. Groups of up to 100 balls in contact were deleted to produce flaws of different sizes.

porosity) decreases when the flaw size increases. In DEM simulations, stress redistribution after bond breakage leads to another stable position of equilibrium. Therefore breakage does not propagate from one bond to the neighboring bonds. The total force needed to fragment a particle is the sum of the contact forces needed to break all the elementary bonds inside that particle. More sophisticated models are needed to capture unstable fracture propagation and consequent cluster strength variations in DEM [93]. This being said, our results confirm the strong dependence of particle strength to porosity, already noted in uniaxial compression strength (UCS) tests performed on porous rock samples [104] [105].

3.5 Conclusion

We modeled a crushable sand particle as a quasi-spherical cluster of bonded, hexagonally packed, equally sized, non-breakable balls. With this distinct element model, a series of single-particle uniaxial compression tests were simulated by controlling the velocity of two

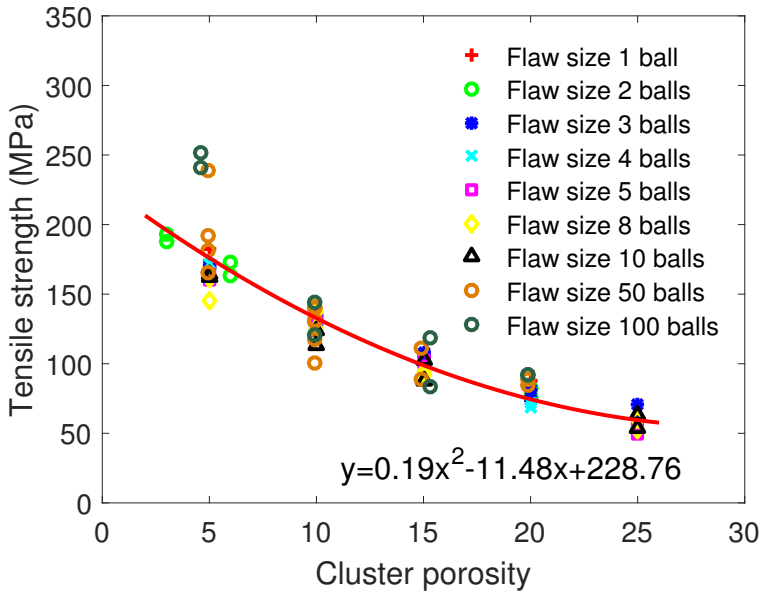

Figure 3.16: Effect of porosity on particle tensile strength.

rigid walls, placed at the top and bottom of the cluster. We calibrated the DEM parameters so as to match the displacement and axial force obtained experimentally at the first particle fragmentation. Then the calibrated cluster model was used to simulate shielding and size effects at the particle scale. In order to study the influence of the coordination number on particle crushing, we modeled the mechanical confinement effect of neighboring particles by placing rigid walls around the cluster. We used symmetric distributions of walls for coordination numbers lower than 60, and both symmetric and random wall distributions for higher coordination numbers. We found that the axial force necessary to trigger the first fragmentation increases linearly with the coordination number. In order to understand why larger particles have lower tensile strength, we studied size effects on the crushing process of clusters with and without internal flaws. At constant flaw size and cluster porosity, we found that the cluster tensile strength did not depend on the cluster size as long as the ratio ball size / cluster size was smaller than 0.014 (i.e. for clusters that contained at least 37,000 elementary balls). We also verified that the tensile strength of a particle of given size decreases when, for a given flaw size (respectively for a given number of flaws), the number

of flaws increases (respectively the flaw size increases). For clusters with a porosity ranging between 0% and 30%, tensile strength only depends on porosity and not on flaw size. The results thus show that particle strength depends: (1) linearly on particle coordination number; (2) quadratically on particle porosity. The numerical methods presented in this chapter will be improved to model the process of fragmentation within an assembly of particles and predict the combined actions of shielding and size effects. Theoretical and DEM modeling of particle crushing will advance the fundamental understanding of energy transfer in particulate media, which can be used to design infrastructure (e.g., ballast), shielding materials (e.g., packaging), food and medical products (e.g., tablets).

CHAPTER 4
IMAGE BASED MICRO-MECHANICAL MODELING OF FRAGMENTATION IN GRANULAR MATERIALS

4.1 Introduction

In DEM, particle breakage can be modeled with the cluster (agglomerate) method or the replacement method. In the former, crushable particles are represented by a cluster of smaller elements that are bonded together. The cluster breaks when stresses in the bonds exceed the corresponding bond strengths. The cluster method was used in Chapter 3, as well as in many other works [14, 69, 22]. In the replacement method, breakage occurs when the stress induced by contacts is larger than the particle strength or when it satisfies a limit condition. The broken particle is then replaced by several smaller fragments.

Both methods have their pros and cons. In the cluster method, micro-cracks that occur in a particle before a major breakage event and can be tracked by the number of broken bonds. The shape of fragments truly depends on the stress distribution in the crushable particle, but the solution depends on the number of elements and bonds considered in the cluster. Precise models are computationally expensive due to the large number of elements represented in each cluster (typically, several tens of thousands of elements per cluster). The replacement method is relatively more effective because the number of elements is equal to the number of soil grains. The replacement method can be used to predict driving forces, breakage modes as well as to study the effect of the coordination number on crushing. The main challenge is to define the breakage model parameters, such as the particle strength, the position and orientation of breakage planes, the number and size of the fragments.

The use of X-ray Computed Tomography (XCT) in experimental studies has allowed

the 3D observation and measurement of the micro-mechanisms leading to particle breakage. Through single-particle compression tests, Zhao and collaborators observed the strong influence of particle morphology on particle stress distribution [106]. They found that particles with small radii of curvature were prone to extensive fragmentation, due to local stress concentrations at the contact points between the particle and the loading plates. The importance of using 3D images to describe particle morphology has been discussed in [107], showing that 2D and 3D measurements produce important differences in various particle shape parameters. XCT coupled with sophisticated algorithms, such as particle tracking [108], was used to predict and measure the life expectancy of porous granular materials during oedometric compression [109]. 3D images were also used for qualitative comparison of particle crushing with DEM and FEM models [110, 111].

In this chapter, we build a new DEM breakage model, using direct micro-scale observations and measurements from 3D images, to realistically represent the breakage process and capture the resulting macroscopic material properties. To achieve this goal, we first present an experiment conducted by our collaborators at 3SR Laboratory (Grenoble, France), in which uniform dry zeolite specimens were subjected to oedometer compression and imaged with an XCT scanner at different stress levels. We used several image processing algorithms to identify and track intact particles and fragments and get information about the evolution of grading and the types of breakage events. Our observations are reported in Section 4.2. We studied selected breakage events that occur in the oedometer test, by using 3D image analysis and different breakage models in replacement method. We proposed a new robust breakage model (explained in Section 4.4), which can simulate sequential breakage, generate non-spherical fragments and predict appropriate arrangements of fragments. Lastly, we calibrated the parameters and simulated the oedometer test. The results, presented in Section 4.5.2, show good agreement with the experimental results.

4.2 Zeolite oedometer tests and XCT

4.2.1 Experimental methods

In this chapter, we use experimental results from Zeynep Karatza's PhD thesis [80]. Strain-controlled oedometric compression tests were conducted on manufactured zeolite granules and scanned with an XCT at 3SR laboratory in Grenoble, France. The material was chosen due to its highly spherical and rounded shape, which facilitates the modeling of the experimental procedure using the DEM. Each particle had a density of 2.18 g/cm^3 and an estimated crushing strength of 15 N. The intact sample had a mean particle diameter (D_{50}) of 1.36 mm and a very uniform grading (C_u = 1.07). The specimens were created to have the same repeatable dense initial configuration (porosity 40 %). The microstructure properties of the specimens (*i.e.*, particle size, shape and grading), allowed all intact particles to be imaged with the same precision and ensured the highest possible probability of fracturing [112, 113]. Each specimen had a diameter of 15 mm and a target height of 15 mm, which slightly varied among the specimens due to the material filling process. The oedometric cell was made of PEEK (specially designed for this study), chosen for its low x-ray absorption and low friction properties (more details can be found in [80]). The loading direction was ascending and the quasi-static loading was performed with an axial loading rate of 50 μm/min.

Imaging was done with an x-ray scanner using 100 kV of acceleration [described in 114]. The voxel size (*i.e.*, 3D pixel) was 12.3 μm/px and 10.0 μm/px for tests 1 and 2 respectively, which allowed getting images of high resolution. Loading was performed *in-situ* in the scanner under displacement control, setting the strain rate to zero during scanning (*i.e.*, loading stage).

4.2.2 Analysis of particle breakage using XCT

A 3D reconstruction provided full microstructure information in the form of 32-bit floating points. In order to save space and have some inherent normalisation between the scans, the data was degraded to a 16-bit integer format, which offers a 2^{16} dynamic range of grey scale information and is more than the noise of reconstruction. Figure 4.1 shows vertical slices from the reconstructed 16-bit 3D images. In the first loading stages, only primary breakage appears to occur, however after an axial strain of 7.12 %, a number of fragments undergo significant breakage. Additionally, from a careful visual inspection of the images, the majority of breakage events occur close to the moving boundaries, as previously observed in [115].

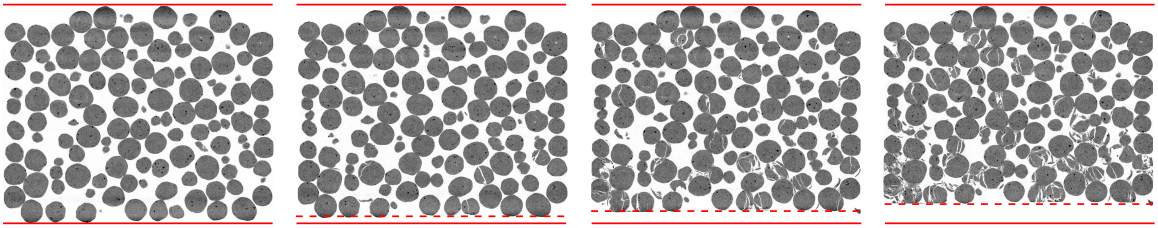

Figure 4.1: Vertical 2D slices from the oedometer test (strains in %) [80]

For the measurement of the volume, size and shape of the particles, the particles must first be detected, therefore the continuous grey scale information must be segmented. A threshold that distinguishes the solid and void phases (*i.e.*, binary image) was set by means of an algorithm that preserves moments [116]. A watershed analysis [117] was used to separate contacting particles, so that each particle could be surrounded by voxels that represent void. As a result, individual particle measurements could be performed.

Zeolite particles have significant intra-porosity, which is filtered after the initial binarisation, to avoid over-segmentation. The internal pores are significantly smaller and more spherical than the inter-particulate pores, which provides a basis to define the criterion in the filtering process. This procedure is described in Figure 4.2.

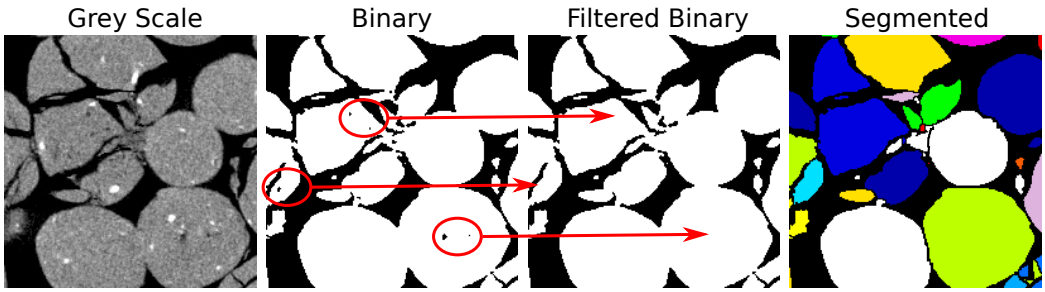

Figure 4.2: Identifying and filtering intra-particle porosity [80]

After each particle (intact granule or fragment) has been identified, we measure the perpendicular maximum and minimum lengths of the particle at 60 different orientations. Then the medium diameter of a prescribed ellipsoid of same volume as the particle is calculated and assigned to each particle and used to get the Particle Size Distribution (PSD) for each loading stage [29].

4.3 Image Based Analysis of Particle Breakage Criteria

The goal of this section is to test the breakage criteria in Section 2.4 based on the breakage events in a set of 3D images taken during an oedometer test.

4.3.1 Test procedure and data acquisition

In the test, zeolite specimens were loaded with confinement, and XCT was performed before loading and at several key loading stages, after some breakage events had occurred [49]. The grains were close to spherical with a D_{50} of 1.36 mm, as shown in Fig 4.3. The mechanical response was found to be the same for three different loading strain rates (25 μm/min, 50 μm/min and 100 μm/min). The mean particle diameter contained around 120 pixels, which provided enough details to identify contacts and breakage fragments. Then the anisotropic diffusion method, which is a partial differential equation based filtering technique, was used to reduce the noise and hence maximize the signal to noise ratio. After filtering the image, watershed segmentation was used to identify grains and fragments

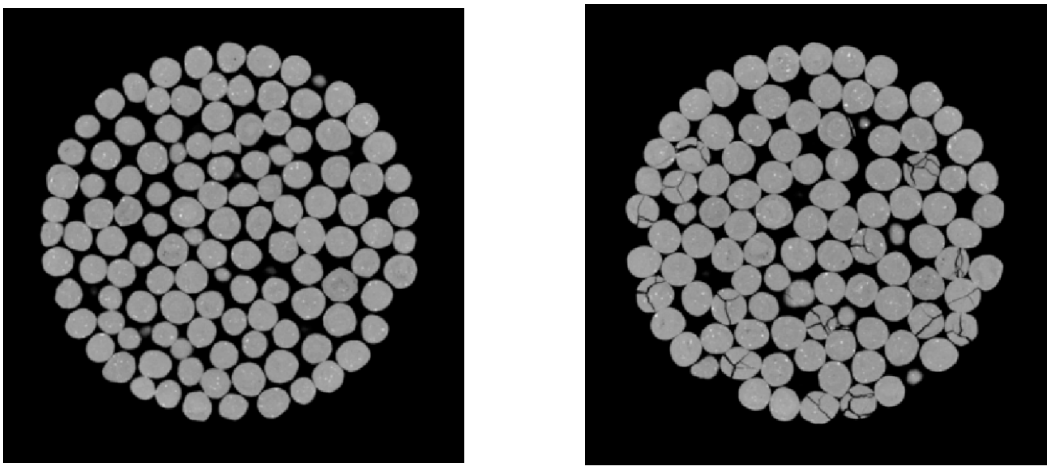

(a) (b)

Figure 4.3: Slice of an XCT scan of a zeolite specimen (a) before compression; (b) after compression

[118]. Any selected grains A and B have boundary point sets $A_{boundary}$ and $B_{boundary}$. When the euclidian distance between two points of two different sets is smaller than 1, these two points are considered in contact.

Breakage events and broken particles were identified, selected and numbered in the image. We focused on splitting breakage, for which breakage criteria listed in Section 2.4 can be applied. Therefore we visually chose particles that had a major breakage plane that went through the particle centroid, as shown in Figure 4.4. For each selected broken particle, we used the anisotropic diffusion method and the watershed segmentation technique to determine the positions and areas of the contacts before breakage, the position of a particle relative to its neighbors and the volume of neighboring particles. We also identified the points on the breakage plane. Then we used the least square method to fit the points on the breakage surface on a plane. Figure 4.5 shows the front and top views of the surface, the contact points, and the direction and location of the breakage plane of one of the broken grains.

Contacts are assumed to be circular surfaces. According to the Hertzian contact theory

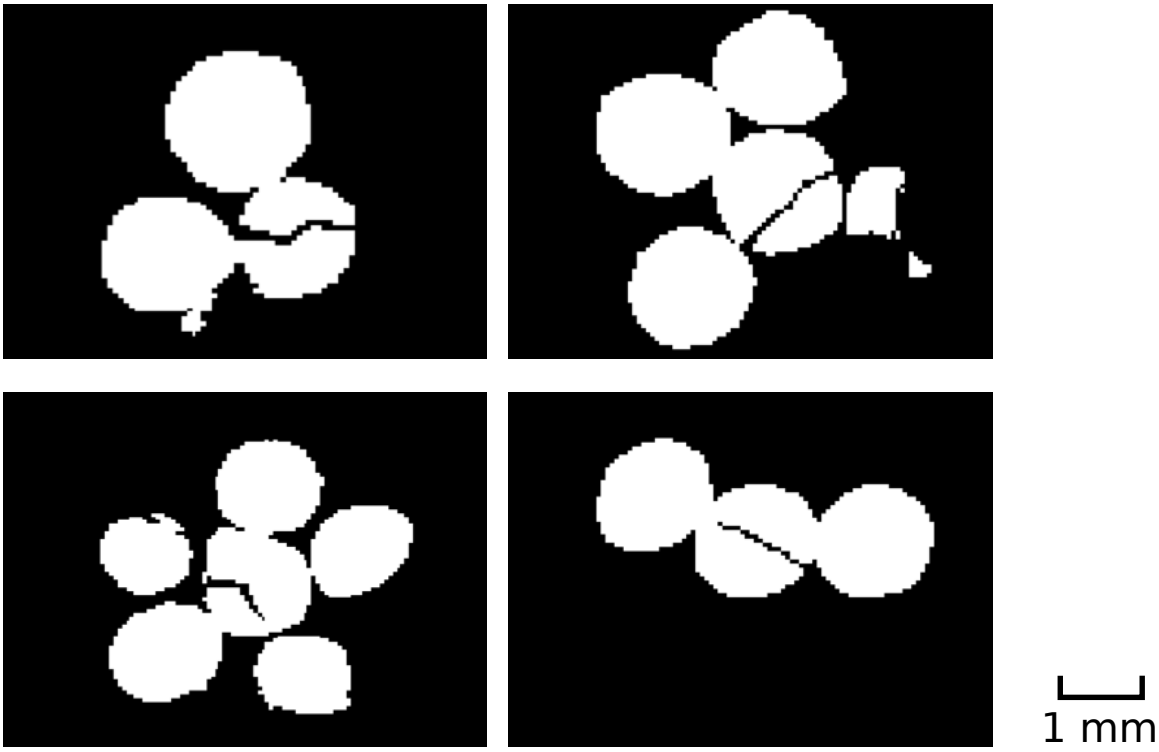

Figure 4.4: Splitting breakage events selected from the oedometer test.

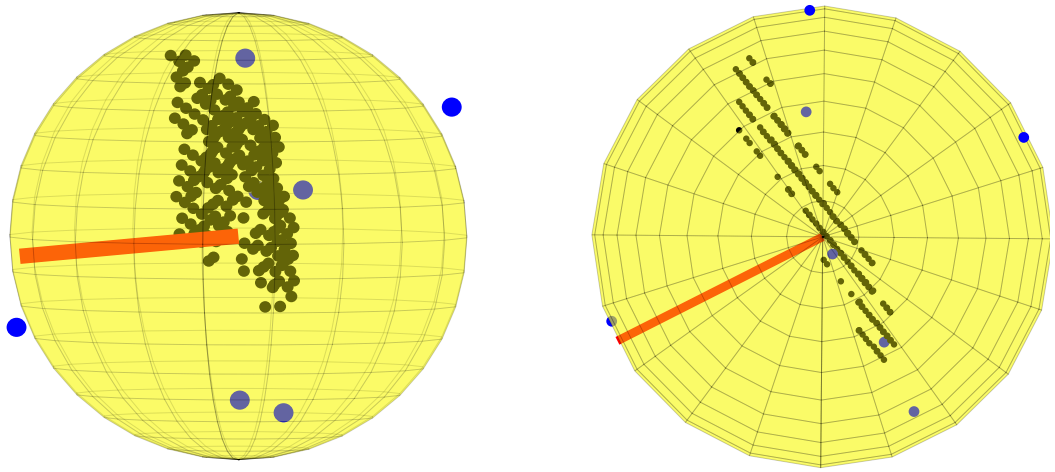

(a) (b)

Figure 4.5: Data obtained on a broken grain 703 from image analysis (a) Front view and (b) Top view: blue points represent contact positions; black points are on the breakage plane; the red line is the direction normal to the breakage plane; the yellow surface is the grain surface.

[92], the effective contact radius R of two spheres in contact is given by

$$\frac{1}{R} = \frac{1}{R_1} + \frac{1}{R_2} \tag{4.1}$$

where R_1 and R_2 are the radii of the two particles in contact. The relation between the contact radius a, the depth of indentation d and the effective radius R can be expressed by $a = \sqrt{Rd}$. Then the contact force F has the expression

$$F = \frac{4}{3} E^* R^{1/2} d^{3/2}. \tag{4.2}$$

where E^* is a function of the Young's modulus and Possion's ratio of the material.

4.3.2 DEM Breakage Criterion Tests

Based on the contact force, contact position, breakage plane, size and position of a particle obtained by image analysis (Section 4.3.1), we calculated the stress tensor using Equation 2.16 and predicted the breakage plane according to five breakage criteria. The following assumptions are made:

- All particles are made of the same material and thus have the same mechanical properties, such as E and μ.
- The Hertzian contact theory applies.
- The contact area calculated from image analysis at the timestep before breakage is equal to that at the time of particle breakage.
- Breakage is a sequence of events that include a major splitting followed by several smaller breakage events; the major splitting event is controlled by the breakage criterion.

We compared breakage plane predictions obtained with the 5 following methods:

- M1: Maximum tensile stress method.
- M2: Maximum contact force method.
- M3: Force chain method.
- M4: Three largest contact forces method.
- M5: Weighted distance method.

We already presented methods M1 and M2 in Section 2.4. In the force chain method (M3), we assume that the breakage is caused by a pair of co-linear or nearly co-linear forces that compress the particle diametrically. Therefore, the breakage process is similar to that in a single particle crushing test. The three largest contact forces method (M4) is appropriate for cases when the breakage plane does not pass through the centroid of the particle, mainly when the breakage plane contains the three largest contact forces. In the weighted distance method (M5), the breakage plane is fitted between contact points, whose weights are calculated by $F^{(c)} / \sum_{N_c} F_i^{(c)}$. The largest contact force is in, or close to, the fitted breakage plane and smaller confining forces are approximately normal to the fitted breakage plane.

We used methods M1-M5 to simulate the oedometer tests and we compared the direction normal to the predicted breakage plane to the direction normal to the breakage plane observed in the experiments. If the angle between the predicted and observed normal directions is close to 0° or $180\circ$, this means that the model predictions are in good agreement with the experimental data. Results of ten grains, presented in Table 4.1, show that none of the five methods is satisfactory.

The inconsistency between experimental and simulation results comes from two aspects. On the on hand, predicting the breakage plane based on contact forces and contact positions is very complex, because contact forces and directions need to be identified at the time of the breakage event (rather than from post-breakage images). The broken grains

Table 4.1: Angle between the normal to the breakage plane observed in the experiments and the normal of the breakage plane predicted by the models

Method	703	803	885	937	939	964	1065	1066	1134	1116
M1	97.24	65.65	53.92	73.51	100.40	52.9	154.55	92.65	75.12	102.5
M2	97.25	112.62	55.92	106.34	79.48	126.39	26.11	98.15	104.46	77.77
M3	68.41	176.47	56.66	164.79	94.82	167.7	99.92	53.93	71.82	80.25
M4	176.46	140.65	89.3	176.25	168.31	74.95	78.07	53.76	101.88	56.60
M5	14.41	139.94	116.93	39.17	11.04	58.08	162.66	57.8	78.12	110.57

shown in Figure 4.3 and Figure 4.6 exhibit curved breakage surfaces (rather than planes), and undergo several generations of breakage after a major splitting – a phenomenon that was not considered in previous models. On the other hand, the location and orientation of breakage plane in some current models are oversimplified. Breakage planes in M1 to M3 are located thanks to the average stress tensor, regardless of the locations and orientations of the maximum contact forces.

In the experiment analysed in this study, only two grains underwent a major splitting without secondary breakage. Contrary to what is proposed in all current existing replacement models listed in Fig. 2.12, no fragment lies on the breakage plane. Current replacement models are partially inspired by the Brazilian test for rock materials, in which a wedge-shaped fragment may appear at the loading point. However, such phenomenon never occurs in the broken grains studied in the present experiment.

4.4 A Hybrid Replacement Model of Particle Breakage

To overcome the shortcomings of the breakage models discussed in Section 2.4.2 and 4.3.2, we propose a new replacement method that: (1) contains angular fragments made of bonded spherical particles; (2) considers multiple generations of breakage (including both grain breakage and bond breakage); and (3) does not generate fragments on the failure plane. As discussed in Section 2.4.2, we used the maximum contact force as the breakage criterion

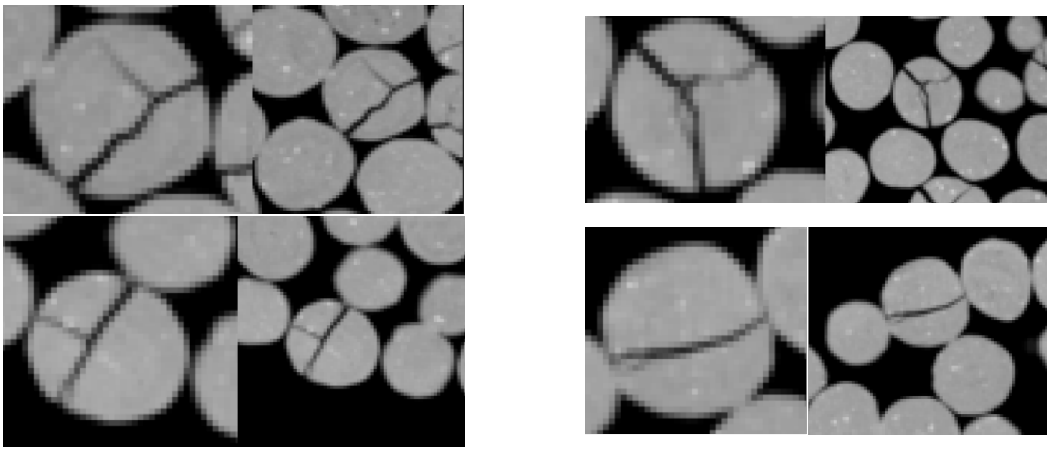

Figure 4.6: Breaking grains and their breakage plane in the oedometer test

in our replacement model. During the simulation, the maximum contact force (F_{max}) of each particle is monitored. When the stress defined as $\sigma_{F_{max}} = F_{max}/d^2$ exceeds the grain strength, the particle is then defined as being broken.

The next step is to replace the broken particle with smaller fragments. We focus on breakage mechanisms where a major splitting event occurs first, during which the particle is separated into two fragments along a plane that contains the contact points with the largest contact forces. During the splitting event, the elastic energy stored in the breaking particle is released and partially turns into fragment kinetic energy. The fragments move in the least confined direction, the largest contact forces (contained in the splitting plane) decrease, and smaller contact forces (confining forces) increase. This latter phenomenon leads to secondary breakage in the fragments, as shown in Figure 4.7. The rearrangement of fragments ultimately transforms kinetic energy into heat and another state of equilibrium is reached. This micro-mechanism of particle breakage is validated from the observation that most broken particles undergo a primary axial splitting and that secondary failure occurs in the fragments.

To model the primary splitting event, we propose to replace the crushable particle by two fragments modelled by clusters of 17 bonded rigid spherical elements (1 central sphere surrounded by 16 smaller spheres of two different sizes) as shown in Figure 4.8. The 16

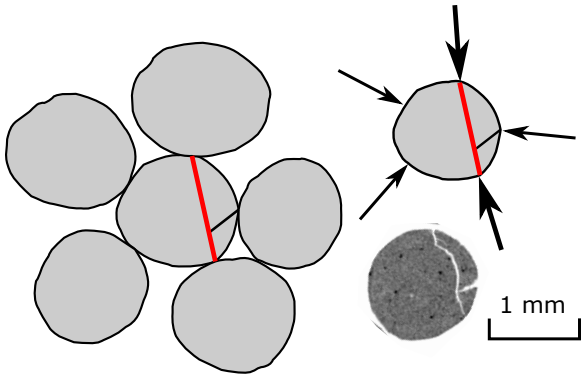

Figure 4.7: Sketch of the sequential breakage mechanism in a zeolite particle (thicker arrows indicate larger contact forces)

smaller spheres are tangent to the sphere that formed the mother particle. Spheres in the same fragment are connected together with parallel bonds, which are joints that transmit forces and moments [119]. We use the bond breakage as a criterion to model secondary breakage. It is important to arrange the spheres in appropriate positions so that the replacement process can match the breakage mechanism to its maximum extent. The arrangement is determined by the breakage plane. In a 2D simulation, σ_3 is zero according to Equation 2.16, thus the breakage occurs along a line that passes through the centre of the mother particle and is coaxial with the maximum principal stress or maximum contact force [17, 76]. In 3D we need two vectors to define the plane direction. If these vectors are defined as the two largest principal directions $\bar{n}_1$ and $\bar{n}_2$ (e.g., [72, 17]), the maximum contact force is not guaranteed to be on the splitting plane. To overcome this limitation, Ciantia rotated the replacement configuration twice so that the vertical axis in the configuration becomes parallel to the direction of contact force [71, 120, 19]. However, he did not provide any physical or mechanical explanation for this rotation. When a particle breaks, fracture propagates in the direction perpendicular to the minimum principal stress direction. In addition, according to our experiments, the breakage planes of broken particles does pass through the contact points. Therefore, in our simulations, we assume that the breakage plane passes through the contact with maximum contact force and that it is perpendicular to the plane

that contains the directions of σ_3 and of the maximum normal contact force.

Additionally, we need to set the smallest particle size allowed to break, to avoid high computational cost. Theoretically, the isolated spherical grains can always break when the breakage criterion is met. However, the large gap between the relative mass of the particles will greatly decrease computational time because the critical time step in DEM is calculated as $t_{crit} = \sqrt{m/k}$, where m is the mass of the smallest grain and k is its stiffness. We set the smallest breakable particle size to be 0.2 mm, which is the smallest size that can be identified in the XCT. Consequently particles below this size threshold do not break in our simulations. This size threshold allows us to have four generations of breakage, as shown in Figure 4.8. The calibration of the new breakage model is discussed in the following section.

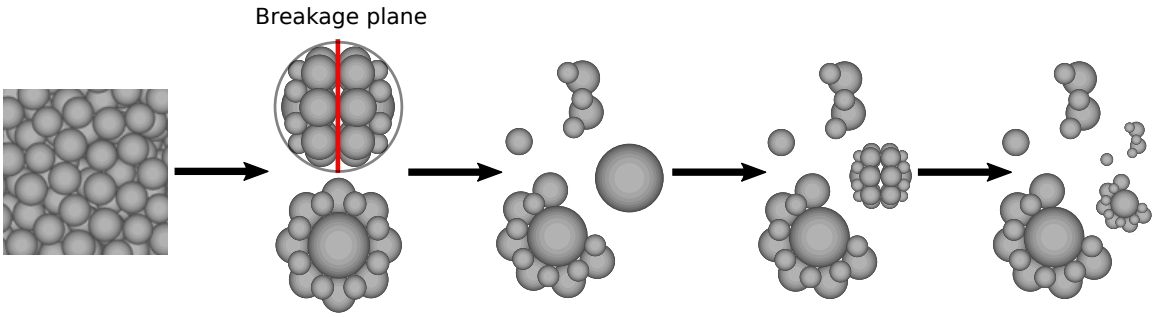

Figure 4.8: Schematic of multiple generations of breakage modelled with the new DEM hybrid replacement method

4.5 DEM simulation of oedometer test

4.5.1 Model construction and calibration

We modelled the oedometer compression test of zeolite granules using the hybrid replacement model proposed in Section 4.4. The parameters in the model are the particles' shear modulus (G) and Poisson ratio (ν), the strength of particles of average size d_0 (σ_{t0}), the Weibull modulus (m), the normal and shear bond strengths ($\bar{\sigma}_n$ and $\bar{\sigma}_t$), the parallel bond normal and shear stiffnesses ($\bar{k}^n$ and $\bar{k}^s$) and the parallel bond radius multiplier λ.

The contact between unbonded spherical particles is governed by the Hertzian contact model, in which the behaviour is solely defined by the shear modulus (G) and Poisson ratio (ν). They are chosen to match the properties of zeolite. We assume that splitting is caused by tensile failure and the relationship between tensile strength and maximum contact force is characterized by $\sigma_{F_{max}} = F_{max}/d^2$, where d is the diameter of the particle [11, 85]. In a single particle compression test, the grain strength is the particle's tensile strength. However, in a granular assembly, each grain is shielded by its neighbours, leading to a redistribution of the stress induced by contact forces that results in quasi-hydrostatic stress and reduced tensile stress. In both experiments and simulations, it is reported that the force necessary to break a particle within a granular assembly is several times higher than that necessary to break an unconfined particle [41, 13]. In our simulations, we set the particle tensile strength to σ_{t0}, to 12 MPa, which is close to four times the tensile strength found from single particle crushing tests. A size effect is however noticed in strength tests performed on a number of different materials [41, 82, 43, 121], indicating that materials with larger sized particles usually have lower strengths. We account for the size effect by using a Weibull distribution of tensile strength, where the survival probability of a particle of size d is given by $P(d) = exp[-(d/d_0)^3(\sigma_{F_{max}}/\sigma_{t0})^m]$ [87, 122], and we set the Weibull modulus to 3.0, which is a reasonable estimation, according to the test results summarized in [122]. The parallel bonds' normal and shear strengths are set equal to 3.3 MPa, which is the tensile strength found from single particle crushing tests. The parallel bonds' normal and shear stiffnesses are calculated using the equations $\bar{k}^n = E/(R^{(A)} + R^{(B)})$ and $\bar{k}^s = G/(R^{(A)} + R^{(B)})$, as proposed by [99]; where $R^{(A)}$ and $R^{(B)}$ are the radii of the bonded ball and E the Young's modulus calculated from G and ν. The frictional coefficient, which is known to not greatly influence DEM results [123], is set to 0.5; this is a common choice in DEM simulation [124, 99]. The parallel bonds' radius multiplier λ is used to set the bond radius and area; the larger it is the stronger the bond is (*i.e.*, a larger force is required to break the bond). A summary of the parameters used in the simulation is shown in Table

4.2.

Table 4.2: Parameters used in the DEM simulation

Shear modulus (G)	GPa	2.2
Possion's ratio (ν)	-	0.25
Density of sphere (ρ)	kg/m^3	2180
Material tensile strength (σ_{t0})	MPa	12.0
Weibull modulus (m)	-	3.0
Normal and shear bond strength ($\bar{\sigma}_n$ and $\bar{\sigma}_t$)	N/m^3	3.3
Frictional coefficient of sphere (μ)	-	0.5
Parallel bond radius multiplier (λ)	-	1.25

In order to reproduce the conditions of the experiment, the diameter and height of the sample are respectively set to 15 mm and 12.25 mm (same as in the experimental set-up). Particles are initially randomly generated in a cylinder that is 15 mm in diameter and 30 mm in height, and then subjected to free falling movement to the bottom of the cylinder. In order to generate particles following the same initial grading as in the experiment, we fit the probability density of particle sizes found experimentally to a normal distribution and we use it to generate particles in the DEM sample. The probability density functions are shown in Figure 4.9. The porosity of the sample is between 44 % and 45 %, like in the physical test. The loading speed is set to 0.1 m/s, which allows simulating quasi-static conditions [16, 41, 99]. During loading, the breakage criterion is checked every ten steps and the compressive strain of the assembly, the contact forces, the number of broken grains and the location of the particles are recorded.

4.5.2 Simulation results

The stress – strain curves for both the experiment and the simulation responses are shown in Figure 4.10, in which we can see that simulation results follow the same trend as the experimental ones. The stress – strain curve clearly shows a yielding region at around 2 MPa after the initial compaction. Before yielding, the curve is smooth with just a few

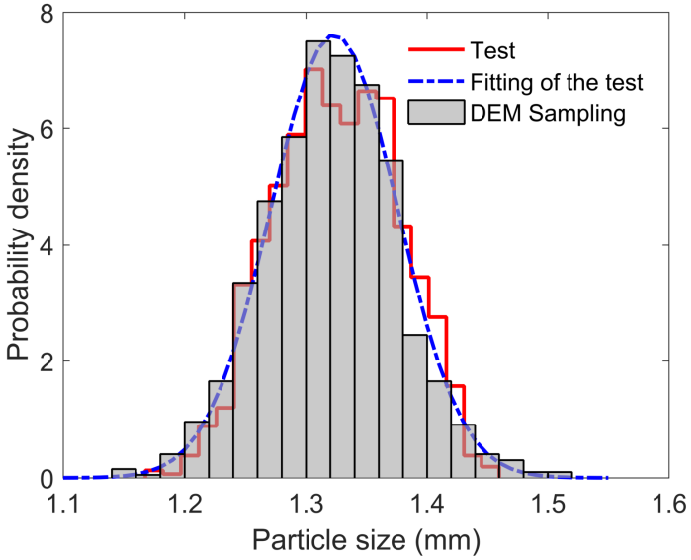

Figure 4.9: Probability density functions of DEM and experimental initial particle configurations (before oedometric compression)

fluctuations, indicating grain breakage and stress release due to particle rearrangement. After yielding, the curve shows important fluctuations caused by extensive particle and bond breakage. The rapid increase in the number of broken particles and bonds after yielding is more evident in Figure 4.11. Before yielding there are 20 broken balls and 300 broken bonds, yet the two values rapidly increase to respectively 280 and 10,000 as the compressive stress reaches 4 MPa. Figure 5.7 shows the sample before and after compression (note that in order to have a better view of the fragments, intact particles are set invisible in Figure 5.7(b)). We can also see that breakage is more likely to occur near the loading platens, which is in agreement with experimental observations.

We now focus on the evolution of the PSD during compression. Figure 4.13 compares the numerical and experimental PSDs at axial strains of 0.00 %, 4.40 %, 7,12 %, 11.28 % and 15.48 %: DEM results are in agreement with physical measures. As the strain increases, particles continue to break, resulting in the increase of the number of fines. It is noticeable that the PSD curves in the DEM simulation are slightly below those in the experiment for the size range from 1.1 mm to 1.2 mm. We attribute this difference to the

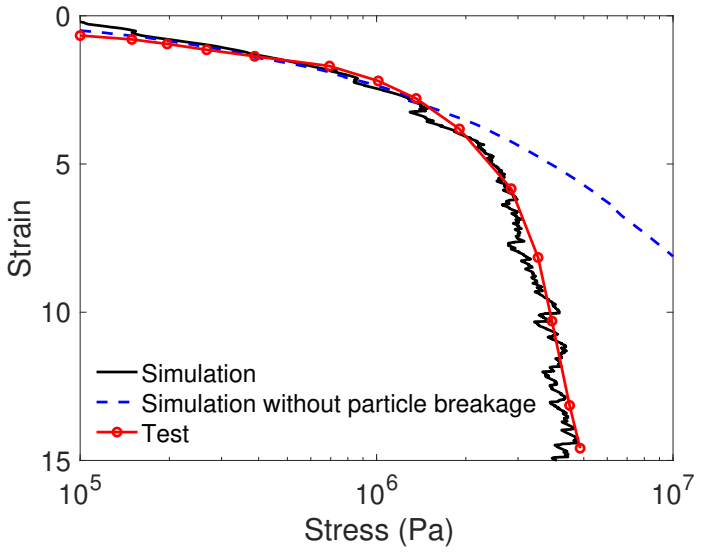

Figure 4.10: Comparison of DEM and experimental results of an oedometric compression test performed on zeolite

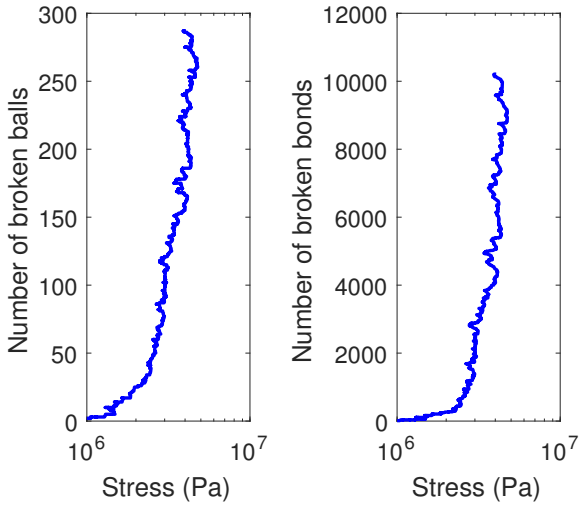

Figure 4.11: Number of broken particles and broken bonds at the end of the simulation

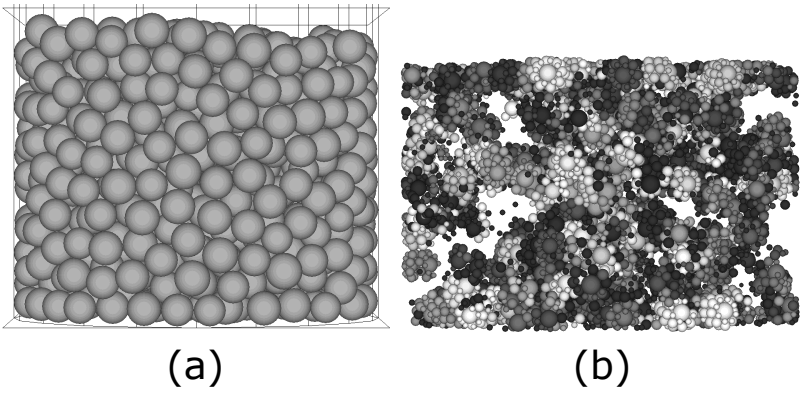

Figure 4.12: DEM model before compression (a) and broken particles after compression (b) [note that intact particles are set invisible in (b)]

surface chipping that occurs during the experiment, which cannot be captured in this model. In fact, at the end of simulation (i.e. for an axial strain of 15.48 %), we find that 35 % of the intact particles break compared to nearly 70 % in the experiment. That said, one has to keep in mind that most breakage models aim to only reproduce the macroscopic stress/strain curve and the PSD [49, 34, 36], which are both in agreement with experimental measures in our proposed model. We conclude that the hybrid replacement model of breakage is representative. Chipping will be studied in future work.

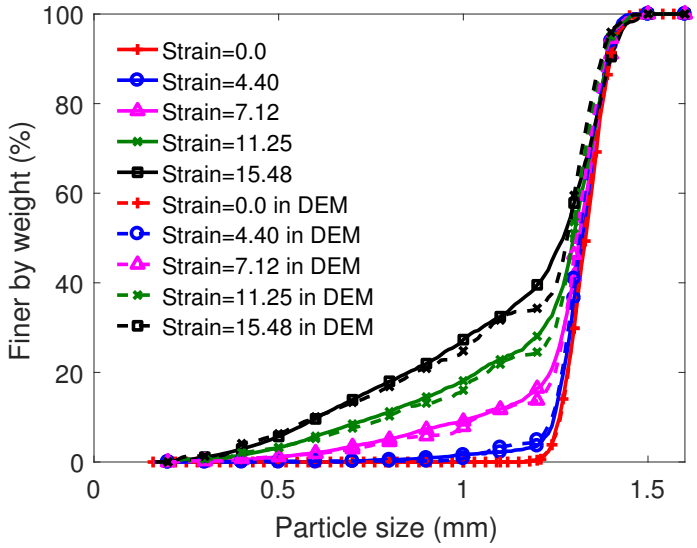

Figure 4.13: Evolution of the PSD in the simulation and in the experiments

An important feature of our proposed new model is the generation of non-spherical fragments. We use the Flatness Ratio (FR) and the Aspect Ratio (AR) to characterize particles' shapes; these two parameters are given by $FR = D_{min}/D_{med}$ and $AR = D_{max}/D_{min}$, where D_{min}, D_{med}, and D_{max} are respectively the smallest, medium and largest dimensions of the minimum circumscribed cube. The distributions of FR and AR calculated at the end of the simulations are shown in Figures 4.14 and 4.15, respectively. Note that initially, both the FR and AR are equal to 1.0, because granules are initially quasi-spherical. At the end of the experiments (respectively, simulations), 81 % of the particles (respectively, 78 % of the particles) have an FR between 0.9 and 1.0 and 71 % of the particles (respectively, of 80 % the particles) have an AR in the range of 1.0 to 2.0. The match between experimental and numerical results is thus satisfactory for quasi-spherical fragments, which constitute about three-quarters of the particles in the final stage of the oedometer test. Figure 4.14 shows that the number of particles with an FR between 0.8 and 0.9 (respectively, between 0.4 and 0.8) is lower (respectively, higher) in the simulation than in the experiment. We think that the high number of particles with an FR between 0.8 and 0.9 in the experiment is due to chipping, a process by which mother particles that have not yet experience primary breakage by splitting are eroded. Eroded mother particles are considered non-spherical in the image analysis but they are considered spherical in our model. Further more, the high number of particles with an FR between 0.4 and 0.8 in the simulations is attributed to the type of primary breakage in our model, which produces fragments of FR around 0.5, separated by a breakage plane. Figure 4.15 shows that number of particles with an AR between 2.0 and 3.0 (respectively, over 3.0) is lower than (respectively, negligible in front of) the experimental values. This difference is also attributed to chipping, which produces a large number of angular fragments (chips) through a process that is not captured (yet) by the proposed model. To support his interpretation, note that in the experiments, the smallest 10 % particles (which stem in part from chipping) have, in average, an AR that is 14 % higher than the 90 % larger particles.

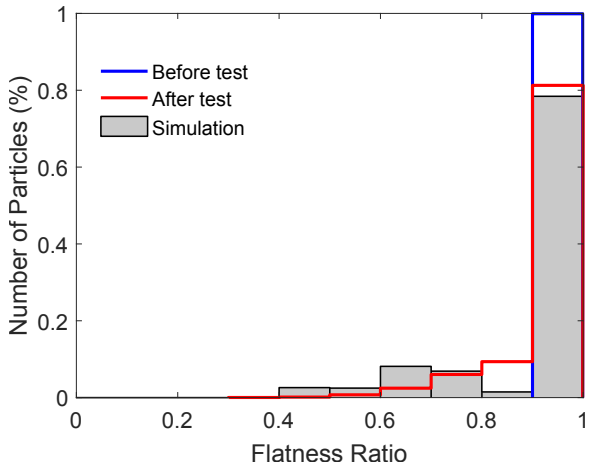

Figure 4.14: Flatness ratios of the particles before and after the test.

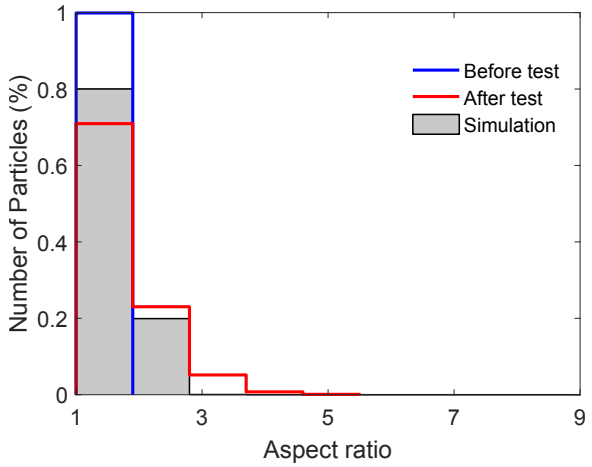

Figure 4.15: Aspect ratios of the particles before and after the test.

4.6 Conclusions

Understanding the micro-mechanisms leading to particle crushing is important because fragmentation affects the bulk mechanical behaviour of granular materials. The DEM is often used to study particle breakage. An appropriate breakage model is crucial in DEM because it defines the breakage criterion and the configuration of the fragments. In this chapter, we proposed a new, hybrid DEM replacement method. We analysed the experimental results and the 3D images at both sample and grain scales with emphasis given on particle breakage. From the quantitative 3D experimental analysis, we validated and calibrated the DEM results. In summary, here are the main conclusions:

1. The DEM model includes both tensile splitting and bond breakage, combining the two most commonly used DEM models in the literature: particle replacement (used for primary splitting breakage) and clustering (used for breakage of fragments). The model allows simulating several cycles of splitting breakage and cluster fragment breakage. Sequential breakage stops when a fragment reaches a critical size, equal to the resolution of the XCT images.

2. Thanks to the clusters introduced in the model, angular fragments can be produced during the simulation, depicting a realistic evolution of particle grading during crushing.

3. An important improvement upon previously published models is that during the tensile splitting, the breakage plane is defined by the contact carrying the maximum normal force and direction of minimum principal stress, instead of assuming that the breakage plane contains the two maximum contact force vectors.

4. The 3D images confirm that multiple generations of breakage occur during the oedometric compression of zeolite and, by using rigorous algorithms, we could accurately

quantify the evolution of the PSD. The PSD obtained with the new DEM hybrid replacement model exhibits an impressive matching.

5. The bulk response of the oedometric compression was also compared to the DEM results. Using the new breakage model results in good agreement with the experimental stress – strain relationship.

This research is expected to provide insights to improve DEM breakage models and to allow developing toolboxes for further analysis of particle breakage mechanisms.

CHAPTER 5
ENERGY DISTRIBUTION DURING THE QUASI-STATIC CONFINED COMMINUTION OF GRANULAR MATERIALS

5.1 Introduction

During particle crushing, the total input energy of the granular assembly (δW) is stored in the form of elastic energy in the grains, and dissipated by breakage, friction and grain redistribution, i.e., the production of kinetic energy of moving fragments [20]. A good understanding of how the energy dissipates during confined comminution is necessary to formulate sound constitutive models for granular materials. For instance, McDowell and Bolton were able to explain compressibility changes by relating particle crushing to the variations of void ratio, and by introducing the breakage energy in the Cam clay model [39]. Based on thermodynamic principles, Collin introduced non-associative flow rules to model friction-induced plasticity in granular materials [125]. Recently, the breakage mechanics theory was formulated to predict the thermodynamic response of crushable granular materials within continuum mechanics [57, 36]. In the theory of breakage mechanics, the evolution of the particle size distribution is used to predict the amount of energy dissipated by breakage, which is fully coupled to the redistribution energy. Within this framework, further developments were proposed to analyze creep, permeability, cementation and the brittle-ductile transition of granular materials [58, 10, 59, 60].

To better understand energy distribution during the process, let us consider an assembly of granular material subjected to an oedometer compression test. Under low stress, the solid skeleton sustains the load, which leads to an increase in stored elastic energy. As the stress increases, some friction will occur at some contacts. Since in this stage the coordination number of each particle is low (compared to that in the subsequently crushed material),

particles are more likely to split in mode I. As the particles continue to break, both of the coordination number and the breakage energy increase. For an increased coordination number, shileding effects induce breakage hardening. As the Particle Size Distribution (PSD) approaches the ultimate PSD, the probability to break a grain decreases, and the energy dissipated by breakage becomes negligible in front of the elastic energy stored at the contacts and the energy dissipated by friction.

How to calculate the relative fraction of the energy components dissipated during comminution has been studied for decades both at the grain and at the sample scales, with analytical, numerical and experimental methods. Bolton *et al.* [21] used the Discrete Element Method (DEM) to analyze the energy distribution during a crushing test performed on a single particle, modeled as an assembly of bonded spheres. The breakage energy was calculated as the total elastic energy stored at the contacts before bonds failed. The energy dissipated by breakage was estimated to be about 10% of the total input energy. The remainder energy was converted into kinetic energy of fragments and then lost by friction and damping. By contrast, in another DEM simulation of particle crushing, the breakage energy was found to be 30% of the total input energy [22]. This difference may come from the properties of the contact bond model, which is difficult to calibrate, and yet largely influences the magnitude of the breakage energy. Recently, X-ray micro-tomography was used to measure the area of new material surfaces created during a single particle crushing test [126]. Zhao *et al.* showed that as breakage proceeds, the extent of material surfaces increases, therefore the number of potential areas of contact increases, and the proportion of energy dissipated by friction exceeds the energy dissipated by breakage. At the macroscale, Rusell *et al.* used simplified models to calculate the ratio between the redistribution energy and the breakage energy, which turned out to be stress independent, but dimension dependent: the ratio was 5 to 20 in 1D, 2 in 2D, and 1 in 3D [20, 10]. The 3D DEM simulation of a triaxial shear test on crushable soil showed that particle breakage contributed to a small amount to the total energy dissipated, but promoted energy dissipation by inter-

particle friction dissipation [68]. Energy distribution was stress dependent, which is in agreement with the results published in [23]. In general, recent results show that energy is mostly dissipated by particle redistribution and inter-granular friction. But there is still no consensus on the relative fraction of the different components of energy dissipated.

In this chapter, we first introduce a method to capture the brittle-to-ductile transition within the framework of breakage mechanics. The sensitivity of the breakage index B_r and the breakage-plasticity coupling angle ω is analyzed. Secondly, we present a novel method to calculate the distribution of energy in a granular sample subjected to quasi-static confined comminution. We used results of uniaxial compression tests performed on cylindrical samples of ground shale and sands under both low compressive stress (0.4MPa to 2.1MPa, [23]) and high compressive stress (up to 92MPa, [127]). The energy decomposition methods are reviewed and the results obtained from the new method is discussed.

5.2 Brittle-ductile transition in assemblies of breakable particles

5.2.1 Theoretical Formulation

Breakage mechanics allows capturing the macroscopic response of a granular assembly subject to particle breakage the evolution of the PSD [36]. The main assumptions of this theory are the following [128]:

- The elastic strain energy stored in the grains is linearly proportional to their surface area.
- The ultimate particle size distribution(PSD) is fractal
- The PSD evolves linearly between the initial PSD and the fractal PSD; the coefficient that quantifies the distance from the current to the initial PSD is the breakage index, defined as the ratio between the total breakage and the breakage potential as shown in Equation 2.5 and 2.6.
- The dissipation due to breakage can be expressed as the loss of residual breakage energy

potential.

The energy balance equation of a granular assembly subject to compression can be expressed as:

$$\delta W = \delta\Psi + \delta\Phi \tag{5.1}$$

where δW is the external work input on the boundaries ($\delta W = \sigma : \delta e$); Ψ and $\delta\Psi$ is the Helmholtz free energy and its increment; $\delta\Phi$ is the energy dissipation.

With the assumption that the energy stored in the grains is proportional to their surface area, the Helmholtz free energy is a function of the stored elastic energy $\psi_r(e_v^e)$, the relative breakage index B_r and the parameter ϑ, which ranges from 0 to 1 and defines the distance from the initial to ultimate grain size distribution. The total dissipation is expressed as the sum of plastic energy and breakage energy. After applying the Legendre transformation, a general yield surface is obtained as follows:

$$y \equiv \frac{\sigma : \sigma}{[\partial\delta\Phi_P^\star/\partial\delta e_p] : [\partial\delta\Phi_P^\star/\partial\delta e_p]} + (\frac{E_B}{\partial\delta\Phi_B^\star/\partial B})^2 - 1 \tag{5.2}$$

where $\delta\Phi_P^\star$ and $\delta\Phi_B^\star$ are respectively the plasticity and breakage dissipations; e_p is the plastic strain tensor; and E_B is the breakage energy. Equation 5.2 indicates that the plasticity and breakage are coupled into a single surface. The coupling parameter is an angle omega, defined as follows:

$$\Phi_P^\star = sin^{-1}(\omega)\Phi_P; \Phi_B^\star = cos^{-1}(\omega)\Phi_B \tag{5.3}$$

The combination of equations 5.2 and 5.3 provides the following expression for the yield surface:

$$y = (sin(\omega)\frac{\psi_r(e_v^e)\vartheta}{\xi(e_v^e)(1-\vartheta B)}p)^2 + (cos(\omega))^2 - G_B(1-B)^{-4} \tag{5.4}$$

Defining:

$$p = \xi(e_v^e)(1-\vartheta B); \xi(e_v^e) = p_r\sqrt{K(1-m)(e_v^e - e_0^e) + 1} \tag{5.5}$$

Equation 5.4 can be reduced to

$$y \equiv y_B = E_B - G_B(1-B)^{-2} \tag{5.6}$$

$$y \equiv y_P = p - \frac{\xi(e_v^e)}{\psi_r(e_v^e)(1-B)^2\vartheta} \tag{5.7}$$

5.2.2 Modeling of the Brittle-ductile Transition in Granular Materials

The coupling angle ω is expected to be linearly related to the particle friction angle, as follows:

$$\omega = \alpha\phi \tag{5.8}$$

where α is a constant ranging from 1.6 to 3.4, and ϕ is the internal frictional angle of the dry granular material. This value is also supposed to be related to the initial porosity (both grains and their representative elementary volume) of the granular assembly: higher porosity would result in larger stress drop following a crushing event [128].

We propose that this angle changes with the breakage parameter B. For a material with a small ω, breakage is the main form of energy dissipation, and a low internal friction force exists at grain contacts. For example, breakage is expected to dominate friction in an assembly of glass beads. However, as the glass beads begin to break, it is inevitable to generate rough surfaces and thus friction and plastic work, which means that the angle ω is not a fixed parameter but rather a function that depends on the microstructure as it evolves during the loading. Moreover, if we accept that the PSD tends to a fractal ultimate PSD upon breakage, then we have to accept that the coupling angle should increase with the breakage index to reflect the breakage hardening due to increased shielding effects.

We propose the following relationship, in which ω can take any value between 0 and π/2:

$$\omega = \frac{\pi}{2}B. \tag{5.9}$$

This assumption is based on the idea that: (1) at the beginning of compression, the average coordination number is low, the probability of grain breakage is high, and the plastic dissipation due to friction is low; (2) as particles break, the average coordination number of particles increases, shielding effects reduce the probability of breakage, and more plastic work is done at the contacts to prevent particle movements. We test our assumption by simulating breakage with fixed coupling angle and variable coupling angle.

Figure 5.1 shows the relationship between the volumetric stain and the mean stress P. The trend of the curve is similar to that in one-dimensional compression test. With the coupling angle changing from 0° to 90° (in different models, and remain constant in each of them), the model varies from elastic-breakage model to an elastic-perfect plastic model. It should be noted that with a fixed ω (except for $\omega = 0^\circ$), a singular point exists between the transition from elastic to plastic/breakage, while for the proposed model with a varying ω, a continuous and differentiable curve is obtained. Figure 5.2 is the plot of the

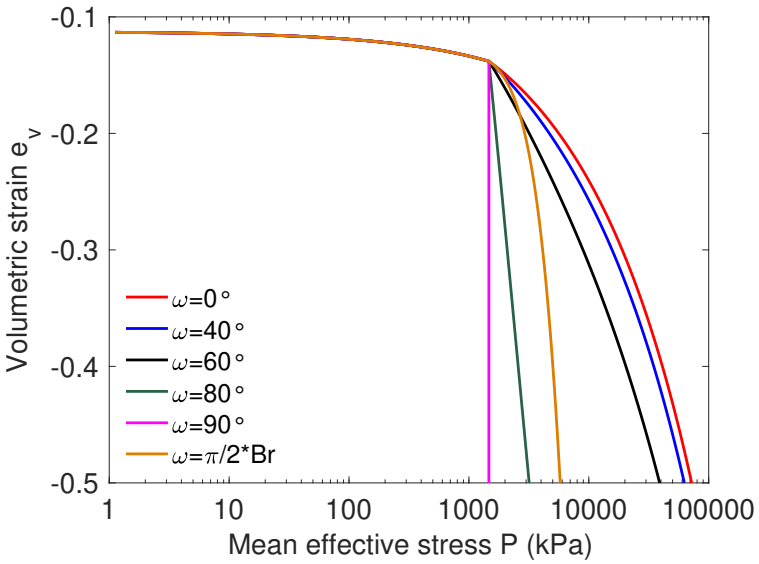

Figure 5.1: The effect of coupling angle ω on stress-strain relationship

relationship between the breakage parameter and the volumetric strain. Results show that, with a variable coupling angle, the breakage parameter is close to that obtained with a fixed, low coupling angle at the beginning of the simulation, and that the breakage parameter

tends towards an asymptote lower than unity at high deformation, due to hardening. Figure 5.3 shows the ratio of plastic work and breakage dissipation. Energy dissipation is zero before breakage initiates. Once the stress state reaches the yield surface, the ratio jumps to a non-zero value which depends on ω and then remains constant. This value, according the Equation 5.4, is given by

$$\delta\Phi_P^\star/\delta\Phi_B^\star = cot(\omega). \tag{5.10}$$

This ratio may range from 0 to $+\infty$ for ω between 0° to 90°. According to our analysis on the brittle-ductile transition, this ratio actually is not a constant during comminution and will greatly increase under high stress. Breakage dissipation becomes less important as the breakage index increases. The relationship between the coupling angle ω and the breakage parameter B is not obvious, and Equation 5.8 is an empirical estimation. That said, results obtained with a varying ω can to some extent explain the experimental results. The maximum ratio at the strain of 0.5 is around 0.8 in Figure 5.3, which is within the range of values obtained at fixed coupling angle. From Figure 5.4 it can be seen that

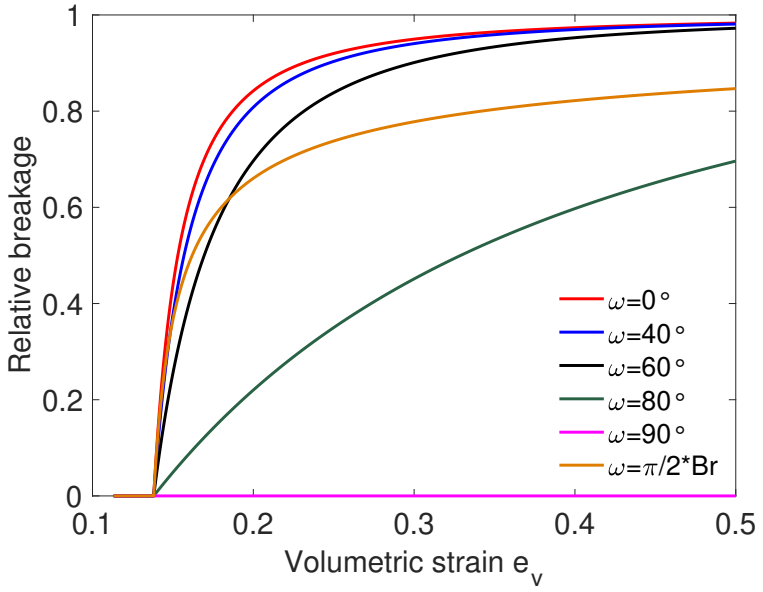

Figure 5.2: The effect of the coupling angle ω on strain-breakage relationship

the proposed model predicts that breakage dissipation dominates plasticity dissipation for

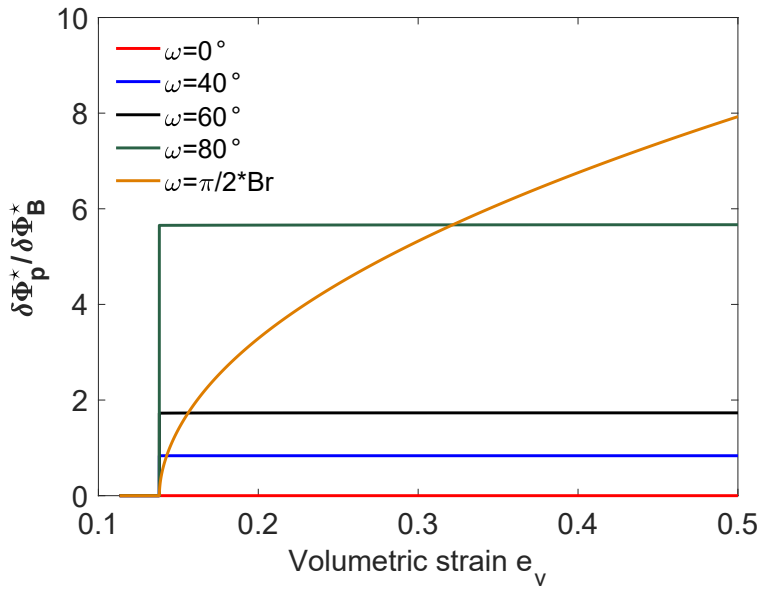

Figure 5.3: The effect of the coupling angle ω on $\delta\Phi_P^\star/\delta\Phi_B^\star$

strains < 0.15, above which, a brittle-ductile transition occurs.

5.3 Energy Distribution During the Quasi-static Confined Comminution of Granular Material

5.3.1 Energy Decomposition

Finding the decomposition of energy of a granular material subject to confined comminution is key to formulate a thermodynamically consistent breakage mechanics model. A lot of work was done towards this goal in the past decades.

Based on the theory of critical state soil mechanics, Roscoe *et al.* [129] established the following energy balance equation for a soil sample subjected to an increment of mean stress δp and an increment of deviatoric stress δq:

$$q\delta\varepsilon + p\delta\nu = \frac{\kappa\delta p}{1+e} + Mp\delta\varepsilon. \tag{5.11}$$

The left hand side of the equation represents the work done by the imposed mean and

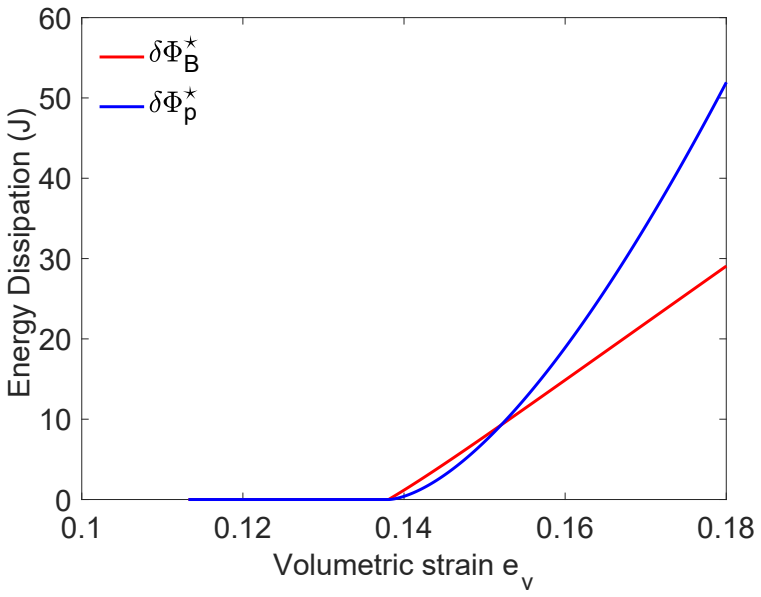

Figure 5.4: The relationship between the increment of energy dissipation and volumetric strain

deviatoric stresses, while the right hand side is the sum of the increments of internal energy and dissipated energy. Miura and Yamamoto [130] conducted a series of high pressure triaxial tests on quartz sand and studied the relationship between the increase of specific surface area ΔS and the plastic work δW_p. The ratio $\Delta S/\delta W_p$ was used as an index of particle crushing, and was related to the dilatancy rate. The model was validated later [56] against static triaxial compression tests and repeated triaxial tests on granitic soil. The plastic work included both friction dissipation and breakage energy. McDowell [39] developed further the theory of Roscoe *et al.* by introducing the breakage energy, expressed as:

$$\Phi_S = \frac{\Gamma dS}{V_s(1+e)} \tag{5.12}$$

In which Γ is the material surface free energy, which remains constant during a confined compression test. Recently, another form of energy dissipation, called redistribution energy, was introduced in the energy balance equation, in order to account for the rearrangement of grains around crushed particles. The complete energy balance equation was given

by [131]:

$$\delta W = \delta\Psi_e + \delta\Phi_p + \delta\Phi_S + \delta\Phi_{redist} \tag{5.13}$$

Where $\delta\Psi_e$, $\delta\Phi_p$, $\delta\Phi_S$ and $\delta\Phi_{redist}$ represent the elastic energy, friction dissipation energy, breakage energy and redistribution energy, respectively. Based on a calibration against two oedometer tests performed on silica sands, it was found that the ratio between the redistribution energy and the breakage energy, $R = \delta\Phi_{redist}/\Delta\Phi_S$, was between 13 and 16. In another study, the breakage energy amounted to 25% to 30 % of the total input energy [22]. A series of uniaxial compression tests conducted on samples of crushable sand of uniform distribution showed that the dissipation of energy by the creation of fracture surfaces depends on the confining stress, and that the fracture (or breakage) energy is predominant at low stresses and becomes less predominant at high stresses [23]. The distinction between pure breakage energy, friction energy and redistribution energy is still an open issue to date. The dissipation of energy by redistribution is triggered by breakage but increases due to the production of kinetic energy and friction energy. During quasi-static comminution, the production of kinetic energy is negligible in front of the other energy components. That is why in this chapter, which focuses on quasi-static comminution, we consider that the redistribution energy includes the friction energy. We use both empirical and numerical methods to calculate the energy dissipated by breakage and the energy dissipated by redistribution. We rewrite Equation 5.13 as:

$$\delta W = \delta\Psi_e + \delta\Phi_S + \delta\Phi_{redist} \tag{5.14}$$

5.3.2 Breakage Energy

The breakage energy is the energy needed to create new material surfaces when particles break [84]: it is the product of the surface free energy by the grain surface area created by breakage. The surface free energy is a material constant in the order of $0.1Nm/m^2$ to $1Nm/m^2$ for rocks and sands [132][133]. We obtain the grain surface area by calculating

the PSD and by estimating the surface area of particles within each size range. Note that in the following, we work with PSDs expressed in percentage of particle mass. During compression, particles break continuously due to the increasing contact forces. As a result, the number of fines as well as the total surface area of fragments increase with the compressive stress. At extremely high stress, an ultimate PSD is reached. It was shown empirically that the ultimate PSD can be represented by a fractal distribution [37, 69, 134, 38]:

$$F_u(r) = (r/r_M)^{3-\alpha} \tag{5.15}$$

Where α is the fractal dimension and r_M is the maximum particle size. In the following, we use $\alpha = 0.5$, which is consistent with experimental results obtained for various materials [38]. In the theory of breakage mechanics, the current PSD $F_c(r)$ is assumed to be an affine function of the initial PSD $F_0(r)$ and the ultimate PSD $F_u(r)$ [36, 10, 59]:

$$F_c(r) = (1 - B_r)F_0(r) + B_r F_u(r) \tag{5.16}$$

In which B_r is the breakage variable. A review of recents results obtained during quasi-static comminution indicates that Equation 5.16 is not a realistic representation of the PSD evolution, especially for larger particles [23, 127, 135, 31]. To overcome this limitation, we express the current PSD (updated at every step of the crushing process), as follows:

$$F_c(r) = (1 - a)F_b(r) + aF_u(r) \tag{5.17}$$

Where $F_u(r)$ is the ultimate fractal PSD and $F_b(r)$ is a uniform distribution, ranging between a size r_b and the maximum grain size r_M; a and r_b are fitting parameters. Similar to the breakage parameter B_r in Equation 5.16, the parameter a represents the evolution of breakage towards the ultimate fractal PSD (from $a = 0$ to $a = 1$). The model is based on the assumption that the initial PSD is uniform or quasi uniform, which is a common situa-

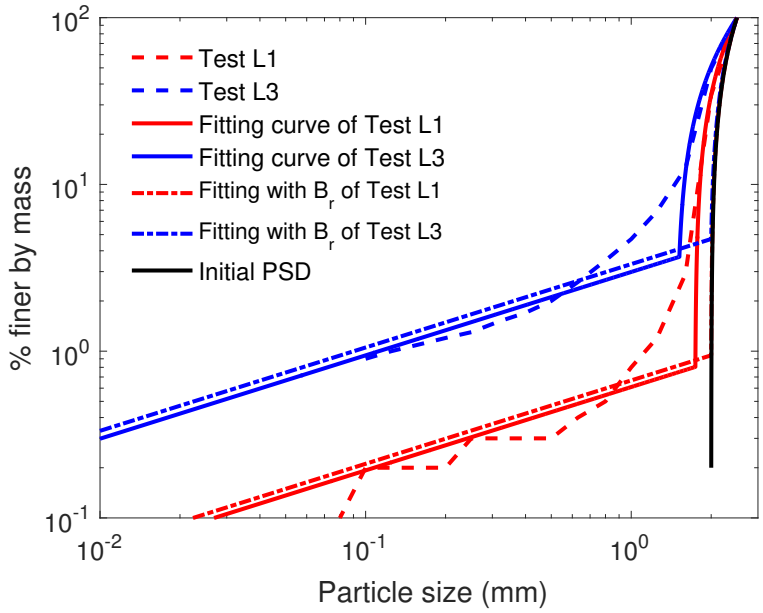

Figure 5.5: Particle size distributions and their best fit according to Equation 5.16 (B_r) vs. Equation 5.17

Table 5.1: Parameters a and d_b calibrated against uniaxial compression tests.

Test	$a(-)$	$r_b(mm)$
L1	0.0096	1.744
L2	0.0143	1.707
L3	0.0472	1.518
L4	0.0459	1.495
H1	0.2738	1.106
H2	0.6191	0.878
H3	0.8417	0.998

tion in laboratory experiments [136, 137]. Both parameters a and r_b are calibrated against the PSDs obtained at the end of confined comminution tests reported in [23] (tests L1 to L4) and in [127] (tests H1 to H3). The resulting PSDs of tests L1 and L3, obtained from Equation 5.17, are plotted in Figure 5.5. We also show that for larger particles, the final PSD obtained from the breakage mechanics model (Equation 5.16) is almost the same as the initial PSD, which results in a 50% error in the calculation of grain surface. The final PSD predicted by Equation 5.17 better captures the breakage of large particles. The results of the calibration of parameters a and r_b are summarized in Table 5.1.

The specific surface calculated from air permeability measures by Blaine's method is close to that obtained if particles are considered spherical [56, 138]. Therefore in the model, we consider that particles and fragments are spherical. Let us consider N size ranges within the interval of sizes $[r_m,\ r_M]$ represented in the PSD. At a given load increment, the surface area S^* of all particles having a radius r^* comprised between $r_1^* = r_m + \frac{n-1}{N}(r_M - r_m)$ and $r_2^* = r_m + \frac{n}{N}(r_M - r_m)$ is calculated as:

$$\begin{aligned} S^* &\approx \sum_{n=1}^{N} \frac{(F_c(r_2^*) - F_c(r_1^*))\, M_T S(r^*)}{\rho V(r^*)} \\ &\approx \sum_{n=1}^{N} \frac{(F_c(r_2^*) - F_c(r_1^*))\, M_T S(\frac{r_1^*+r_2^*}{2})}{\rho V(\frac{r_1^*+r_2^*}{2})} \end{aligned} \tag{5.18}$$

In which $S(r^*)$ is the surface of a particle of size r^*, $V(r^*)$ is the volume of a particle of size r^*, ρ is the mass density of the solid grains and M_T is the total mass of the sample. The current PSD $F_c(r)$ is obtained from Equation 5.17. At each increment, the total number of particles in the sample, N_T, is calculated by:

$$N_T \approx \sum_{n=1}^{N} \frac{3\, M_T\, (F_c(r_2^*) - F_c(r_1^*))}{4\pi\rho(\frac{r_1^*+r_2^*}{2})^3}. \tag{5.19}$$

Equations 5.17 and 5.18 allow estimating the change of material surface in the sample, thus the grain surface area created by breakage, which, multiplied by the surface free energy constant, provides the energy dissipated by breakage at each loading increment.

5.3.3 Redistribution Energy

Using Equation 5.14, the redistribution energy is calculated by subtracting the elastic energy and the breakage energy from the total work input. In the following, we explain how to calculate the total work input and the elastic deformation energy stored in the sample.

Total Energy

The total input energy is calculated from the force-displacement curve obtained in experiments. For an isothermal uniaxial compression test, the loading platen is the only source of energy input, which has the form:

$$\delta W = F\delta u \tag{5.20}$$

where F is the loading force and δu is the increment of displacement. Experimental results of force-displacement relationship for the tests reported in [23] and [127] are shown in Figure 5.6: the total work input is the area below each curve. Note that in tests L1 to L4, samples had different initial void ratios, which explains the different macroscopic stiffnesses observed in Figure 5.6.

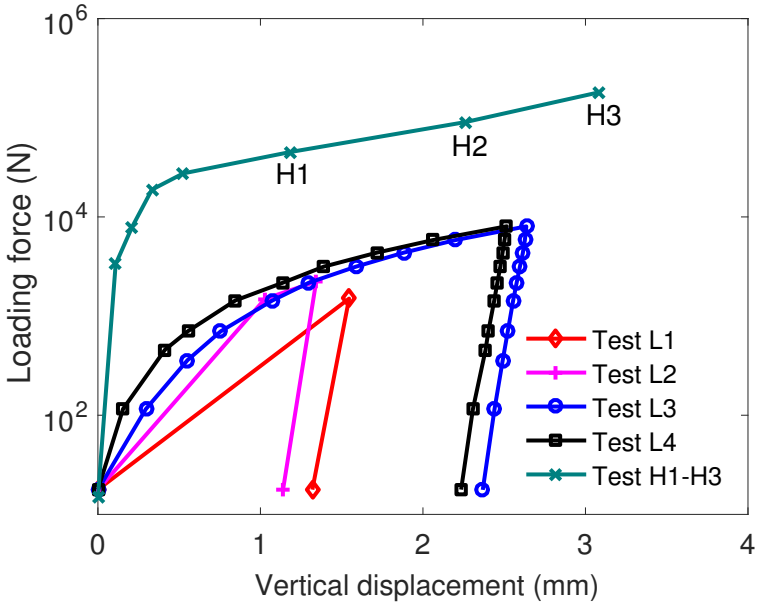

Figure 5.6: Load-displacement curve of uniaxial compression tests performed on crushable sand samples [23][127]

Elastic Energy

The elastic energy was calculated by using the DEM software PFC3D4.0 [89]. First, we generated samples that had the PSD obtained at the end of the confined comminution tests reported in [23] and [127] (Figure 5.5). The samples had the same sizes, weight and densities as in the experiments, and the PSDs were modeled with Equation 5.17. We subjected these samples to the same boundary conditions as in the experiments. The elastic energy is stored at the contacts between grains. Therefore, with the assumption of constant particle stiffness, the elastic deformation energy of the sample is

$$\Psi_e = 2\sum_{i=1}^{c} \frac{F_i^2}{2k_i} \tag{5.21}$$

Where c is the total number of contacts in the sample, F_i is the contact force (normal or shear force) and k_i is the stiffness of the particle (normal or shear stiffness, depending on the orientation of the contact force). In the DEM simulations, we assumed a linear relationship between the contact force and the contact displacement and we used the same value for the normal and shear stiffnesses. We used different stiffness values for tests L1-L4 on the one hand (ground shale) and for tests H1-H3 on the other hand (silica sand). Note that each contact contains two particles, so the elastic energy of the contact is twice that of the particle at that contact. Another way to obtain the elastic energy of the sample is to find the area below the unloading curve in Figure 5.6. However, the value obtained may be 50 to 60 percent less than the actual value of the elastic deformation energy, due to the existence of frozen elastic energy [139, 140]. Figure 5.7 shows the sample used for test H2, after compression. The parameters used in the simulation are reported in Table 5.2.

After creating the DEM samples, we found that the total number of particles in test L4 was about two million and that there were even more particles in tests H1, H2 and H3. DEM simulations were therefore highly computationally intensive. However, we noted

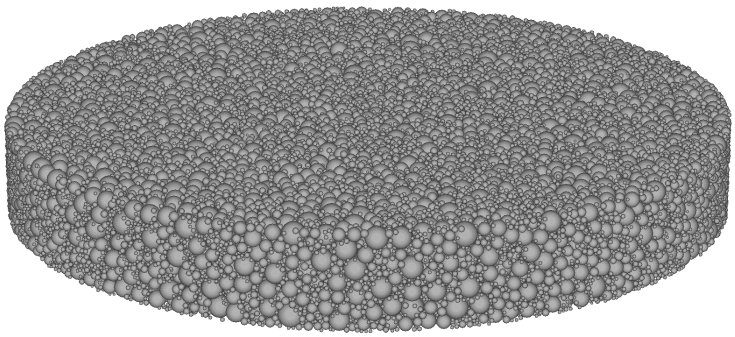

Figure 5.7: DEM sample used to simulate the uniaxial compression test H2

Table 5.2: Parameters used in the DEM simulations

Variable	Value
Density of sphere (ρ):kg/m^3	2750
Normal and shear stiffness in test L1 to L4: N/mm	4×10^2
Normal and shear stiffness in test H1 to H3: N/mm	1.5×10^3
Frictional coefficient of sphere(μ)	0.5
Number of particles L1-H3	8,000-130,800

that according to the final PSD obtained in test L4, particles with a diameter less than 0.1mm accounted for more than 98% of the total number of particles but for less than 1% of the sample weight. Moreover, particles with smaller radius usually have a lower coordination number than larger ones, and force chains usually contain larger particles [141][142]. The elastic energy of a particle increases with its size: in 2D, the elastic energy stored in a particle increases linearly with its radius [36]; here, in 3D, a quadratic correlation was found between the elastic energy and the particle size (see the example of sample H2 in Figure 5.8). As a result, small particles have less elastic energy and in average less contacts than larger ones. Based on these remarks, we performed the DEM simulations with truncated PSDs to increase the computational efficiency: particles with a radius below a radius threshold r_t were removed from the DEM samples. Details are provided in Table 5.3. The elastic energy of the removed particles was calculated by using an interpolation relating the elastic energy stored and the particle surface, like in the example of sample H2

Table 5.3: Description of the small particles removed from the DEM samples for the calculation of the elastic energy

Test	maximum removed size $r_t(mm)$	% of total mass removed
L1	-	0
L2	-	0
L3	0.11	1
L4	0.11	1
H1	0.14	8
H2	0.17	17
H3	0.20	22

in Figure 5.8 .

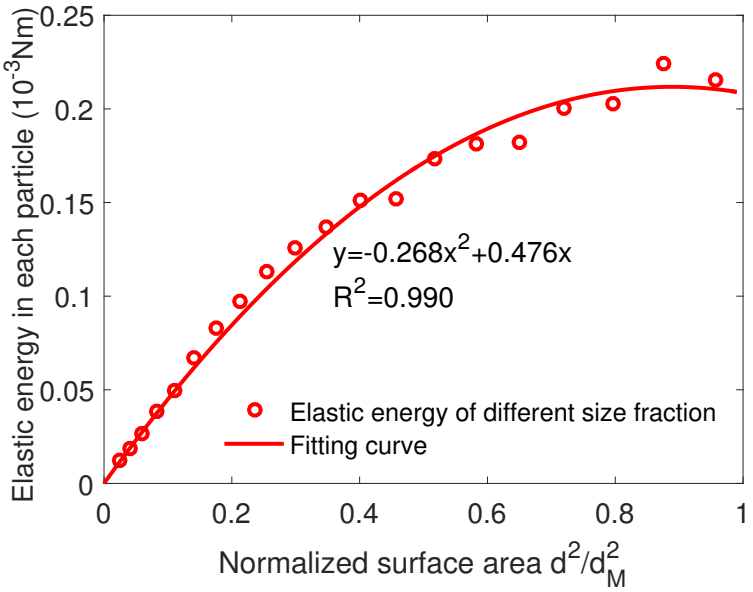

Figure 5.8: Relationship between the energy stored in each particle and the normalized particle surface area (test H2).

After generating the sample, we imposed a controlled velocity on the top platen to apply the uniaxial compression force. The force was continuously monitored during the loading process. When the force reached the value imposed in the experiment, we stopped loading and we calculated the total elastic energy stored in the sample from Equation 5.21. Note that it was not necessary to consider the crushing of particles here because the goal

for this simulation was only to obtain the elastic energy for a specific PSD under a given compressive stress. For each of the 7 tests (L1-L4, H1-H3), three simulations with different random seeds were conducted to guarantee a stable result.

5.3.4 Results and Discussion

DEM simulations allowed calculating the elastic energy stored in each sample under study, at the end of the confined comminution test. Results are shown in Table 5.4. As expected, the elastic energy increases with the loading force.

The initial void ratio, compressive stress and increase of specific surface are reported in

Table 5.4: Elastic energy at the end of confined comminution tests

Test	Simulation 1 (Nmm/g)	Simulation 2 (Nmm/g)	Simulation 3 (Nmm/g)	Average (Nmm/g)
L1	1.56	1.48	1.58	1.54
L2	2.31	2.28	2.31	2.30
L3	10.38	10.51	10.88	10.60
L4	13.31	13.39	13.35	13.35
H1	249.79	239.23	228.37	238.47
H2	891.40	882.44	881.15	884.99
H3	2352.90	2335.00	2336.55	2341.48

Table 5.5 for all tests. As expected, the specific surface increases with the loading force, see Figure 5.9. The value of the surface free energy for rocks ranges from 0.3 to 1.0 Nm/m^2 depending on microstructure and environmental conditions [132]. In this research, we use 0.5 Nm/m^2 to calculate the breakage energy. A summary of the results on energy distribution is provided in Table 5.6.

In order to see the role of each energy component during the comminution process, we normalized the data in Table 5.6 with the corresponding input energy. The results are shown in Figure 5.10.

Although the experiments used for model calibration refer to different materials, some

Table 5.5: Material surface increase during the compression tests

Test	Initial void ratio	Maximum stress (MPa)	Surface increase (mm^2/g)
L1	1.066	0.39	2224.84
L2	1.015	0.579	2537.18
L3	1.015	2.08	4195.36
L4	0.990	2.09	4280.13
H1	0.6±0.3	23.00	6.23×10^4
H2	0.6±0.3	46.00	3.10×10^5
H3	0.6±0.3	92.00	5.60×10^5

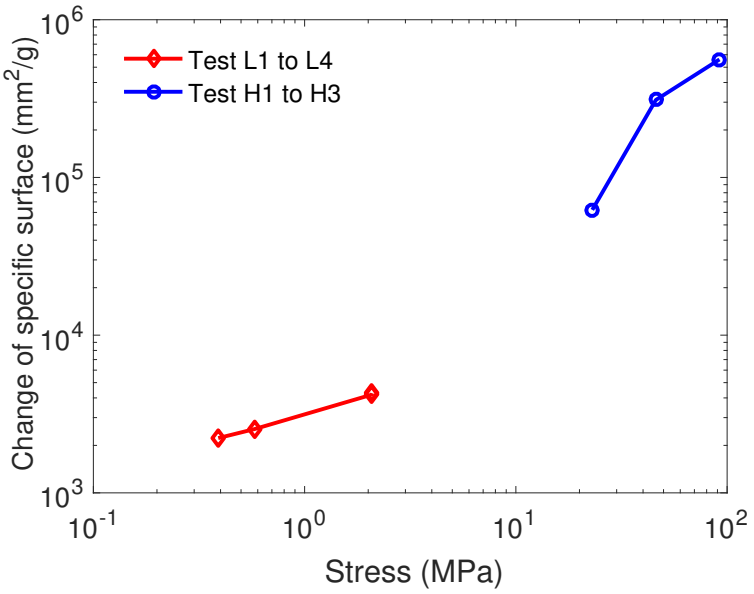

Figure 5.9: Relationship between loading force and surface increase

Table 5.6: Energy distribution at the end of the confined comminution tests (Unit:Nmm/g)

Test	Input energy	Breakage energy	Elastic energy	Redistribution energy
L1	23.82	1.54	1.10	21.18
L2	29.97	2.30	1.25	26.42
L3	74.67	10.60	2.10	61.98
L4	77.37	13.35	2.15	61.87
H1	926.17	31.15	238.47	656.52
H2	3136.33	154.95	884.99	2096.39
H3	6529.99	279.80	2341.48	3908.70

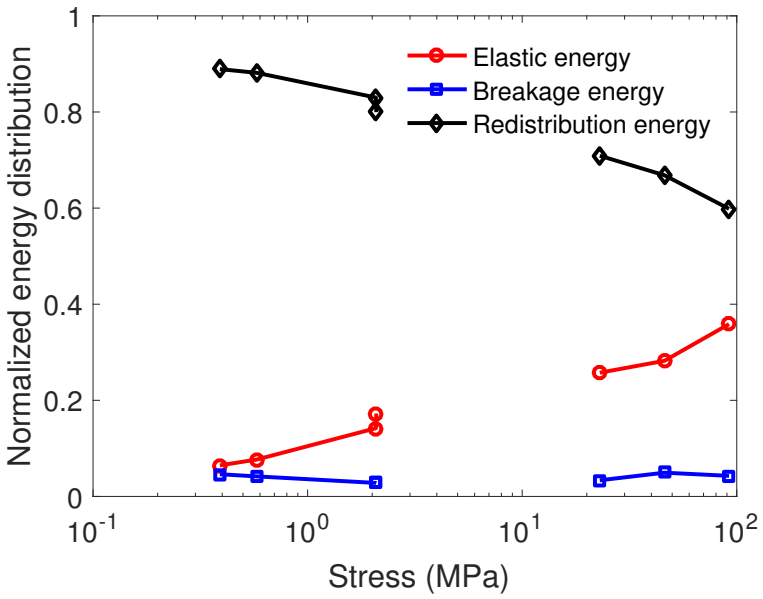

Figure 5.10: Evolution of normalized energy components

interesting conclusions can be drawn from Figure 5.10, mainly:

- In all tests, at least 60% of the work input is dissipated by particle redistribution.
- When the compression stress increases from 0.4MPa (test L1) to 92MPa (test H3), the redistribution energy decreases from 90% to 60% of the work input, and the elastic deformation energy increases from 10% to 40% of the work input.
- The breakage energy is less than 5% of the work input in all tests, i.e. the energy dissipated by breakage seems to represent a constant portion of the work input, regardless of the compression stress.
- The ratio between redistribution dissipation and breakage energy is between 14 to 30 in the tests, which is higher than the ratio between friction energy and breakage energy found by other authors (13 to 16). This result was expected, because in the proposed model, the redistribution energy is the sum of the friction energy and of the kinetic energy of the fragments.

5.4 Conclusion

In this chapter, we analyze the relationship between microstructure evolution and the evolution of energy components in assemblies of breakable grains. We first propose to redefine the coupling angle used in breakage mechanics to couple the breakage and plasticity yield surfaces as a function of the breakage parameters, which allows capturing the transition from brittle to ductile behavior at the macroscale.

Then, we propose a method to calculate the distribution of energy in seven particulate assemblies subjected to confined comminution, under compressive stresses ranging from 0.4 MPa to 92 MPa. The work input, calculated by integrating the load-displacement curve, is written as the sum of the elastic deformation energy, the breakage energy and the redistribution energy (plastic dissipation). The elastic energy stored in the seven samples at the end of the compression tests is obtained by simulating a compression test on the final PSDs with the DEM, and by extracting the contact forces. A PSD evolution law is proposed to account for particle breakage, for which parameters are fitted to match the final PSDs obtained experimentally. At each loading step, the current PSD is related to the total particle surface in the sample, which allows calculating the breakage energy. The redistribution energy, which comprises the kinetic energy of particles being rearranged and the friction energy dissipated at contacts, is obtained by subtracting the elastic energy and breakage energy from the work input. Results show that: (1) At least 60% of the work input is dissipated by particle redistribution; (2) The fraction of elastic deformation energy increases and the fraction of redistribution energy decreases as the compression stress increases; (3) The breakage energy accounts for less than 5% of the total input energy, and this value is independent of the compressive stress; (4) The energy dissipated by redistribution is between 14 to 30 times larger than the breakage energy. The evolution of the relative energy fractions confirms that the coupling angle is not a constant material parameter, but rather, a function of the breakage index.

This research is expected to increase the fundamental understanding of microstructure changes during confined comminution and to provide a concrete foundation to establish energy based constitutive relationships for granular materials. Results could be used to design microstructures that do not crush and store potential elastic deformation energy, or microstructures that do crush to dissipate the energy of a shock, for example. Energy models are expected to be useful to optimize the fabrication process of granular materials and powders.

CHAPTER 6
DEM ANALYSIS OF THE EFFECT OF AGGREGATES AND ITZ ON CONCRETE STRENGTH

6.1 Introduction

The amount of concrete used worldwide is twice that of steel, wood, plastics, and aluminum combined. It is estimated that more than 11 billion metric tonnes of concrete are used every year [143]. Concrete is composed of coarse aggregates and mortar, which itself is made of fine particles (e.g. sand grains) and cement. The heterogeneous micro-structure of concrete brings many analytical, numerical and experimental challenges in material property characterization. In this chapter, we focus on the modeling of fracture pattern formation in concrete. Cracks in concrete occur at different scales, due to structural loading, thermal gradients, shrinkage or wet/dry cycles. Large tensile cracks (width$>$0.1 mm) can be controlled by proper design, e.g. by embedding steel reinforcementin concrete structural members. But microcracks, which usually exist at the aggregate-cement interface, are much harder to control.

The objective of this study is, therefore, to understand the micro-mechanisms that drive fracture propagation in concrete and assess the influence of aggregates on concrete strength. We describe a DEM model of concrete, in which coarse aggregates are represented by particle clusters of realistic shape, and mortar is represented by bonded spherical particles. First, we generate a sample made of spherical rigid elements bonded together. For this purpose, we introduce a bond displacement-softening law. Aggregate centroids are then randomly placed in the DEM sample. We use CT scan images of real aggregates to plot 3D aggregate contours. The spherical elements that are contained in 3D contours around the randomly placed centroids are replaced by clusters. The number and size of the clusters

are determined from the experimental Particle Size Distribution of the aggregates. We first simulate Brazilian tests and uniaxial compression tests done on mortar by using the DEM model without clusters, and we calibrate the mortar DEM parameters. We then use Brazilian tests and uniaxial compression tests performed on concrete to calibrate the remaining parameters of the concrete DEM model with clusters. We then study the effect of aggregate shape on concrete tensile strength and uniaxial compressive strength. A sensitivity analysis is conducted to understand the impact of aggregate strength and of aggregate/mortar bond strength on concrete properties.

6.2 Experimental results of Brazilian tests and uniaxial compression tests done on mortar and concrete

The Brazilian test (BT) is an ASTM standard test method used to determine the splitting tensile strength of cylindrical concrete specimens [144]. A disc-shaped specimen is compressed between two diametrically opposite loading strips. Tensile stress develops at the center of the specimen [145]. Because the procedures are simple and the specimen preparation is easy, the Brazilian test has been widely used as an indirect method to test the tensile strength of concrete and rock. The tensile strength, σ_t, is given by:

$$\sigma_t = \frac{P}{\pi R t} \tag{6.1}$$

where P is the peak load and R and t are the radius and the thickness of the specimen, respectively.

The uniaxial compression test (UCT) is used to measure the compression strength of cylindrical mortar/concrete specimens under zero confining stress. The uniaxial compressive strength (UCS), σ_c, is given by:

$$\sigma_c = \frac{P}{\pi R^2} = \frac{P}{A_0} \tag{6.2}$$

where A_0 is the initial cross sectional area of the specimen.

Concrete is made of coarse aggregates and mortar. The Interfacial Transition Zone (ITZ) between coarse aggregates and mortarmakes it challenging to calibrate DEM models of bonded particles. We proceed by first calibrating a mortar DEM model, and then calibrating aggregate cluster properties against concrete mechanical test results, using the calibrated mortar parameters. The experimental results used for calibration, presented below, were obtained at the Georgia Tech Structural Engineering Laboratory, in partnership with Dr. L. Stewart's group in the School of Civil and Environmental Engineering.

6.2.1 Brazilian tests and uniaxial compression tests done on mortar

Samples used for the Brazilian tests were 150 mm in diameter and 100 mm in thickness (150 $\times$ 100). The ratio diameter/thickness was chosen so as to avoid size effects [146, 121]. All cylinders were cast and stored in a fog room for 28 days before the tests. Three Brazilian tests and three uniaxial compression tests were conducted. Results are shown in Figure 6.1 and 6.2, respectively. A brittle failure was observed both in hte BTs and the UCTs: stress increases with the strain until a peak value (strength) is reached, after which stress drops abruptly. The average Brazilian tensile strength was 4.71 MPa and the average compressive strength was 61.42 MPa. Less than 10% variability was noted for both BT and UCT strength results.

6.2.2 Brazilian tests and uniaxial compression tests done on concrete

Concrete specimens were 150 mm in diameter and 300 mm in thickness. We performed three BT and three UCT on concrete after a period of 28 days of curing time. Test results are shown in Figure 6.3 and 6.4. Concrete specimens also exhibited a brittle behavior. The average Brazilian tensile strength was 2.69 MPa and the average compressive strength was 32.53 MPa, which corresponds, respectively, to 57% of the tensile splitting strength of mortar and to 53% of mortar compressive strength. By observing the fracture surfaces

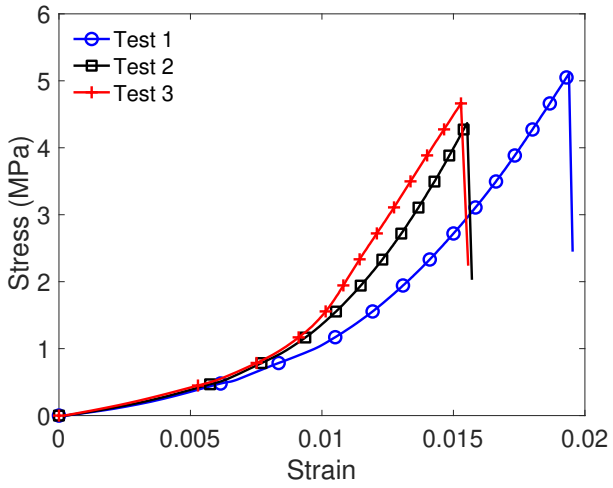

Figure 6.1: Stress-strain curves of mortar cylinders in the Brazilian tests

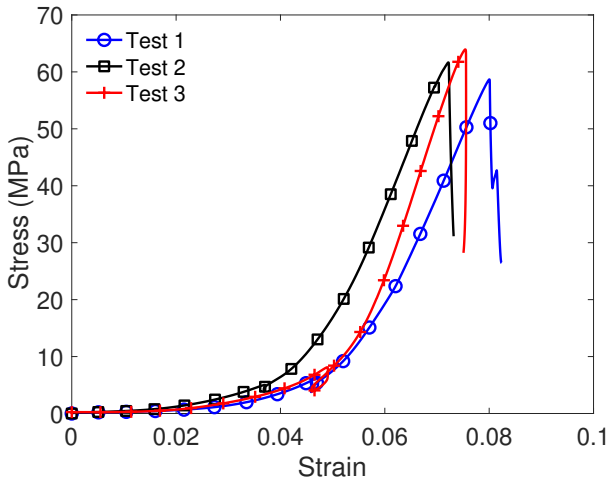

Figure 6.2: Stress-strain curves of mortar cylinders in the uniaxial compression tests

after the tests, we found that fractures had propagated in mortar, in the aggregates and at the mortar/aggregate interfaces. A large number of aggregates were crushed and new fracture surfaces had appeared in the aggregates. These observations differ from previous experimental results reported in the literature [147], in which it was noted that fractures are more likely to propagate at the ITZ. Figure 6.5 shows the fracture surfaces after a test. Table 6.1 summarizes the average strength results.

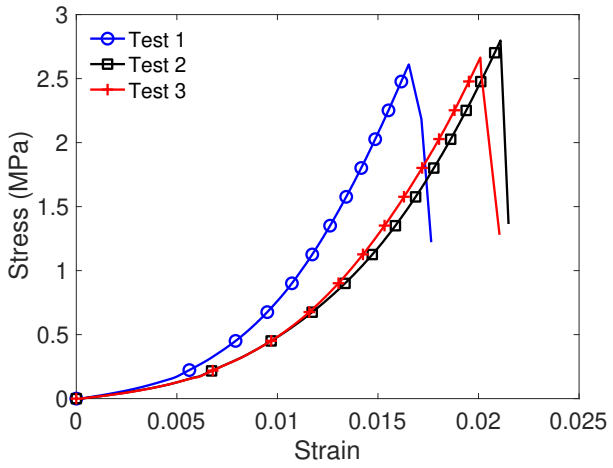

Figure 6.3: Stress-strain curves of concrete cylinders in the Brazilian tests

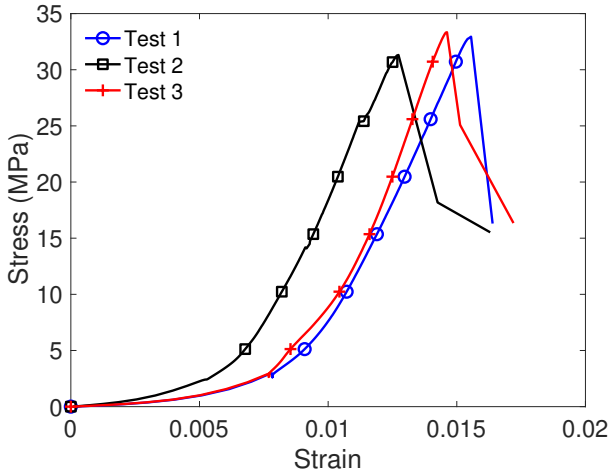

Figure 6.4: Stress-strain curves of concrete cylinders in the uniaxial compression tests

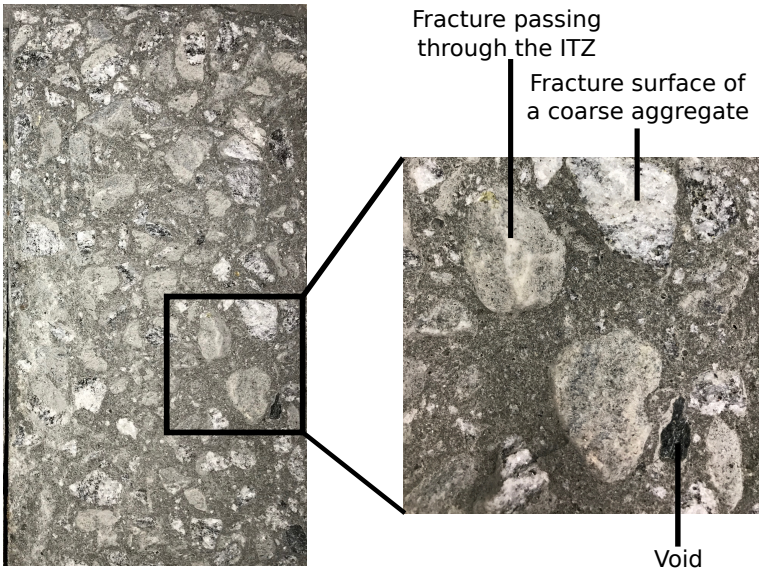

Figure 6.5: Open surface of a specimen after a Brazilian test, showing fractures passing through both coarse aggregates and ITZ

Table 6.1: Average tensile splitting strength and uniaxial compressive strength of mortar and concrete

Materials	Tensile strength (MPa)	Uniaxial compressive strength (MPa)
Mortar	4.71	61.42
Concrete	2.69	32.53

6.3 Discrete element model construction

6.3.1 Displacement softening contact bond model

The mechanical properties of the spherical elements that make a DEM model are the normal stiffness k_n, the normal/shear stiffness ratio k_n/k_s, the friction coefficient μ and the mass density ρ. In addition, a bond model is required to capture crack propagation in the DEM simulations. Experimental results reported in numerous studies indicate that, after the maximum load has been reached, concrete exhibits a gradual decrease of loading capacity with increasing strain/displacement [148, 149, 150]. To capture this softening behavior, we propose a displacement-softening contact model, inspired by the bond model proposed by Ma and Huang [46]. Figure 6.6 illustrates the normal and shear force-displacement curves employed in the contact model, which is governed by the following five microparameters: normal loading stiffness k_{nl}, maximum normal force F^n_{max}, normal softening stiffness k_{ns}, bond stiffness ratio k_{nl}/k_{sl} and maximum force ratio F^s_{max}/F^n_{max}. The maximum normal force F^n_{max} is given by:

$$F^n_{max} = \pi(R_1 + R_2)^2\sigma_t/4 = A_0\sigma_t, \tag{6.3}$$

where R_1 and R_2 are the radii of the two particle in contact; σ_t is the bond tensile strength; A_0 is the bonding area. Equation 6.3 is based on the assumptions that the bonding area between two spherical particles has a disc shape with diameter equal to the average radius of the two particles in contact. The maximum tensile force that a bond can carry is the product of the bonding area by the tensile strength. The maximum force ratio F^s_{max}/F^n_{max} is equal to the bond strength ratio τ/σ_t. Therefore, two sets of micro-properties are used in our DEM simulations, i.e. the micro-properties of the particles:

$$\{k_n, k_n/k_s, \mu, \rho\} \tag{6.4}$$

and the micro-properties of the displacement softening contact bond model:

$$\{k_{nl}, \sigma_t, k_{ns}, k_{nl}/k_{sl}, \tau/\sigma_t\}\,. \tag{6.5}$$

The relationships between the above micro-properties and the macroscopic properties of the mortar and concrete DEM samples are discussed below.

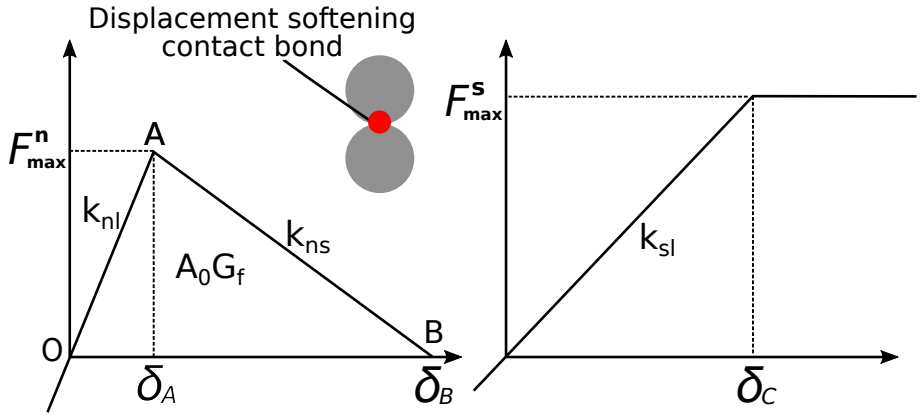

Figure 6.6: Force-displacement relationships used in the displacement softening contact bond model

In our analysis, we followed the method proposed in [99] and [119] to define particle microparameters, as follows:

$$k_n = 4RE, \tag{6.6}$$

$$k_n/k_s = E/G, \tag{6.7}$$

$$\rho = (1+n)\rho_{mat}, \tag{6.8}$$

where R is the particle radius; E and G are the Young's modulus and shear modulus of the material represented by the DEM sample, respectively; ρ_{mat} is the mass density of the material and n is the porosity of the DEM specimen (around 35% in 3D simulations).

The normal loading stiffness k_{nl} is set equal to the average of the normal stiffnesses of the two bonded balls. The bond tensile strength is set equal to the tensile strength of the material represented by the DEM sample. In our displacement softening contact model,

the bond shear strength is set much higher than tensile strength and shear stress does not affect the bond breakage. This is a realistic hypothesis for DEM models of bonded and aggregated materials, according to [151, 47]. The energy used to break a bond, which is the area of OAB in Figure 6.6, is equal to the product of the fracture energy, G_f, by the bonding area, A_0. The normal softening stiffness k_{ns} is expressed as:

$$k_{ns} = \frac{(F^n_{max})^2 k_{nl}}{2G_f A_0 k_{nl} - (F^n_{max})^2}. \tag{6.9}$$

The remaining two contact bond parameters, k_{nl}/k_{sl} and τ/σ_t, control the shear behavior of the material. In former studies [47, 151], a realistic ratio between the uniaxial compressive strength and the Brazilian tensile strength (between 10 to 20 from most geomaterials) could be obtained with a high stiffness ratio and strength ratio. Here, we calibrate k_{nl}/k_{sl} and τ/σ_t against experimental results. To summarize, the required micro-properties in Equation 6.4 and 6.5 can be expressed in the form:

$$\{E, G, \mu, \rho_{mat}, \sigma_t, G_f, k_{nl}/k_{sl}, \tau/\sigma_t\} \tag{6.10}$$

6.3.2 Generation of the mortar sample

We generated the cylinder specimens with the method proposed in [99], which will be briefly introduced here. In a first step, an assembly of particles is generated in a material vessel. The number of particles generated depends on the volume of the vessel, an estimated porosity (35% for 3D model) and the given average particle size. At this time, all particles are randomly located and may overlap, as shown in Figure 6.7(a). Then the radii of all particles are modified uniformly so that an isotropic target stress, which is set to 1% of the uniaxial compressive strength, can be achieved at all boundaries. Large overlaps between particles are eliminated and force chains are generated (Figure 6.7(b)). In Figure 6.7(c), darker grey particles represent the "floating" particles, with a coordination number

less than 3. By adjusting the radius of these particles, we can increase their coordination number and obtain a densely packed sample. In a second step, we assign the displacement softening contact bond at all particle-to-particle contacts. Lastly, we remove the bounding walls and we relax the material, as shown in Figure 6.7(d).

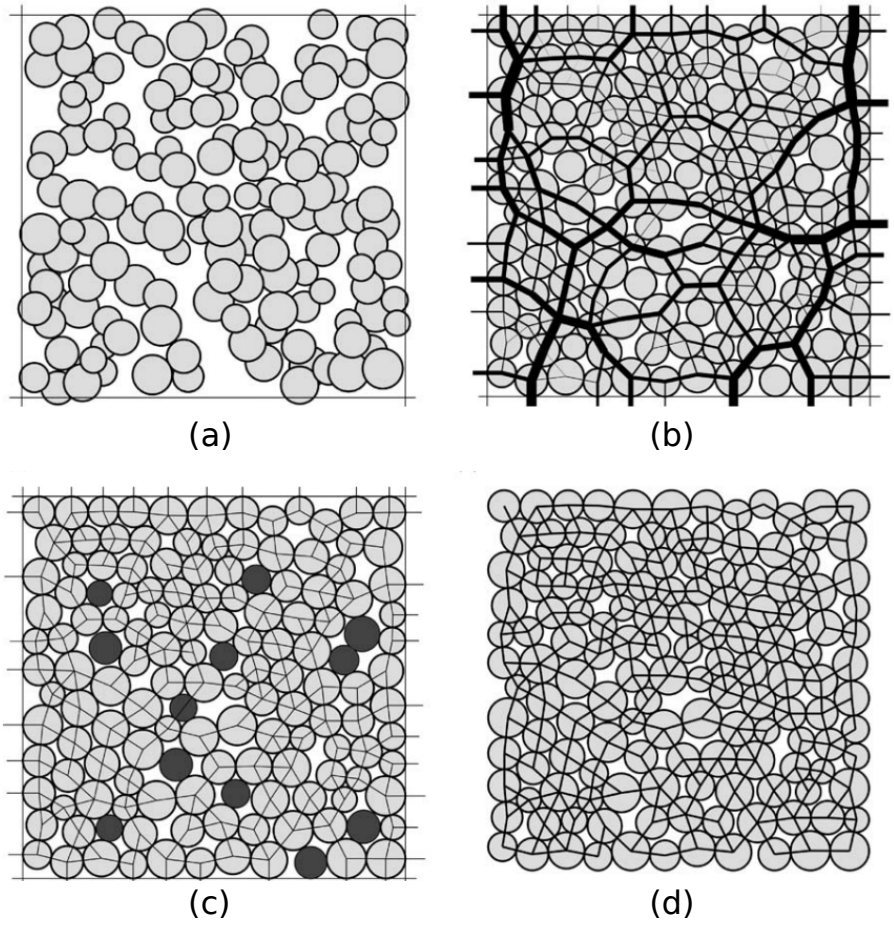

Figure 6.7: Sketch illustrating the material-genesis procedures [99]

In our simulation, a cuboid mortar sample is first generated and then cut into the desired size and shape – in this case, 150 $\times$ 100 cylinders for BTs and 100 $\times$ 200 cylinders for UCTs, like in the experiments. The minimum particle particle size was 1 mm and the size ratio between maximum particle size and the minimum particle size is 1.66. In each simulation, we had 120,000 to 130,000 particles and it usually took 12 hours on a workstation (i7-3770 3.4GHz CPU and 64 GB RAM) to simulate one test. DEM specimens for the BTs

and UCTs are shown in Figure 6.8(a) and (b), respectively.

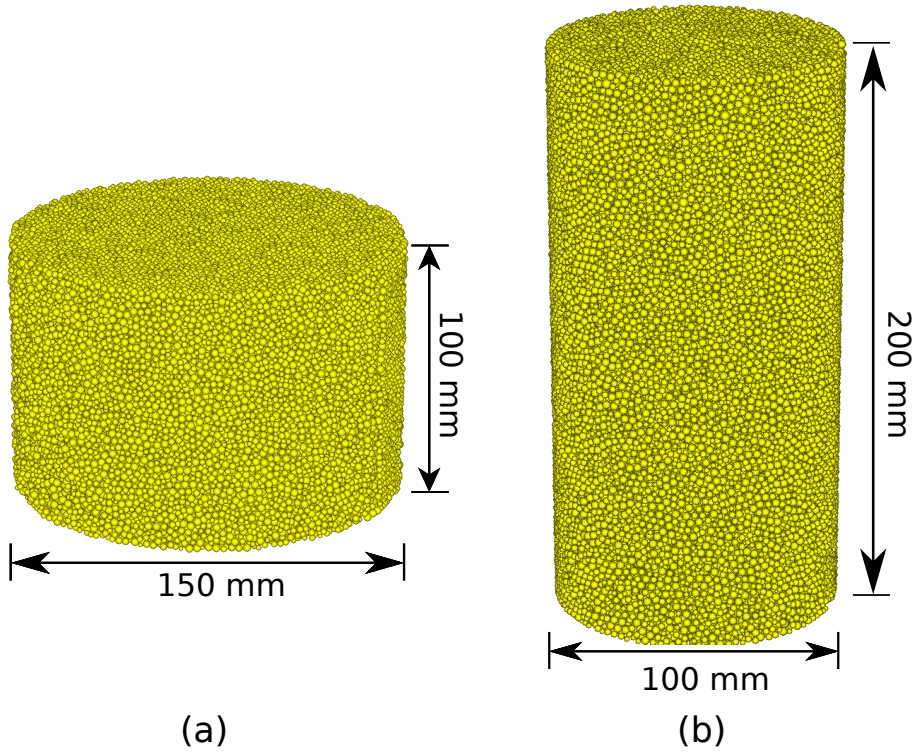

Figure 6.8: Mortar DEM specimens used in the (a) Brazilian tests and the (b) Uniaxial compression tests

6.3.3 Generation of the concrete sample

In order to generate realistic aggregate shapes, we scanned 20 representative aggregates with an X-ray scanner. Aggregate shapes were characterized by 20,000 to 30,000 points, which provided detailed information about particle shapes and surface textures. However, the aggregates modeled with the DEM usually contain 100 to 200 spherical elements, reduce the computation time needed for the generation of the DEM sample. We thus simplified the raw dataset by decrease the density of the points at the surface of the aggregates, so as to limit the computation time while maintaining geometric accuracy. Figure 6.9 shows the original scan data, the simplified data and the corresponding DEM shapes obtained for four aggregates.

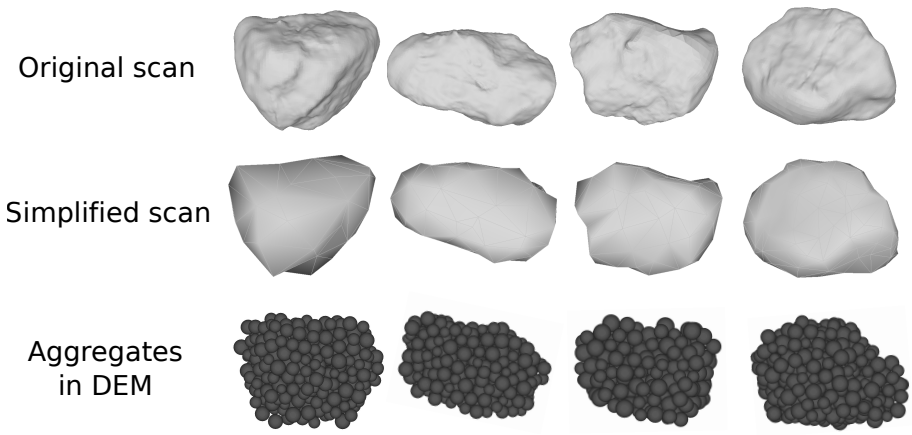

Figure 6.9: Generation of aggregate shapes in the DEM model

The DEM concrete model is generated as follows:

1. Create the mortar sample using the method presented in Section 6.3.2.

2. Calculate the number, sizes and positions of the aggregates. The number of coarse aggregates in each fraction size, n_i is given by

$$n_i = V_t \eta (P_{2i} - P_{1i})/V_i \tag{6.11}$$

where V_t is the total volume of the specimen; η is the volume fraction of the coarse aggregates; P_{1i} and P_{2i} are the percentage of aggregates finer than d_{1i} and d_{2i} in the PSD curve; V_i is the average volume of an aggregate in this size fraction. Within each size fraction, the size of an aggregate is assumed to follow a uniform distribution. A MATLAB code was written to generate non-overlapping spheres within the sample boundary, with the given number of aggregates and the given aggregate sizes. Each sphere generated by the MATLAB code corresponds to an aggregate of specific volume.

3. Replace the spheres by realistic aggregate shapes. We replace each sphere with a realistic shape randomly chosen from the set of shapes obtained by X-ray scanning

(here, we used 20 different aggregate shapes). After the replacement, some aggregates may overlap, which slightly decreases the total volume fraction of the aggregates. In addition, some aggregate fractions may be outside of the boundary of the specimen.

4. Find the spherical elements and the contacts within the aggregates. Another MATLAB algorithm is created to loop through all spherical elements and contacts, and check whether they belongs to an aggregate or not. Then the aggregate volume fraction is calculated as the ratio of the number of spheres in the aggregates by the total number of spheres in the specimen. We compare this volume fraction with the volume fraction found experimentally, update the parameter η accordingly, and repeat step 2 to 4 if the difference is larger than 1%.

5. Change the properties of the spherical elements and bonds in the aggregate shapes and in the ITZ. To account for the local increase of porosity in the ITZ, we removed a certain portion of displacement softening contact bonds at the aggregate/mortar interface.

6. Generate voids. Another important difference between mortar and concrete is the void ratio. An estimated void ratio of 4% is used in our model, which is a reasonable estimation according to images of X-ray Computed Tomographic images obtained in [152].

Figure 6.8(a) and (b) show the DEM concrete samples used to simulate the BTs and UCTs, respectively.

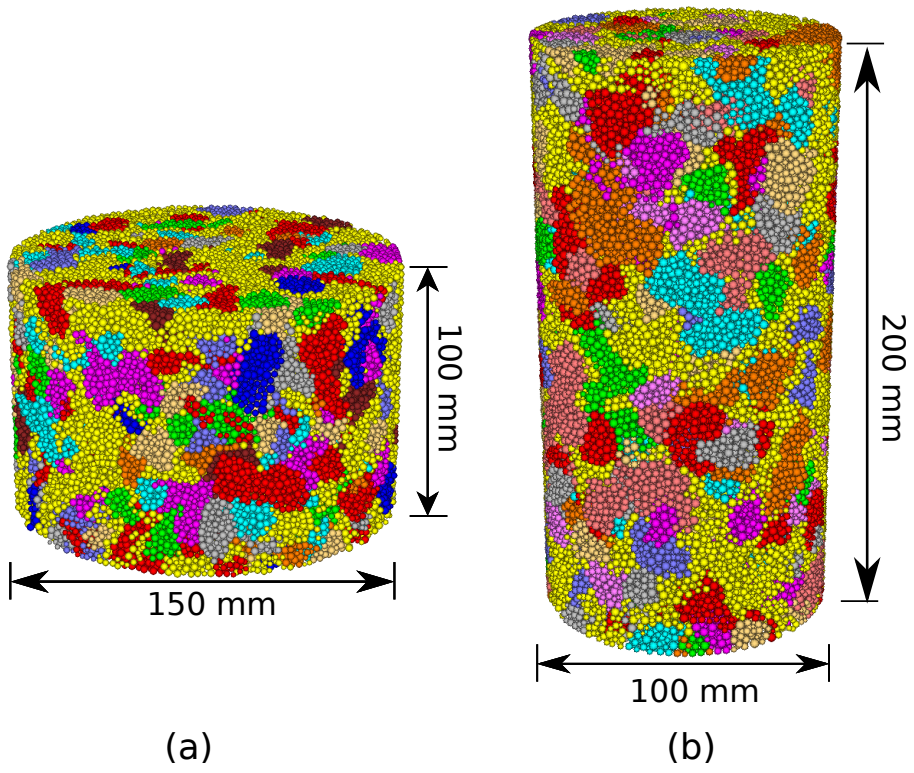

Figure 6.10: DEM concrete specimens used to simulate (a) Brazilian tests and (b) Uniaxial compression tests

6.4 Calibration of the DEM concrete model

6.4.1 Mortar model calibration against experimental results

We obtain mortar's Young's modulus from the empirical equation proposed in ACI 318:

$$E = 4700\sqrt{f'_c}, \tag{6.12}$$

where f'_c is the uniaxial compressive strength, reported in Table 6.1. Following [143], we assume that the mortar's Poisson's ratio is 0.2. The shear modulus G is then given by $E/(2(1+\mu))$. For the DEM friction coefficient, we use an empirical value of 0.5, recommended in the state-of-the art [123]. The mass density of the particles used in the mortar DEM model is calculated from Equation 6.8. The tensile strength of the bonds, σ_t, is set equal to that of the mortar specimen. Due to the size effects that occur in Brazilian tests, the tensile strength reported in Table 6.1 is higher than the tensile strength of the material tested [44]. We use the relationship proposed in [153] to calculate mortar tensile strength from the BT strength and the specimen diameter. For mortar, G_f ranges from 20 N/mm to 200 N/mm, depending on the type of mortar [146, 154, 155, 156, 157]. In our simulation, we use G_f = 80 N/mm,, because this value provides the best fit with experimental results. With the DEM, it is challenging to simulate BTs and UCTs with a realistic ratio uniaxial compressive strength over Brazilian strength (UCS/BS). Different methods were used in previous studies, for example by generating angular particles to increase the interlocking forces, increasing the initial compressive strength, modifying the strength ratio, and creating new contact models [47, 151, 158]. In our displacement softening contact model, the ratio of UCS/BS is mainly controlled by two parameters: k_{nl}/k_{sl} and τ/σ_t. In a Brazilian test, the failure mechanism is a combination of shear failure at the loading point and tensile failure at the center [159]. A low k_{nl}/k_{sl} decreases the shear stress, thus yielding a lower Brazilian tensile strength. A large τ/σ_t increases the shear strength measured in the uniax-

ial compressive test. Mortar parameters obtaied after calibration are summarized in Table 6.2.

Table 6.2: Mortar DEM model parameters

Parameter	Mortar	Aggregate
Young's modulus E: GPa	36.8	36.8
Shear modulus G: GPa	30.7	30.7
Friction coefficient μ	0.5	0.5
Density ρ_{mat}: kg/m^3	2400	2400
Tensile strength σ_t: MPa	3.85	3.5
Fracture energy: N/m	80	72.7
Stiffness ratio k_{nl}/k_{sl}	6.0	6.0
Strength ratio τ/σ_t	20	20

We conducted the simulations of the UCT and the BT twice to check that DEM randomization effects would not affect the calibration results. Simulation results are presented in Figures 6.11 to 6.14. The BTS and UCS are in agreement with the strenghts measured experimentally, with an error of less than 5%. The ratio of UCS/BS, which is around 13.0 in our experiments, is properly reproduced in the DEM simulations. Figure 6.12 shows the location of broken bonds at several stages of the BTs. At 50% of the peak load, micro-cracks appear near the loading platens, which is typical of a loacal shear mechanism close to the loading supports. At 90% of the peak load, the number of cracks near the loading platens increase. In addition, micro-cracks appear at the center, which reveals a tensile failure mechanism, induced by horizontal tensile stress. At the peak load, the micro-cracks which originated at the center propagate to wards the loading platens. After the peak, the specimen rapidly breaks into two fragments.

In the UCT, we observe randomly distributed micro-cracks at 50% of the peak load. No obvious shear band or fracture can be identified at this point. When the load reaches 90% of the peak load, we can observe more micro-cracks, preferentially oriented along the directions of two shear failure planes (shear bands). At this loading stage, the stiffness of the material starts to decrease due to material softening induced by micro-crack propagation.

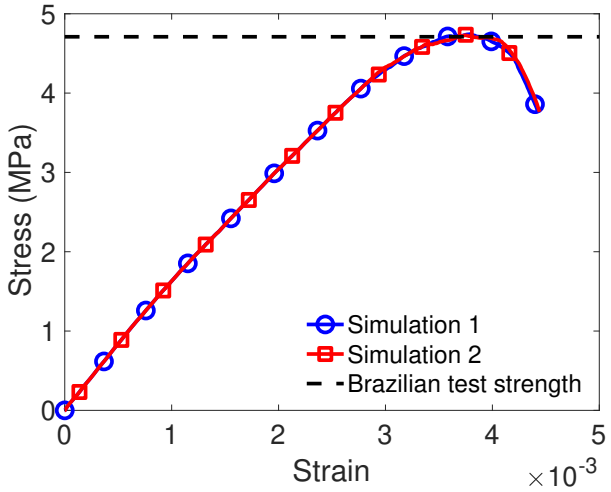

Figure 6.11: Stress-strain curves of mortar in the Brazilian tests simulated by the DEM

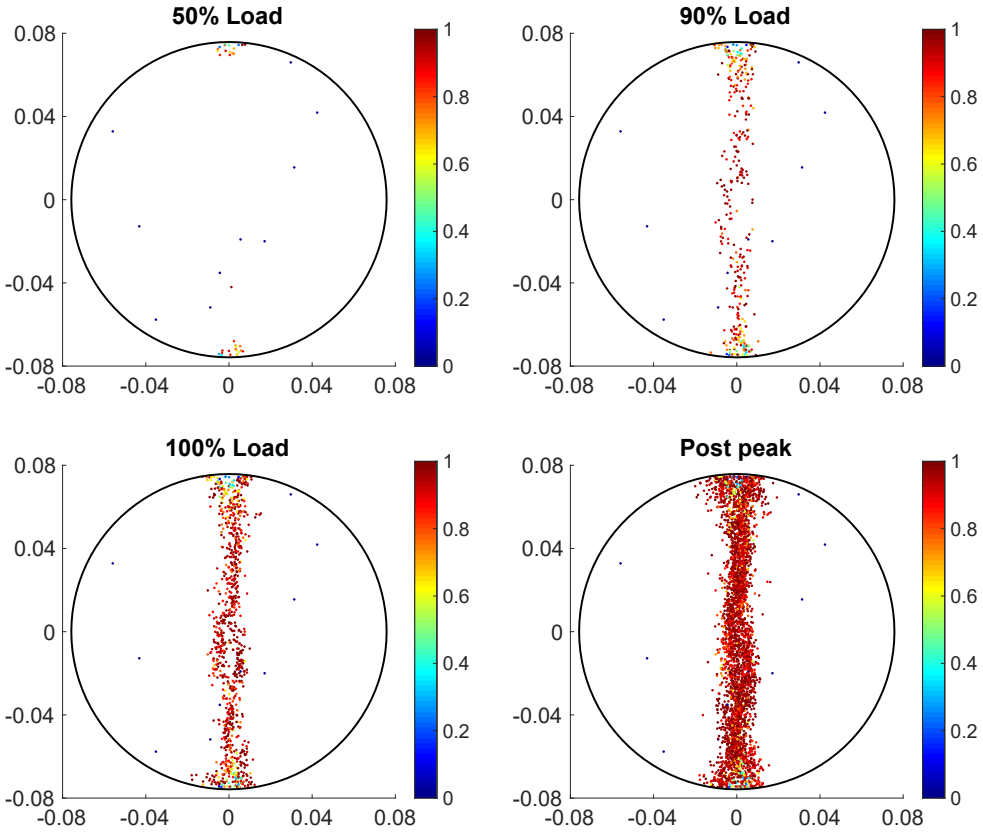

Figure 6.12: Micro-cracks in mortar at different stages of the Brazilian tests

As we continue loading from 90% to 100% of the peak load, the number of broken bonds in the shear bands increase rapidly. Figure 6.14 clearly shows a fracture pattern characterized by more than one oblique plane. Note that these failure planes are not parallel to each other [160]. This failure mode is one of the four most common failure modes reported by ASTM codes [161], along with diagonal fractures, columnar vertical cracks and the combination of conic and vertical cracks. The observed failure mechanism is typical of fixed ends boundary conditions, [162, 163], in which strong confinement is used at loading platens to prevent any lateral displacement of the specimen. The fixed ends boundary condition is used in both our experiments and simulations.

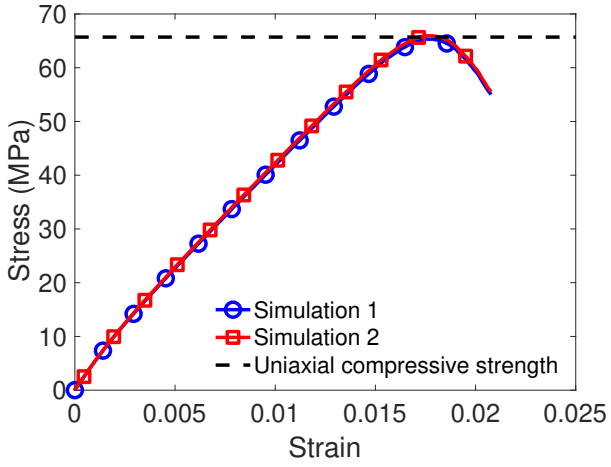

Figure 6.13: Stress-strain curves of mortar in the uniaxial compression tests simulated by the DEM

6.4.2 Concrete model calibration against experimental results

The coarse aggregates used in the concrete tested in our experiments are made of granite from Norcross, GA. In most concretes, coarse aggregates are found to be much stronger than mortar and have much lower probability to break [147, 164]. Contrary to those observations, in both the BTs and UCTs we conducted, a large number of coarse aggregates were crushed and fresh aggregate surfaces were exposed, which indicates that aggregates had a lower tensile strength and a lowaer compressive strength than mortar. Not surprisingly, our

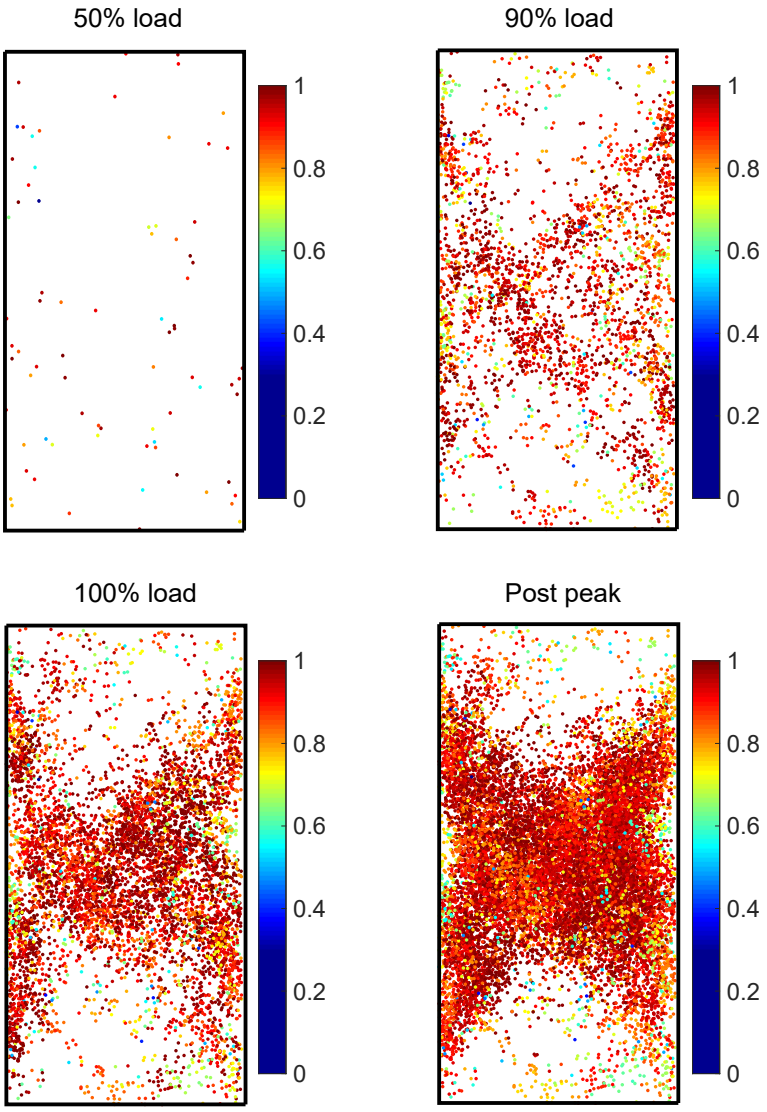

Figure 6.14: Micro-cracks in mortar at different stages of the uniaxial compression tests

calibration simulations yield a lower bond strength σ_t for coarse aggregates than for mortar. In addition, we assume that the ultimate bond displacement at failure is the same as that of mortar, so that the fracture energy of aggregates, G_f, is proportional to the aggregate bond strength. The ITZ also contributes to the relative lower strength of concrete compared to that of mortar [25]. The existence of coarse aggregates leads to a local increase in porosity and thus to a smaller bond area between aggregates and mortar. To account for the effect ofthe ITZ, we removed 20% of the displacement softening contact bonds between aggregate particles and mortar particles. This value of 20% was obtained by trial and error. The effect of this ratio on concrete strength will be discussed in the next section.

We conducted the BT and UCT simulations three times, to check if DEM randomization would have any effects on the results. Simulation results are shown in Figures 6.15 to 6.18. The coarse aggregate properties obtained after calibration are summarized in Table 6.2. Concrete stress-strain curves are similar to those of mortar. However, because the coarse aggregates increase the heterogeneity of the specimens, a variability of 16.0% (respectively 7.0%) is observed for the BTS (respectively UCS) among the three simulations (Figures 6.15 and 6.17). The sequence of bond breakage events in concrete is similar to that in mortar. In the BT, micro-cracks first appear at the loading platens but the failure is caused by tensile micro-cracks that originate at the center of the specimen and then propagate towards the platens. The failure plane after the peak load is not a straight line, because of the specimen heterogeneity caused by the presence of aggregates. Like in mortar, multiple shear failure planes are observed, see Figure 6.18. Due to the lower loading capacity of concrete, the number of micro-cracks is less than in mortar. In other words, fractures form at an earlier stage, passing through the weak aggregates and the ITZ. A detailed analysis of the influence of the relative fraction of inactive bonds at the ITZ will be presented in the next section. To sum up, the existence of coarse aggregates greatly affects both the BTS and the UCS, but the presence of aggregates does not influence the failure mechanisms involved.

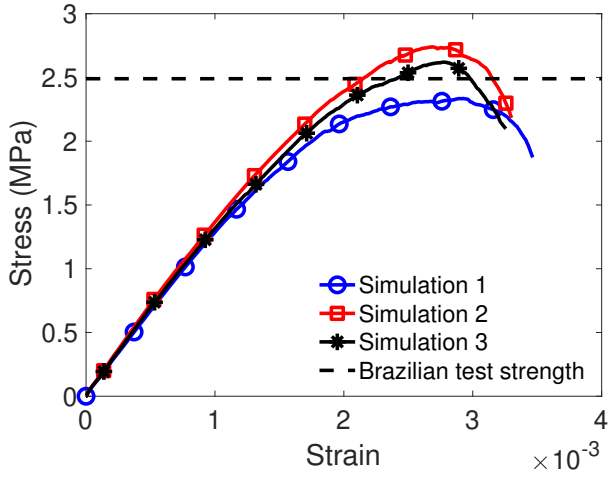

Figure 6.15: Stress-strain curves of concrete in the Brazilian tests simulated with the DEM

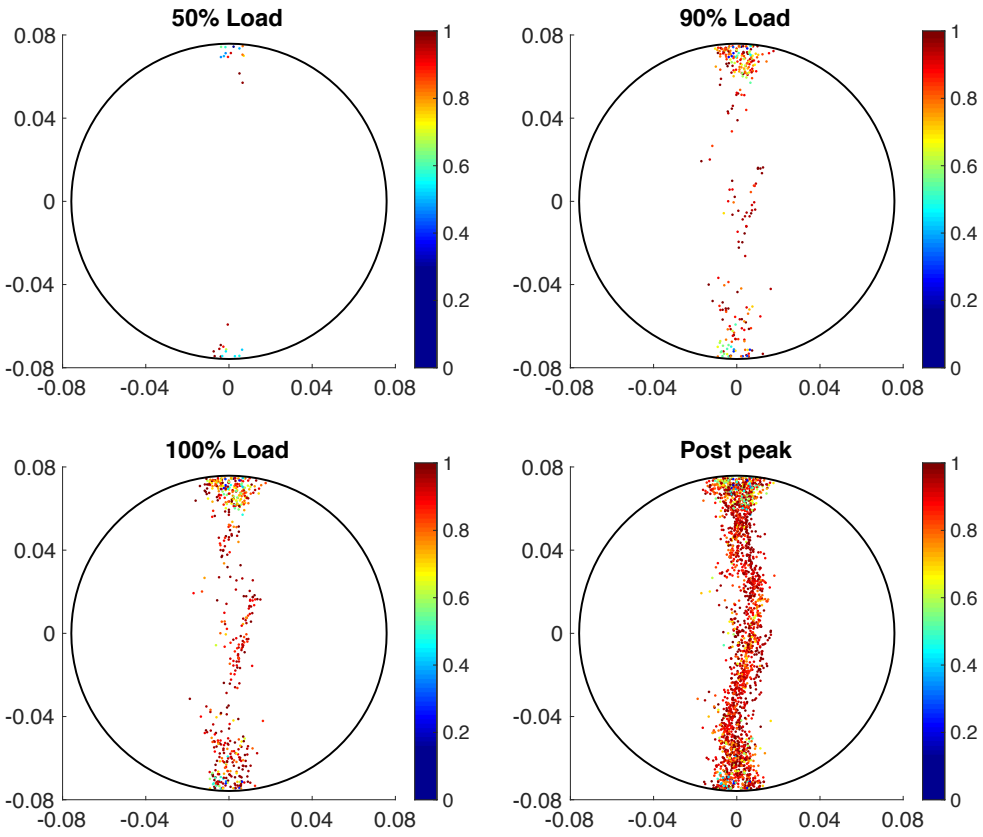

Figure 6.16: Micro-cracks in concrete at different stages of the Brazilian tests

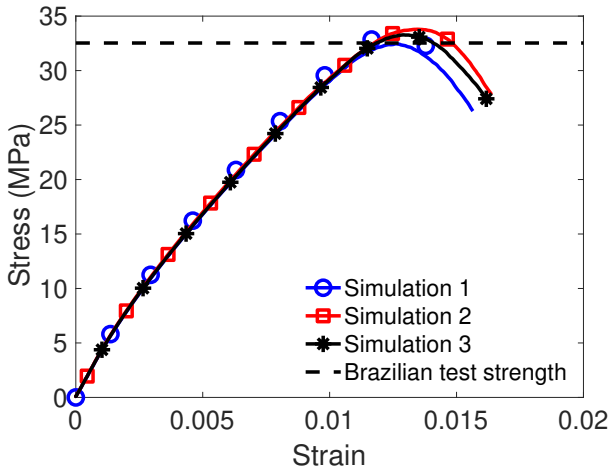

Figure 6.17: Stress-strain curves of concrete in the uniaxial compression tests simulated with the DEM

6.5 Sensitivity analysis

In Section 6.4, we calibrated our DEM model to reproduce the behavior of concrete, which exhibited lower strenght than mortar. Some authors hypothesized that the ITZ is a weak surface that lowers concrete strength compare to a mortar of same water/cement ratio and fine aggregates volume fraction [143, 25]. The ITZ is a layer of around 30 μm that can only be observed through scanning electron microscopy (SEM); it is hence challenging to monitor the ITZ during concrete loading. In addition, it was noted taht concrete strength decreases with the strength of coarse aggregates [165, 166], but most studies focused on strong aggregates materials. Despite qualitative observations, quantitaitive analyses of the effect of the ITZ and aggregate strength on concrete strength are lacking. Therefore, in this section we will study the sensitivity of concrete strength to the ITZ and to aggregate strength by simulating the BT and the UCT wit hour DEM model. We generate the DEM specimens following the method explained in Section 6.3.3 and we use the calibrated parameters listed in Table 6.2.

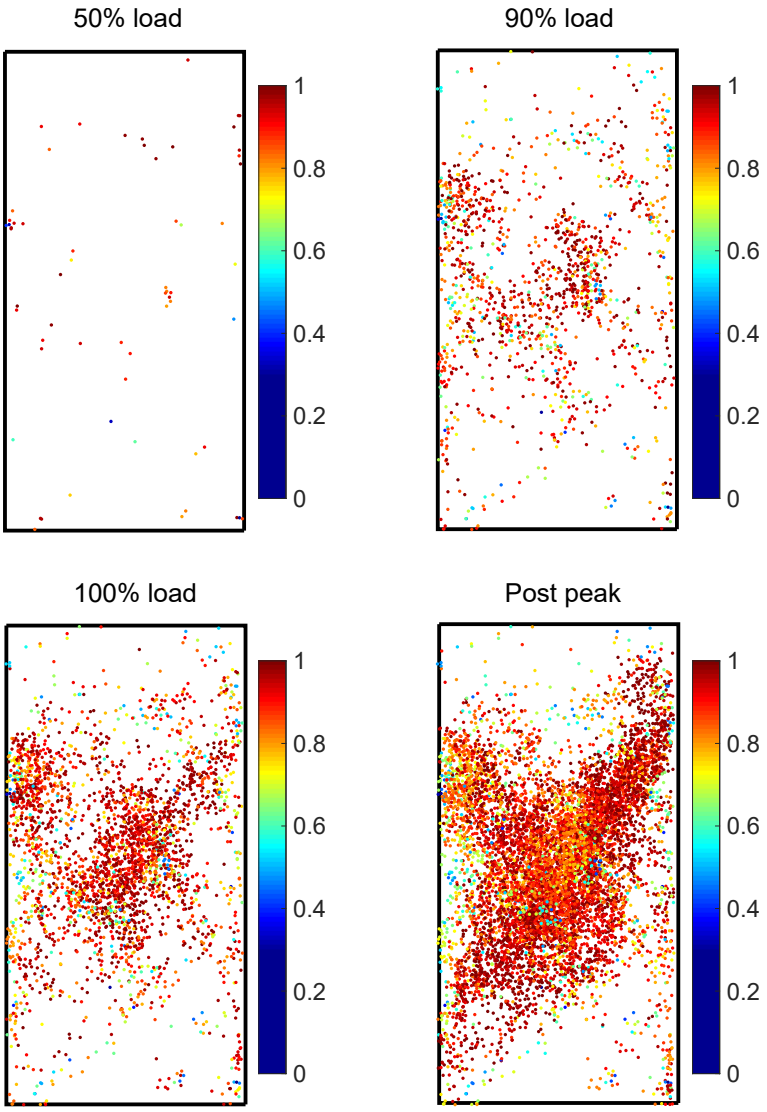

Figure 6.18: Micro-cracks in concrete at different stages of the uniaxial compression tests

6.5.1 Effect of the Interfacial Transition Zone (ITZ) on concrete strength

In our model, the weakening effect of the ITZ is accounted for by deleting a fraction of the aggregate/mortar bonds. We define the contact ratio, α, as the number of displacement softening contact bonds used at aggregate/mortar interfaces over the total number of interfacial contacts.The model was calibrated for $\alpha = 80\%$. We now vary α between 50% and 100% to understand the influence of mortar/aggregate adhesive surface on concrete BTS and UCS. Results are presented in Figures 6.19 and 6.20, respectively. Note that for each contact ratio α we conducted the BT and UCT simulatiosn at least three times. Only the average results are shown here. The ITZ greatly affects concrete strength: the BTS and the UCS respectively increase by 227.5% and 222.0% when α is varied from 50% to 100%. The stress/strain curves are similar in all simulations: At first, stress increases with strain but the stiffness gradually decreases due bond softening and breakage; Then stress reaches a peak value and the specimen starts to fail; As the specimen is further compressed, stress decreases rapidly and a large number of bonds break. Figure 6.21 and 6.22 show that the strength-contact ratio relationship is linear for both the BT and the UCT. The higher α, the higher the strength. Contacts without displacement softening contact bonds can be viewed as internal micro-cracks or micro-flaws, similar to the ITZ in actual concrete. Micro-crack interaction and coalescence occurs in specimens with low contact ratio, which drastically lowers concrete strength.

6.5.2 Effect of aggregate tensile strength on concrete strength

In the concrete tested in this study, the volume fraction of coarse aggregates amounts to nearly 45%. Aggregates are thus expected to play an important role in concrete mechanical behavior. The calibrated tensile strength of the coarse aggregates is 3.5 MPa, which is lower than the mortar BTS. During the BTs and UCTs, we note indeed that concrete strength is lower than that of mortar, and we observe a large number of crushed aggregates. Materials commonly used for coarse aggregates include quartzite, limestone, marble, low strength

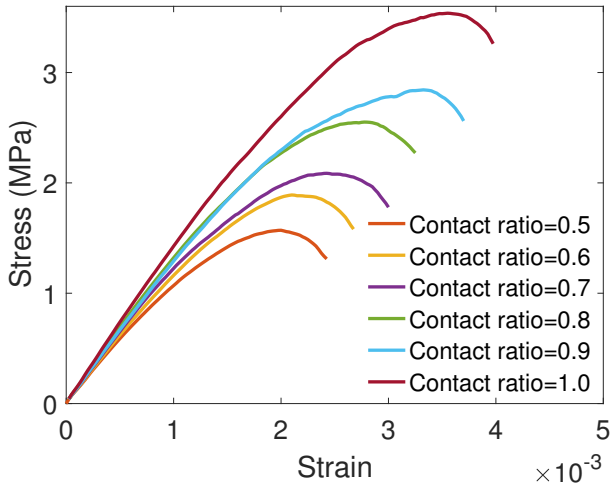

Figure 6.19: Stress-strain curves of concrete with different interface contact ratios in the Brazilian tests

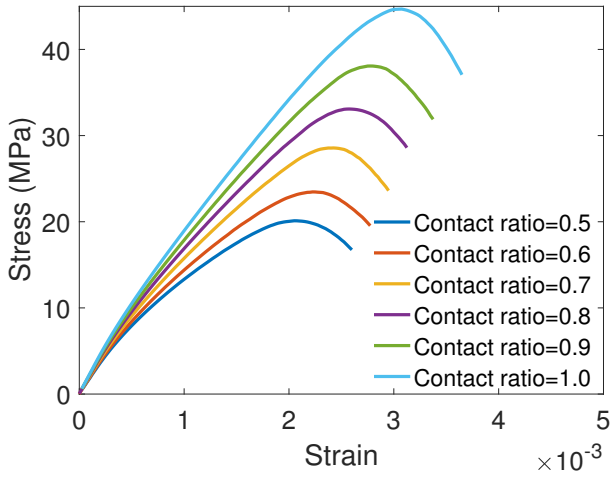

Figure 6.20: Stress-strain curves of concrete with different interface contact ratios in the uniaxial compression tests

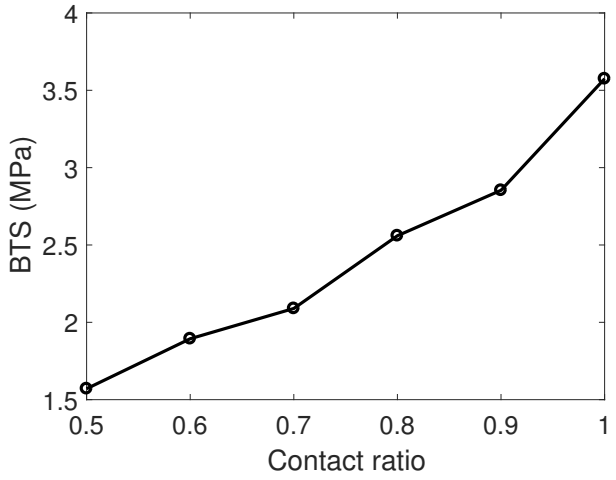

Figure 6.21: Effect of the interface contact ratio α on concrete BTS

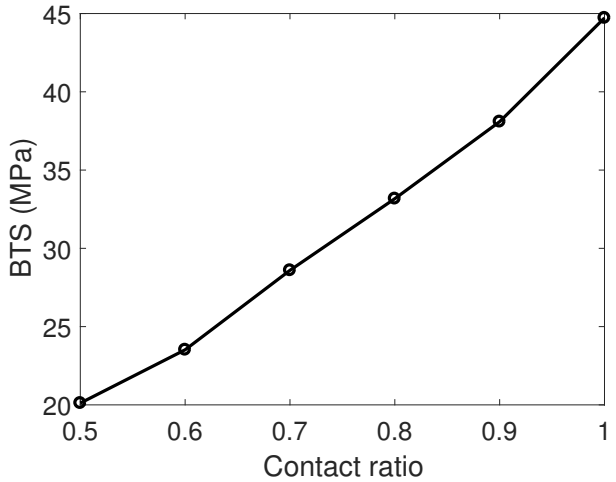

Figure 6.22: Effect of interface contact ratio α on concrete UCS

granite and high strength granite. Corresponding aggregate tensile strengths span from 3.0 MPa up to 15.0 MPa [167, 24]. In order to understand the effect of aggregate tensile strength on concrete BTS and UCS, concrete specimens with different aggregate strengths are generated and subjected to BTs and UCTs. As mentioned in Section 6.4.2, we assume that the ultimate bond displacement at failure is the same for all aggregates, so that the change of aggregate strength dictates the change of fracture energy, G_f. BT and UCT simulation results are shown in Figure 6.23 and 6.24, respectively. In general, concrete strength increases with aggregate strength, except in the simulation of the UCT with coarse aggregates with a tensile strength of 3.5 MPa. The exact reason for this unknown; this discrepancy may stem from the variability of concrete specimens generated with the DEM. Figures 6.25 and 6.26 show that the relationship between aggregate tensile strength and concrete strength is quasi-linear both on the BT and in the UCT. It it also noticeable that when the aggregate strength increased by more than 300%, concrete BTS and UCS increase by less 68%. In other words, both the ITZ and aggregate tensile strength influence concrete strength, but concrete strength is most sensitive to the contact ratio α in the ITZ.

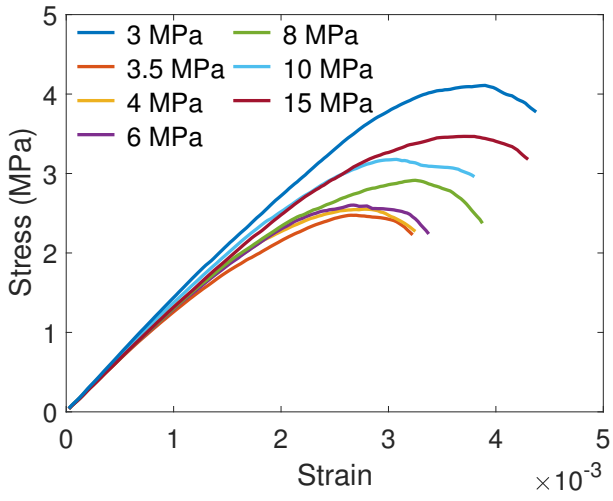

Figure 6.23: Stress-strain curves of concrete with different aggregate tensile strengths in the Brazilian tests

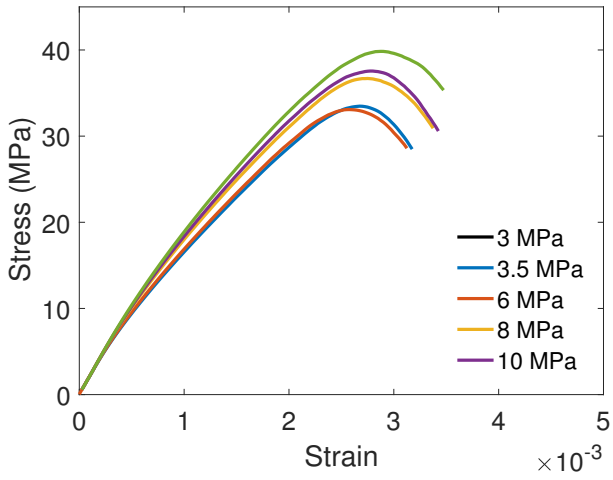

Figure 6.24: Stress-strain curves of concrete with different aggregate tensile strengths during the uniaxial compression tests

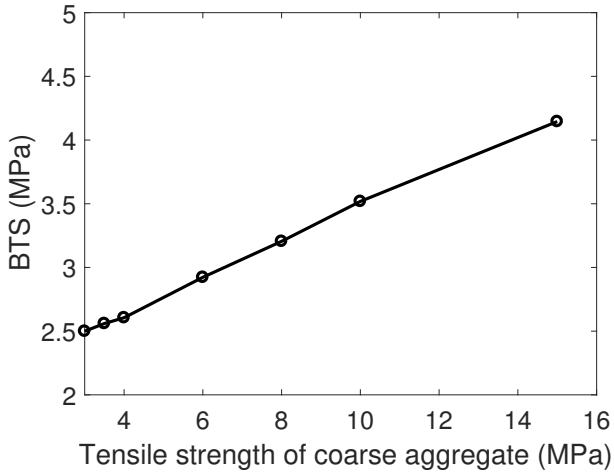

Figure 6.25: Effect of coarse aggregate tensile strength on concrete BTS

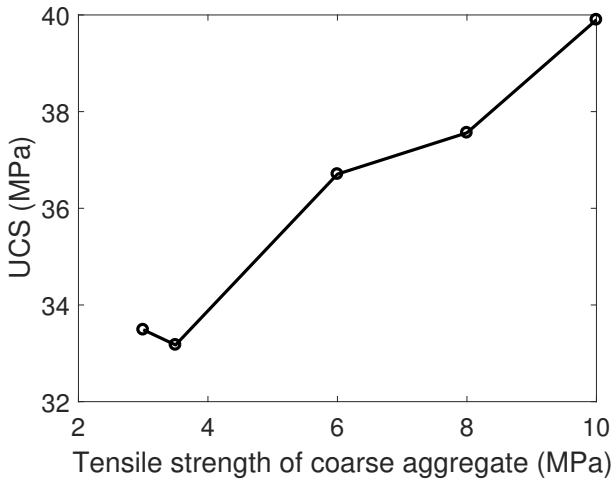

Figure 6.26: Effect of coarse aggregate tensile strength on concrete UCS

6.6 Conclusions

We proposed a displacement softening contact bond model and we calibrated a bonded particle DEM model of mortar against results of BT and UCT conduceted on mortar specimens. Coarse aggregates were then generated from point clouds obtained by scanning actual aggegates used in concrete. The aggregate bond parameterswere calibrated against concrete BTs and UCTs, with the calibrated mortar parameters. The proposed DEM model captures the mortar and concrete mechanical behavior with a realistic ratio of UCS/BTS. We then studied the influence of coarse aggregate tensile strength and of the adhesive area of the ITZ on concrete strength. The main conclusions are the following:

1. Concrete BTS and UCS increse with aggregate tensile strength and with teh ITZ contact ratio α.

   In our tests, mortar BTS and UCS are about twice as much as concrete BTS and UCS, respectively. Other authors had also noticed that concrete could have lower strength than mortar, and attributed this phenomenon to the weak surfaces in the ITZ. Our study confirms that the ITZ is the primary cause of low concrete strength. Aggregate volume fraction is usually around 30% or more. We found that multiplying the ag-

gregate tensile strength by four could increase concrete strength by 2/3. The effect of aggregate tensile strength on concrete strength had never been quantified before.

2. The proposed displacement softening contact bond model can capture mortar and concrete failure mechanisms in both the BT and the UCT. In the BT, micro-cracks first appear at the vicinity of the loading platens. But failure is induced by fractures tha initiate at the center of the specimen and that coalesce with the cracks loacted close to the platens. Specimens subjected to UCTs exhibits multiple shear failure planes – usually, two symmetric shear bands. A realistic ratio of UCT/BT is obtained. Micro-parameters used in the proposed bond model are closely related to the macro-scale material properties, which facilitates calibration.

3. The ITZ is accounted for by deleting bonds at the mortar/aggregate interface.The ITZ can be seen as a distribution of interfacial micro-cracks, like in actual concrete. Both in the BT and the UCT, a linear relationship exisits between the contact ratio α in the ITZ and concrete strength, for $0.5 \leq \alpha \geq 1.0$.

4. Concrete strength is linearly related to aggregate tensile strength. Weak aggregates decrease concrete strength. However, the influence of aggregate tensile strength on conrte strength is much lower than that of the ITZ.

The proposed softening displacement contact bond model is suitable to predict the behavior of concrete with the DEM. Results of the sensitivity analysis presented here suggest that increasing the adhesive area of the mortar/aggregate interface should improve the mechanical performance of concrete. Future studies will aim to understand the topological and physical factors that control the rheology of the aggregate/mortar interface.

CHAPTER 7
CONCLUSION

7.1 Summary

In this thesis, we propose a micro-mechanical analysis of quasi-static particulate fragmentation by means of the Discrete Element Method (DEM).

In Chapter 2, we provided an overview of the state-of-the-art techniques available to characterize and model fragmentation in granular media. Photo-elasticity and X-ray Computed Tomography [49] are the most commonly used techniques to visualize stress distributions and contact evolutions during breakage, respectively. Single particles subject to uniaxial compression fail due to the development of tensile stress at the center [11]. Particle strength is size dependent [86]. At the scale of the granular assembly, it was proposed that the ultimate PSD of granular material can be characterized by a Weibull distribution [39, 36]. A relative breakage index can be defined based on the difference between the current PSD and the initial PSD, normalized by the difference between the ultimate PSD and the initial PSD. In contiuum mechanics, particle breakage is usually modeled by relating energy dissipation to the increase of particles' surface and/or to the frictional displacement field [30, 55]. The evolution of energy distribution reveals the evolution of breakage and the resulting plastic deformation. The DEM allows simulating particle fragmentation either through the breakage of bonds within clusters of spherical elements (cluster method), or through the replacement of large particles by smaller ones, which represent fragments (replacement method).

In Chapter 3, we studied size and shielding effects during single particle crushing. Previous studies show that particle tensile strength decreases with particle size. At the same time, particle strength increases with the coordination number, which statistically increases

with particle size. To date, there is no clear understnading of what originates size effects and how size effects counter-act shielding effects in a granular assembly. To elucidate these two phenomena, we modeled a crushable sand particle as a quasi-spherical cluster of bonded non-breakable spherical elements. A series of single-particle uniaxial compression tests were simulated with the DEM. Rigid walls were placed around the particles to represent the confinement effect of neighboring particles. We varied the particle diameter and the number of walls, to study the effects of particle size and coordination number, respectively. We found that the cluster tensile strength did not depend on the cluster size as long as the ratio spherical element size / cluster size was smaller than 0.014. In addition, results show that particle strength depends: (1) linearly on particle coordination number; (2) quadratically on particle porosity.

We study particle breakage within a granular assembly in Chapter 4. We proposed a new DEM breakage model that combines the cluster method and the replacement method. The orientation of the breakage plane, the size of the fragments and the relative position of the particles after breakage are determined from X-ray Computer Tomography observations. An important improvement upon previously published models is that during the tensile splitting, the breakage plane is defined by the contact carrying the maximum normal force and direction of minimum principal stress, instead of assuming that the breakage plane contains the two maximum contact force vectors. The model allows simulating several cycles of splitting breakage and cluster fragment breakage. Because of the clusters introduced in the model, angular fragments can be produced during the simulation, depicting a realistic evolution of particle shape during crushing. By calibrating parameters in this model, we could accurately quantify the evolution of the PSD. Using the new breakage model also results in good agreement with the experimental stress – strain relationship.

In chapter 5, we analyzed the evolution of energy distribution in granular assemblies subject to breakage. We first proposed to redefine the so-called “coupling angle” used in breakage mechanics to couple the breakage and plasticity yield surfaces as a function of

the breakage parameters. This new relationship allowed capturing the transition between brittle and ductile behavior. Then, we proposed a method to calculate the distribution of energy in particulate assemblies subjected to confined comminution, under a wide range of compressive stresses. The work input, calculated by integrating the load-displacement curve, is written as the sum of the elastic deformation energy, the breakage energy and the redistribution energy. The latter can be viewed as the sum of the energy dissipated by friction at grain contacts and the kineric energy of the grains being rearranged during the comminution process. Results show that: (1) At least 60% of the work input is dissipated by particle redistribution; (2) The fraction of elastic deformation energy increases and the fraction of redistribution energy decreases as the compression stress increases; (3) The breakage energy accounts for less than 5% of the total input energy, and this value is independent of the compressive stress; (4) The energy dissipated by redistribution is between 14 to 30 times larger than the breakage energy. The evolution of the relative energy fractions confirms that the coupling angle is not a constant material parameter, but rather, a function of the breakage index.

In chapter 6 we focus the fragmentation of coarse aggregates in concrete. Published studies indicate that coarse aggregates have a strong influence on the mechanical behavior of concrete [24]. The interfacial transition zone (ITZ) between coarse aggregates and mortar also affects concrete strength. Despite these qualitative observations, no quantitative analysis was conducted so far to understand the effects of coarse aggregate strength and of the ITZ on concrete strength. To bridge this gap, we proposed a displacement softening contact bond model and we calibrated a bonded particle DEM model of mortar against results of Brazilan tests (BTs) and uniaxial compression tests (UCTs) conducted on mortar specimens. Coarse aggregates were then generated from point clouds obtained by scanning actual aggegates used in concrete. The aggregate bond parameters were calibrated against concrete BTs and UCTs, with the calibrated mortar parameters. The proposed DEM model captures the mortar and concrete mechanical behavior with a realistic ratio of uniaxial com-

pression strength (UCS) over Brazilan test strength (BTS). We then studied the influence of coarse aggregate tensile strength and of the adhesive area of the ITZ on concrete strength. We define the contact ratio, α, as the number of active bonds at the aggregate/mortar interface over the total number of interfacial contacts. Our conclusions are that: (1) concrete BTS and UCS increse with aggregate tensile strength and with the ITZ contact ratio α; (2) the proposed displacement softening contact bond model can capture mortar and concrete failure mechanisms in both the BT and the UCT; (3) Concrete strength is linearly related to aggregate tensile strength.

7.2 Future Work

Many challenges need to be overcome to relax some of the assumptions that we made in our DEM models. Below are some ideas to continue and improve the work.

1. We will consider multiple failure modes in the replacement method. Currently the replacement method proposed in Chapter 4 assumes that first generation of breakage is always caused by tensile failure. This assumption leads to under-estimating the volume of fines that are generated from surface chipping. Adding other failure modes will increase the accuracy of the simulation results.

2. Many factors such as size, coordination number, contact positions and force magnitude control breakage processes. We envision to use machien learning to train our DEM simulator to predict specific breakage events (e.g., tensile splitting, multi-fold fragmentation, chipping, abrasion) from XCT images.

3. An appplication of the two improvements proposed above is to validate the proposed displacement softening contact bond model against triaxial tests. So far, the model was calibrated against Brazilian tests and uniaxial compression tests conducted on mortar and concrete. Additional tests used for validation will have to be performed on the same concrete as that used for model calibration. More complex stress paths

will be simulated to identify the loading conditions that lead to specific breakage events.

4. Epoxy resins have been widely used as coating materials, structural adhesives, and electrical insulators. In civil engineering, epoxy injection is used to repair cracks in concrete [168, 169]. Both concrete and epoxy could be modeled with the DEM by using the displacement softening contact model, which would allow understanding the effects of aggregate/mortar topology on concrete strength, as well as optimizing the distribution of epoxy resin in concrete for reparation purposes.

5. Models proposed so far are restricted to quasi-static loading conditions. However, many granular media, such as railway ballast or pavement aggregates, are subjected to dynamic loads. It is therefore important to understand how the development of kinetic energy in a granular assembly affects the process of fragmentation. According to previous studies, it is anticipated that breakage is more prominent under quasi-static loading conditions than under dynamic loads [170].

6. In this thesis, we focused on purely mechanical processes. However, recent studies [171, 172] indicate that the presence of water plays a critical role on particle breakage and the subsequent collapse of granular assemblies. One hypothesis that was put forward is the the development of corrosion stress initiates cracks at grain contacts [173, 174].

REFERENCES

[1] B. P. Numbi, J. Zhang, and X. Xia, "Optimal energy management for a jaw crushing process in deep mines," *Energy*, vol. 68, pp. 337–348, 2014.

[2] S. Lobo-Guerrero and L. E. Vallejo, "Discrete element method analysis of railtrack ballast degradation during cyclic loading," *Granular Matter*, vol. 8, no. 3, pp. 195–204, 2006.

[3] A. W. Momber, "The fragmentation of standard concrete cylinders under compression: The role of secondary fracture debris," *Engineering Fracture Mechanics*, vol. 67, no. 5, pp. 445–459, 2000.

[4] K. T. Savjani, A. K. Gajjar, and J. K. Savjani, "Drug solubility: Importance and enhancement techniques," *ISRN pharmaceutics*, vol. 2012, 2012.

[5] P. Khadka, J. Ro, H. Kim, I. Kim, J. T. Kim, H. Kim, J. M. Cho, G. Yun, and J. Lee, "Pharmaceutical particle technologies: An approach to improve drug solubility, dissolution and bioavailability," *asian journal of pharmaceutical sciences*, vol. 9, no. 6, pp. 304–316, 2014.

[6] G. McDowell and M. Bolton, "On the micromechanics of crushable aggregates," *Geotechnique*, vol. 48, no. 5, pp. 667–679, 1998.

[7] G. McDowell, "On the yielding and plastic compression of sand," *Soils and foundations*, vol. 42, no. 1, pp. 139–145, 2002.

[8] A. Nakata, M Hyde, H Hyodo, and Murata, "A probabilistic approach to sand particle crushing in the triaxial test," *Geotechnique*, vol. 49, no. 5, pp. 567–583, 1999.

[9] M. N. Panda and L. W. Lake, "Estimation of single-phase permeability from parameters of particle-size distribution," *AAPG bulletin*, vol. 78, no. 7, pp. 1028–1039, 1994.

[10] G. D. Nguyen and I. Einav, "The energetics of cataclasis based on breakage mechanics," *Pure and applied geophysics*, vol. 166, no. 10-11, pp. 1693–1724, 2009.

[11] Y. Hiramatsu and Y. Oka, "Determination of the tensile strength of rock by a compression test of an irregular test piece," in *International Journal of Rock Mechanics and Mining Sciences & Geomechanics Abstracts*, Elsevier, vol. 3, 1966, pp. 89–90.

[12] D Robertson, "Numerical simulations of crushable aggregates," PhD thesis, Ph. D. dissertation, University of Cambridge, 2000.

[13] Y. Salami, C. Dano, and P.-Y. Hicher, "An experimental study on the influence of the coordination number on grain crushing," *European Journal of Environmental and Civil Engineering*, pp. 1–17, 2017.

[14] Y. Cheng, Y Nakata, and M. Bolton, "Discrete element simulation of crushable soil," *Geotechnique*, vol. 53, no. 7, pp. 633–641, 2003.

[15] C. Tang, X. Xu, S. Kou, P.-A. Lindqvist, and H. Liu, "Numerical investigation of particle breakage as applied to mechanical crushing—part i: Single-particle breakage," *International journal of rock mechanics and mining sciences*, vol. 38, no. 8, pp. 1147–1162, 2001.

[16] G. McDowell and O Harireche, "Discrete element modelling of soil particle fracture," *Géotechnique*, vol. 52, no. 2, pp. 131–135, 2002.

[17] G. R. McDowell and J. P. de Bono, "On the micro mechanics of one-dimensional normal compression," *Géotechnique*, vol. 63, no. 11, p. 895, 2013.

[18] S. Lobo-Guerrero, L. E. Vallejo, and L. F. Vesga, "Visualization of crushing evolution in granular materials under compression using DEM," *International Journal of Geomechanics*, vol. 6, no. 3, pp. 195–200, 2006.

[19] M. O. Ciantia, M. Arroyo, J. Butlanska, and A. Gens, "DEM modelling of cone penetration tests in a double-porosity crushable granular material," *Computers and Geotechnics*, vol. 73, pp. 109–127, 2016.

[20] A. R. Russell and I. Einav, "Energy dissipation from particulate systems undergoing a single particle crushing event," *Granular Matter*, vol. 15, no. 3, pp. 299–314, 2013.

[21] M. Bolton, Y Nakata, and Y. Cheng, "Micro-and macro-mechanical behaviour of DEM crushable materials," *Geotechnique*, vol. 58, no. 6, pp. 471–480, 2008.

[22] T. Afshar, M. M. Disfani, A. Arulrajah, G. A. Narsilio, and S. Emam, "Impact of particle shape on breakage of recycled construction and demolition aggregates," *Powder Technology*, vol. 308, pp. 1–12, 2017.

[23] C. Ovalle, C. Dano, and P.-Y. Hicher, "Experimental data highlighting the role of surface fracture energy in quasi-static confined comminution," *International Journal of Fracture*, vol. 182, no. 1, pp. 123–130, 2013.

[24] K.-R. Wu, B. Chen, W. Yao, and D. Zhang, "Effect of coarse aggregate type on mechanical properties of high-performance concrete," *Cement and Concrete Research*, vol. 31, no. 10, pp. 1421–1425, 2001.

[25] K. L. Scrivener, A. K. Crumbie, and P. Laugesen, "The interfacial transition zone (itz) between cement paste and aggregate in concrete," *Interface science*, vol. 12, no. 4, pp. 411–421, 2004.

[26] J Billam, "Some aspects of the behaviour of granular materials at high pressures," in *Proc. of the Roscoe Memorial Symp., Cambridge*, 1972, pp. 69–80.

[27] J. Jaeger, "Failure of rocks under tensile conditions," in *International Journal of Rock Mechanics and Mining Sciences & Geomechanics Abstracts*, Elsevier, vol. 4, 1967, pp. 219–227.

[28] M Lu and G. McDowell, "The importance of modelling ballast particle shape in the discrete element method," *Granular matter*, vol. 9, no. 1-2, pp. 69–80, 2007.

[29] Z. Karatza, E. Andò, S.-A. Papanicolopulos, J. Y. Ooi, and G. Viggiani, "Evolution of deformation and breakage in sand studied using X-ray tomography," *Géotechnique*, vol. 68, no. 2, pp. 107 –117, 2018.

[30] A. Daouadji, P.-Y. Hicher, and A. Rahma, "An elastoplastic model for granular materials taking into account grain breakage," *European Journal of Mechanics-A/Solids*, vol. 20, no. 1, pp. 113–137, 2001.

[31] P. V. Lade, J. A. Yamamuro, and P. A. Bopp, "Significance of particle crushing in granular materials," *Journal of Geotechnical Engineering*, vol. 122, no. 4, pp. 309–316, 1996.

[32] R. J. Marsal, "Large-scale testing of rockfill materials," *Journal of the Soil Mechanics and Foundations Division*, vol. 93, no. 2, pp. 27–43, 1967.

[33] K. L. Lee and I. Farhoomand, "Compressibility and crushing of granular soil in anisotropic triaxial compression," *Canadian geotechnical journal*, vol. 4, no. 1, pp. 68–86, 1967.

[34] B. O. Hardin, "Crushing of soil particles," *Journal of Geotechnical Engineering*, vol. 111, no. 10, pp. 1177–1192, 1985.

[35] P. Wang and C. Arson, "Energy distribution during the quasi-static confined comminution of granular materials," *Acta Geotechnica*, vol. 13, no. 5, pp. 1075–1083, 2018.

[36] I. Einav, "Breakage mechanics-part i: Theory," *Journal of the Mechanics and Physics of Solids*, vol. 55, no. 6, pp. 1274 –1297, 2007.

[37] C. Sammis, G. King, and R. Biegel, "The kinematics of gouge deformation," *Pure and Applied Geophysics*, vol. 125, no. 5, pp. 777–812, 1987.

[38] D. Turcotte, "Fractals and fragmentation," *Journal of Geophysical Research: Solid Earth*, vol. 91, no. B2, pp. 1921–1926, 1986.

[39] G. McDowell, M. Bolton, and D Robertson, "The fractal crushing of granular materials," *Journal of the Mechanics and Physics of Solids*, vol. 44, no. 12, pp. 2079–2101, 1996.

[40] A. Procopio, A Zavaliangos, and J. Cunningham, "Analysis of the diametrical compression test and the applicability to plastically deforming materials," *Journal of Materials Science*, vol. 38, no. 17, pp. 3629–3639, 2003.

[41] P. Wang and C. Arson, "Discrete element modeling of shielding and size effects during single particle crushing," *Computers and Geotechnics*, vol. 78, pp. 227–236, 2016.

[42] B. H.B.D.D.C.C. L. Sollenberger, "Feed size effects in single particle crushing," *Transactions of the Society of Petroleum Engineers of the American Institute of Mining, Metallurgical, and Petroleum Engineers*, vol. 226, pp. 433–441, 1963.

[43] Z. P. Bažant, "Size effect in blunt fracture: Concrete, rock, metal," *Journal of Engineering Mechanics*, 1984.

[44] Z. P. Bazant, M. T. Kazemi, T. Hasegawa, and J. Mazars, "Size effect in brazilian split-cylinder tests: Measurements and fracture analysis," *ACI Materials Journal*, vol. 88, no. 3, pp. 325–332, 1991.

[45] C. Ovalle, E. Frossard, C. Dano, W. Hu, S. Maiolino, and P.-Y. Hicher, "The effect of size on the strength of coarse rock aggregates and large rockfill samples through experimental data," *Acta Mechanica*, vol. 225, no. 8, pp. 2199–2216, 2014.

[46] Y. Ma and H. Huang, "A displacement-softening contact model for discrete element modeling of quasi-brittle materials," *International Journal of Rock Mechanics and Mining Sciences*, vol. 104, pp. 9–19, 2018.

[47] Y. Ma, "Discrete element modeling of the brittle-ductile transition in strength tests for quasi-brittle materials," PhD thesis, Georgia Institute of Technology, 2017.

[48] R. Brzesowsky, C. Spiers, C. Peach, and S. Hangx, "Failure behavior of single sand grains: Theory versus experiment," *Journal of Geophysical Research: Solid Earth*, vol. 116, no. B6, 2011.

[49] Z Karatza, E Andò, S. Papanicolopulos, J. Ooi, and G Viggiani, "Evolution of deformation and breakage in sand studied using x-ray tomography," *Géotechnique*, vol. 1, pp. 1–11, 2017.

[50] L Rothenburg and N. P. Kruyt, "Critical state and evolution of coordination number in simulated granular materials," *International Journal of Solids and Structures*, vol. 41, no. 21, pp. 5763–5774, 2004.

[51] M. C. Todisco, M. R. Coop, Q Guo, and K Senetakis, "The effect of the coordination number on particle crushing," in *Geomechanics from Micro to Macro, Vols I and II*, CRC PRESS-TAYLOR & FRANCIS GROUP, 2015, pp. 1063–1068.

[52] W. Lim and G. McDowell, "The importance of coordination number in using agglomerates to simulate crushable particles in the discrete element method," *Géotechnique*, vol. 57, no. 8, pp. 701–705, 2007.

[53] J. Desrues and G. Viggiani, "Strain localization in sand: An overview of the experimental results obtained in grenoble using stereophotogrammetry," *International Journal for Numerical and Analytical Methods in Geomechanics*, vol. 28, no. 4, pp. 279–321, 2004.

[54] W. Salim and B. Indraratna, "A new elastoplastic constitutive model for coarse granular aggregates incorporating particle breakage," *Canadian Geotechnical Journal*, vol. 41, no. 4, pp. 657–671, 2004.

[55] M. Cecconi, A. DeSimone, C. Tamagnini, and G. MB Viggiani, "A constitutive model for granular materials with grain crushing and its application to a pyroclastic soil," *International Journal for Numerical and Analytical Methods in Geomechanics*, vol. 26, no. 15, pp. 1531–1560, 2002.

[56] N. Miura and S. O-HARA, "Particle-crushing of a decomposed granite soil under shear stresses," *Soils and Foundations*, vol. 19, no. 3, pp. 1–14, 1979.

[57] I. Einav, "Breakage mechanics—part ii: Modelling granular materials," *Journal of the Mechanics and Physics of Solids*, vol. 55, no. 6, pp. 1298–1320, 2007.

[58] Y. Zhang and G Buscarnera, "A rate-dependent breakage model based on the kinetics of crack growth at the grain scale," *Géotechnique*, pp. 1–15, 2017.

[59] A. Das, A. Tengattini, G. Nguyen, and I. Einav, "A micromechanics based model for cemented granular materials," *Constitutive Modeling of Geomaterials*, pp. 527–534, 2013.

[60] P Wang, C Arson, *et al.*, "Breakage mechanics modeling of the brittle-ductile transition in granular materials," in *50th US Rock Mechanics/Geomechanics Symposium*, American Rock Mechanics Association, 2016.

[61] Y. Zhang and G Buscarnera, "Prediction of breakage-induced couplings in unsaturated granular soils," *Géotechnique*, vol. 65, no. 2, pp. 135–140, 2015.

[62] S Mercier and A Molinari, "Homogenization of elastic–viscoplastic heterogeneous materials: Self-consistent and mori-tanaka schemes," *International Journal of Plasticity*, vol. 25, no. 6, pp. 1024–1048, 2009.

[63] Q.-S. Zheng and D.-X. Du, "An explicit and universally applicable estimate for the effective properties of multiphase composites which accounts for inclusion distribution," *Journal of the Mechanics and Physics of Solids*, vol. 49, no. 11, pp. 2765–2788, 2001.

[64] R. Hill, "Continuum micro-mechanics of elastoplastic polycrystals," *Journal of the Mechanics and Physics of Solids*, vol. 13, no. 2, pp. 89–101, 1965.

[65] A. Pouya, C. Zhu, and C. Arson, "Micro–macro approach of salt viscous fatigue under cyclic loading," *Mechanics of Materials*, vol. 93, pp. 13–31, 2016.

[66] Y. Cheng, M. Bolton, and Y Nakata, "Crushing and plastic deformation of soils simulated using DEM," *Geotechnique*, vol. 54, no. 2, pp. 131–141, 2004.

[67] C. Kwok and M. Bolton, "DEM simulations of soil creep due to particle crushing," *Géotechnique*, vol. 63, no. 16, p. 1365, 2013.

[68] J. Wang and H. Yan, "DEM analysis of energy dissipation in crushable soils," *Soils and Foundations*, vol. 52, no. 4, pp. 644–657, 2012.

[69] S. Abe and K. Mair, "Grain fracture in 3d numerical simulations of granular shear," *Geophysical Research Letters*, vol. 32, no. 5, 2005.

[70] C Couroyer, Z Ning, and M Ghadiri, "Distinct element analysis of bulk crushing: Effect of particle properties and loading rate," *Powder Technology*, vol. 109, no. 1-3, pp. 241–254, 2000.

[71] M. Ciantia, M. Arroyo Alvarez de Toledo, F. Calvetti, and A. Gens, "An approach to enhance efficiency of DEM modelling of soils with crushable grains," *Géotechnique*, vol. 65, no. 2, pp. 91–110, 2015.

[72] J de Bono and G McDowell, "Particle breakage criteria in discrete-element modelling," *Géotechnique*, vol. 66, no. 12, pp. 1014–1027, 2016.

[73] J. Åström and H. Herrmann, "Fragmentation of grains in a two-dimensional packing," *The European Physical Journal B-Condensed Matter and Complex Systems*, vol. 5, no. 3, pp. 551–554, 1998.

[74] O. Ben-Nun and I. Einav, "The role of self-organization during confined comminution of granular materials," *Philosophical Transactions of the Royal Society of London A: Mathematical, Physical and Engineering Sciences*, vol. 368, no. 1910, pp. 231–247, 2010.

[75] K. J. Hanley, C. O'Sullivan, and X. Huang, "Particle-scale mechanics of sand crushing in compression and shearing using DEM," *Soils and Foundations*, vol. 55, no. 5, pp. 1100–1112, 2015.

[76] O. Tsoungui, D. Vallet, and J.-C. Charmet, "Numerical model of crushing of grains inside two-dimensional granular materials," *Powder technology*, vol. 105, no. 1, pp. 190–198, 1999.

[77] G. R. McDowell, J. P. de Bono, P. Yue, and H.-S. Yu, "Micro mechanics of isotropic normal compression," *Géotechnique Letters*, vol. 3, no. 4, pp. 166–172, 2013.

[78] O Ben-Nun, I Einav, and A Tordesillas, "Force attractor in confined comminution of granular materials," *Physical review letters*, vol. 104, no. 10, p. 108 001, 2010.

[79] M. Todisco, W Wang, M. Coop, and K Senetakis, "Multiple contact compression tests on sand particles," *Soils and Foundations*, vol. 57, no. 1, pp. 126–140, 2017.

[80] Z. Karatza, "A study of temporal and spatial evolution of deformation and breakage of dry granular materials using x-ray computed tomography and the discrete element method," PhD thesis, Department of Civil and Environmental Engineering, The University of Edinburgh, 2017.

[81] L. Scholtès and F.-V. Donzé, "A DEM model for soft and hard rocks: Role of grain interlocking on strength," *Journal of the Mechanics and Physics of Solids*, vol. 61, no. 2, pp. 352–369, 2013.

[82] L. Scholtès, F.-V. Donzé, and M. Khanal, "Scale effects on strength of geomaterials, case study: Coal," *Journal of the Mechanics and Physics of Solids*, vol. 59, no. 5, pp. 1131–1146, 2011.

[83] W. L. Lim, "Mechanics of railway ballast behaviour," PhD thesis, University of Nottingham, 2004.

[84] A. A. Griffith, "The phenomena of rupture and flow in solids," *Philosophical transactions of the royal society of london. Series A, containing papers of a mathematical or physical character*, vol. 221, pp. 163–198, 1921.

[85] B. Darvell, "Uniaxial compression tests and the validity of indirect tensile strength," *Journal of Materials Science*, vol. 25, no. l990, pp. 757–780, 1990.

[86] D.-M. Lee, "The angles of friction of granular fills.," PhD thesis, University of Cambridge, 1992.

[87] W. Weibull, *A statistical theory of the strength of materials*, 151. Generalstabens litografiska anstalts förlag, 1939.

[88] P. A. Cundall and O. D. Strack, "A discrete numerical model for granular assemblies," *Geotechnique*, vol. 29, no. 1, pp. 47–65, 1979.

[89] Itasca, *Particle flow code in three dimensions, version 4.0*. Itasca Consulting Group, Inc., Minnesota., 2008.

[90] M. B. Cil and K. A. Alshibli, "3d modeling of sand particle fracture using discrete element method and synchrotron micro-tomography images," in *Geo-Congress 2014 Technical Papers@ sGeo-characterization and Modeling for Sustainability*, ASCE, 2014, pp. 2822–2829.

[91] I Cavarretta and C O'SULLIVAN, "The mechanics of rigid irregular particles subject to uniaxial compression," *Géotechnique*, vol. 62, no. 8, pp. 681–692, 2012.

[92] K. L. Johnson and K. L. Johnson, *Contact mechanics*. Cambridge university press, 1987.

[93] N. a. Cho, C. Martin, and D. Sego, "A clumped particle model for rock," *International Journal of Rock Mechanics and Mining Sciences*, vol. 44, no. 7, pp. 997–1010, 2007.

[94] J. F. Hazzard, R. P. Young, and S. Maxwell, "Micromechanical modeling of cracking and failure in brittle rocks," *Journal of Geophysical Research: Solid Earth (1978–2012)*, vol. 105, no. B7, pp. 16 683–16 697, 2000.

[95] E. Buckingham, "On physically similar systems; illustrations of the use of dimensional equations," *Physical Review*, vol. 4, no. 4, pp. 345–376, 1914.

[96] H Huang, *Discrete element modeling of tool-rock interaction, university of minnesota*, 1999.

[97] B. Yang, Y. Jiao, and S. Lei, "A study on the effects of microparameters on macroproperties for specimens created by bonded particles," *Engineering Computations*, vol. 23, no. 6, pp. 607–631, 2006.

[98] S Lei, P Kaitkay, and X Shen, "Simulation of rock cutting using distinct element method-pfc 2d," *Numerical modeling in micromechanics via particle methods*, vol. 1, no. 4, pp. 63–72, 2004.

[99] D. Potyondy and P. Cundall, "A bonded-particle model for rock," *International journal of rock mechanics and mining sciences*, vol. 41, no. 8, pp. 1329–1364, 2004.

[100] A. Standard, "D2487 (2011) standard practice for classification of soils for engineering purposes (unified soil classification system)," *ASTM International, West Conshohocken, PA www.ASTM.org*,

[101] G. Marsaglia *et al.*, "Choosing a point from the surface of a sphere," *The Annals of Mathematical Statistics*, vol. 43, no. 2, pp. 645–646, 1972.

[102] S. Antonyuk, J. Tomas, S. Heinrich, and L. Mörl, "Breakage behaviour of spherical granulates by compression," *Chemical engineering science*, vol. 60, no. 14, pp. 4031–4044, 2005.

[103] J Billam, "Some aspects of the behaviour of granular materials at high pressure," *stress-strain behaviour of soils*, 1972.

[104] M. P. Schöpfer, S. Abe, C. Childs, and J. J. Walsh, "The impact of porosity and crack density on the elasticity, strength and friction of cohesive granular materials: Insights from DEM modelling," *International Journal of Rock Mechanics and Mining Sciences*, vol. 46, no. 2, pp. 250–261, 2009.

[105] C. Chang, M. D. Zoback, and A. Khaksar, "Empirical relations between rock strength and physical properties in sedimentary rocks," *Journal of Petroleum Science and Engineering*, vol. 51, no. 3, pp. 223–237, 2006.

[106] B. Zhao, J. Wang, M. R. Coop, G. Viggiani, and M. Jiang, "An investigation of single sand particle fracture using x-ray micro-tomography.," *Géotechnique*, vol. 65, no. 8, pp. 625 –641, 2015.

[107] J. Fonseca, C. O'Sullivan, M. Coop, and P. Lee, "Non-invasive characterization of particle morphology of natural sands," *Soils and Foundations*, vol. 52(4): 712-722, 2012.

[108] E. Andò, S. A. Hall, G. Viggiani, J. Desrues, and P. Bésuelle, "Grain-scale experimental investigation of localised deformation in sand: A discrete particle tracking approach," *Acta Geotechnica*, vol. 7, no. 1, pp. 1 –13, 2012.

[109] G. Guida, F. Casini, G. M. B. Viggiani, E. Andò, and G. Viggiani, "Breakage mechanisms of highly porous particles in 1d compression revealed by X-ray tomography," *Géotechnique Letters*, vol. 8, no. 2, pp. 155 –160, 2018.

[110] A. M. Druckrey and K. A. Alshibli, "3D finite element modeling of sand particle fracture based on in situ X-ray synchrotron imaging," *International Journal for Numerical and Analytical Methods in Geomechanics*, vol. 40, no. 1, pp. 105 –116, 2016.

[111] M. B. Cil and K. A. Alshibli, "Modeling the influence of particle morphology on the fracture behavior of silica sand using a 3D discrete element method," *Comptes Rendus Mécanique*, vol. 343(2): 133-142, 2015.

[112] C. Sammis, G. King, and R. Biegel, "The kinematics of gouge deformation," *Pure and applied geophysics*, vol. 125, no. 5, pp. 777 –812, 1987.

[113] O. Tsoungui, D. Vallet, and J.-C. Charmet, "Numerical model of crushing of grains inside two-dimensional granular materials," *Powder Technology*, vol. 105, no. 1, pp. 190 –198, 1999.

[114] E. Andò, "Experimental investigation of micro-structural changes in deforming granular media using x-ray tomography," PhD thesis, Université de Grenoble, 2013.

[115] Z. Karatza, E. Andò, S.-A. Papanicolopulos, G. Viggiani, and J. Y. Ooi, "Evolution of particle breakage studied using x-ray tomography and the discrete element method," *EPJ Web Conf.*, vol. 140, p. 07 013, 2017.

[116] W.-H. Tsai, "Document image analysis," in, L. O'Gorman and R. Kasturi, Eds., Los Alamitos, CA, USA: IEEE Computer Society Press, 1995, ch. Moment-preserving Thresholding: A New Approach, pp. 44 –60, ISBN: 0-8186-6547-5.

[117] S. Beucher and F. Meyer, "The morphological approach to segmentation: The watershed transformation," *Mathematical morphology in image processing. Optical Engineering*, vol. 34, pp. 433 –481, 1993.

[118] J. B. Roerdink and A. Meijster, "The watershed transform: Definitions, algorithms and parallelization strategies," *Fundamenta informaticae*, vol. 41, no. 1, 2, pp. 187–228, 2000.

[119] C. Itasca, "Pfc 3d-user manual," *Itasca Consulting Group, Minneapolis*, 1999.

[120] M. O. Ciantia, M Arroyo, F. Calvetti, and A Gens, "A numerical investigation of the incremental behavior of crushable granular soils," *International Journal for Numerical and Analytical Methods in Geomechanics*, vol. 40, no. 13, pp. 1773–1798, 2016.

[121] Y. Ma and H. Huang, "Dem analysis of failure mechanisms in the intact brazilian test," *International Journal of Rock Mechanics and Mining Sciences*, vol. 102, pp. 109–119, 2018.

[122] S. Lobo-Guerrero and L. E. Vallejo, "Application of weibull statistics to the tensile strength of rock aggregates," *Journal of geotechnical and geoenvironmental engineering*, vol. 132, no. 6, pp. 786–790, 2006.

[123] Y. Xu, C. Xu, Z. Zhou, J. Du, and D. Hu, "2D DEM simulation of particle mixing in rotating drum: A parametric study," *Particuology*, vol. 8, no. 2, pp. 141–149, 2010.

[124] J. Raisianzadeh, A. A. Mirghasemi, and S. Mohammadi, "2D simulation of breakage of angular particles using combined DEM and XFEM," *Powder Technology*, vol. 336, pp. 282 –297, 2018.

[125] I. Collins and G. Houlsby, "Application of thermomechanical principles to the modelling of geotechnical materials," in *Proceedings of the royal society of London A: Mathematical, physical and engineering sciences*, The Royal Society, vol. 453, 1997, pp. 1975–2001.

[126] B Zhao, J Wang, M. Coop, G Viggiani, and M Jiang, "An investigation of single sand particle fracture using x-ray micro-tomography," *Géotechnique*, vol. 65, no. 8, pp. 625–641, 2015.

[127] Y. Nakata, M. Hyodo, A. F. Hyde, Y. Kato, and H. Murata, "Microscopic particle crushing of sand subjected to high pressure one-dimensional compression," *Soils and foundations*, vol. 41, no. 1, pp. 69–82, 2001.

[128] A. Das, G. D. Nguyen, and I. Einav, "Compaction bands due to grain crushing in porous rocks: A theoretical approach based on breakage mechanics," *Journal of Geophysical Research: Solid Earth*, vol. 116, no. B8, 2011.

[129] K. Roscoe, A. Schofield, and A Thurairajah, "Yielding of clays in states wetter than critical," *Geotechnique*, vol. 13, no. 3, pp. 211–240, 1963.

[130] N. Miura and T. Yamamoto, "Particle-crushing properties of sands under high stresses," *Technology reports of the Yamaguchi University*, vol. 1, no. 4, pp. 439–447, 1976.

[131] A. Russell, "A compression line for soils with evolving particle and pore size distributions due to particle crushing, geotechnique let., 1 (), 5-9," *Géotechnique Letters*, vol. 1, no. 1, pp. 5–9, 2011.

[132] M Friedman, J Handin, and G Alani, "Fracture-surface energy of rocks," in *International Journal of Rock Mechanics and Mining Sciences & Geomechanics Abstracts*, Elsevier, vol. 9, 1972, pp. 757–764.

[133] N. Arsalan, S. S. Palayangoda, D. J. Burnett, J. J. Buiting, and Q. P. Nguyen, "Surface energy characterization of sandstone rocks," *Journal of Physics and Chemistry of Solids*, vol. 74, no. 8, pp. 1069–1077, 2013.

[134] S. W. Tyler and S. W. Wheatcraft, "Fractal scaling of soil particle-size distributions: Analysis and limitations," *Soil Science Society of America Journal*, vol. 56, no. 2, pp. 362–369, 1992.

[135] M. Coop, K. Sorensen, T. B. Freitas, and G Georgoutsos, "Particle breakage during shearing of a carbonate sand," *Géotechnique*, vol. 54, no. 3, pp. 157–163, 2004.

[136] Y. Nakata, Y. Kato, M. Hyodo, A. F. HYDE, and H. Murata, "One-dimensional compression behaviour of uniformly graded sand related to single particle crushing strength," *Soils and Foundations*, vol. 41, no. 2, pp. 39–51, 2001.

[137] S Zhang, C. Tong, X Li, and D Sheng, "A new method for studying the evolution of particle breakage," *Géotechnique*, vol. 65, no. 11, pp. 911–922, 2015.

[138] I. Celik, "The effects of particle size distribution and surface area upon cement strength development," *Powder Technology*, vol. 188, no. 3, pp. 272–276, 2009.

[139] I. F. Collins, "The concept of stored plastic work or frozen elastic energy in soil mechanics," *Geotechnique*, vol. 55, no. 5, pp. 373–382, 2005.

[140] M Jefferies, "Plastic work and isotropic softening in unloading," *Géotechnique*, vol. 47, no. 5, 1997.

[141] F. Radjai, M. Jean, J.-J. Moreau, and S. Roux, "Force distributions in dense two-dimensional granular systems," *Physical review letters*, vol. 77, no. 2, p. 274, 1996.

[142] J. Peters, M Muthuswamy, J Wibowo, and A Tordesillas, "Characterization of force chains in granular material," *Physical review E*, vol. 72, no. 4, p. 041 307, 2005.

[143] P. Monteiro, *Concrete: microstructure, properties, and materials*. McGraw-Hill Publishing, 2006.

[144] C ASTM *et al.*, "Standard test method for splitting tensile strength of cylindrical concrete," 2011.

[145] R Berenbaum and I Brodie, "Measurement of the tensile strength of brittle materials," *British Journal of Applied Physics*, vol. 10, pp. 281–287, 1959.

[146] Z. P. Ba¡ zant and M. Kazemi, "Determination of fracture energy, process zone longth and brittleness number from size effect, with application to rock and conerete," *International Journal of fracture*, vol. 44, no. 2, pp. 111–131, 1990.

[147] Ł. Skarżyński and J Tejchman, "Experimental investigations of fracture process in concrete by means of x-ray micro-computed tomography," *Strain*, vol. 52, no. 1, pp. 26–45, 2016.

[148] Z. P. Bazant and P. A. Pfeiffer, "Determination of fracture energy from size effect and brittleness number," *ACI Materials Journal*, vol. 84, no. 6, pp. 463–480, 1987.

[149] H. Nakamura and T. Higai, "Compressive fracture energy and fracture zone length of concrete," *Modeling of inelastic behavior of RC structures under seismic loads*, pp. 471–487, 2001.

[150] P. Peterson, "Fracture energy of concrete: Method of determination," *Cement and Concrete research*, vol. 10, no. 1, pp. 79–89, 1980.

[151] A. Fakhimi and T. Villegas, "Application of dimensional analysis in calibration of a discrete element model for rock deformation and fracture," *Rock Mechanics and Rock Engineering*, vol. 40, no. 2, p. 193, 2007.

[152] E Gallucci, K Scrivener, A Groso, M Stampanoni, and G Margaritondo, "3d experimental investigation of the microstructure of cement pastes using synchrotron x-ray microtomography," *Cement and Concrete Research*, vol. 37, no. 3, pp. 360–368, 2007.

[153] C. Rocco, G. V. Guinea, J. Planas, and M. Elices, "Size effect and boundary conditions in the brazilian test: Experimental verification," *Materials and Structures*, vol. 32, no. 3, p. 210, 1999.

[154] G Giaccio, C Rocco, and R Zerbino, "The fracture energy (g f) of high-strength concretes," *Materials and structures*, vol. 26, no. 7, pp. 381–386, 1993.

[155] E. N. Landis and E. N. Nagy, "Three-dimensional work of fracture for mortar in compression," *Engineering Fracture Mechanics*, vol. 65, no. 2-3, pp. 223–234, 2000.

[156] C Rosselló, M Elices, and G. Guinea, "Fracture of model concrete: 2. fracture energy and characteristic length," *Cement and concrete research*, vol. 36, no. 7, pp. 1345–1353, 2006.

[157] F. Wittmann, "Crack formation and fracture energy of normal and high strength concrete," *Sadhana*, vol. 27, no. 4, pp. 413–423, 2002.

[158] X. Ding and L. Zhang, "A new contact model to improve the simulated ratio of unconfined compressive strength to tensile strength in bonded particle models," *International Journal of Rock Mechanics and Mining Sciences*, vol. 69, pp. 111–119, 2014.

[159] D. Li and L. N. Y. Wong, "The brazilian disc test for rock mechanics applications: Review and new insights," *Rock mechanics and rock engineering*, vol. 46, no. 2, pp. 269–287, 2013.

[160] R. Bisai, "A study on modes of rock failure under uniaxial compression," PhD thesis, 2014.

[161] A. ASTM, "C39/c39m-18 standard test method for compressive strength of cylindrical concrete specimens. 2018," *ASTM International: West Conshohocken, PA*,

[162] Z. P. Bazant and J. Planas, *Fracture and size effect in concrete and other quasi-brittle materials, 1998*.

[163] Y. D. Murray, A. Y. Abu-Odeh, and R. P. Bligh, "Evaluation of ls-dyna concrete material model 159," Tech. Rep., 2007.

[164] W. Ren, Z. Yang, R. Sharma, C. Zhang, and P. J. Withers, "Two-dimensional x-ray ct image based meso-scale fracture modelling of concrete," *Engineering Fracture Mechanics*, vol. 133, pp. 24–39, 2015.

[165] J. Chi, R Huang, C. Yang, and J. Chang, "Effect of aggregate properties on the strength and stiffness of lightweight concrete," *Cement and Concrete Composites*, vol. 25, no. 2, pp. 197–205, 2003.

[166] M. Kaplan, "Flexural and compressive strength of concrete as affected by the properties of coarse aggregates," in *Journal Proceedings*, vol. 55, 1959, pp. 1193–1208.

[167] A. Baykasoğlu, H. Güllü, H. Çanakçı, and L. Özbakır, "Prediction of compressive and tensile strength of limestone via genetic programming," *Expert Systems with Applications*, vol. 35, no. 1-2, pp. 111–123, 2008.

[168] P Duarte, J. Correia, J. Ferreira, F Nunes, and M. Arruda, "Experimental and numerical study on the effect of repairing reinforced concrete cracked beams strength-

ened with carbon fibre reinforced polymer laminates," *Canadian Journal of Civil Engineering*, vol. 41, no. 3, pp. 222–231, 2014.

[169] C. A. Issa and P. Debs, "Experimental study of epoxy repairing of cracks in concrete," *Construction and Building Materials*, vol. 21, no. 1, pp. 157–163, 2007.

[170] J. Huang, S. Xu, and S. Hu, "Influence of particle breakage on the dynamic compression responses of brittle granular materials," *Mechanics of materials*, vol. 68, pp. 15–28, 2014.

[171] C Chávez and E. Alonso, "A constitutive model for crushed granular aggregates which includes suction effects," *Soils and Foundations*, vol. 43, no. 4, pp. 215–227, 2003.

[172] L. A. Oldecop and E. Alonso Pérez de Agreda, "Theoretical investigation of the time-dependent behaviour of rockfill," 2007.

[173] N. Brantut, P. Baud, M. Heap, and P. Meredith, "Micromechanics of brittle creep in rocks," *Journal of Geophysical Research: Solid Earth*, vol. 117, no. B8, 2012.

[174] N. Brantut, M. Heap, P. Meredith, and P. Baud, "Time-dependent cracking and brittle creep in crustal rocks: A review," *Journal of Structural Geology*, vol. 52, pp. 17–43, 2013.